TIME-DISTANCE MEASUREMENTS OF LARGE-SCALE FLOWS IN THE SOLAR CONVECTION ZONE

A DISSERTATION
SUBMITTED TO THE DEPARTMENT OF APPLIED PHYSICS
AND THE COMMITTEE ON GRADUATE STUDIES
OF STANFORD UNIVERSITY
IN PARTIAL FULFILLMENT OF THE REQUIREMENTS
FOR THE DEGREE OF
DOCTOR OF PHILOSOPHY

By
Peter M. Giles
December 1999

I certify that I have read this dissertation and that in my opinion it is fully adequate, in scope and quality, as a dissertation for the degree of Doctor of Philosophy.

Phil Scherrer
(Principal Advisor)

I certify that I have read this dissertation and that in my opinion it is fully adequate, in scope and quality, as a dissertation for the degree of Doctor of Philosophy.

Peter Sturrock

I certify that I have read this dissertation and that in my opinion it is fully adequate, in scope and quality, as a dissertation for the degree of Doctor of Philosophy.

Arthur B. C. Walker

Approved for the University Committee on Graduate Studies:

Abstract

Helioseismology has been a powerful tool for measuring the structure and rotation of the solar interior. However, there are still many aspects of the Sun's dynamics which are not well understood. This thesis uses the recently developed method of time-distance helioseismology, closely analogous to seismic exploration in geophysics, to search for large-scale flows in the interior of the Sun. With this technique, data from the Michelson Doppler Imager (MDI) have been used to measure the meridional circulation deep in the solar convection zone for the first time. The results show that the measurements are consistent with a meridional circulation which is 20 m/s poleward at the solar surface, and roughly 3 m/s equatorward at the base of the convection zone. The turnover point is just below $r = 0.80\mathrm{R}_\odot$. The meridional circulation is also observed to be varying with time, with the possible appearance of an equatorward surface flow at high latitudes during the rising phase of the solar magnetic cycle. In addition to these important results, the measurements have yielded interesting results for the solar differential rotation, including the possible detection of a highly localized asymmetric feature with an amplitude of 200 m/s.

All of these measurements illustrate the unique capabilities of the time-distance technique for looking at the solar interior in a new way. Furthermore, these results will have a bearing on our understanding of solar dynamics, particularly the solar cycle and the maintenance of the rotation profile.

Acknowledgements

There are many people who need to be mentioned and acknowledged, either for the part they played in this work, or just for being good friends during the last six years.

First of all, I would be remiss if I did not mention that SOHO is a project of international cooperation between ESA and NASA, and that my research was supported by NASA contract NAG5-3077 at Stanford University.

Second, there is a long list of people at Stanford who have contributed to this work in one way or another. From a scientific standpoint, Tom Duvall, Jr., was the guidance and the inspiration for the work, the inventor of the tools, and the Master to the apprentice. I have Phil Scherrer to thank for many of the ideas contained in this thesis and for his ability to ask the big questions. Alexander Kosovichev has also been an inspiration, and a teacher. Jesper Schou and Rasmus Munk Larsen provided the measurements of the internal rotation rate which I have used as a reference, and have also been helpful when I was drowning in an ocean of linear algebra. Also, the new measurements of the Carrington elements in appendix A were inspired by comments and suggestions made by Jesper. Rick Bogart wrote and maintained the remapping software used in the analysis. John Beck, Laurent Gizon, and Aaron Birch have also made contributions which appear in these pages. Also, a special thanks to Margie Stehle for keeping all the details in order, and especially for all her help during the last few weeks.

There is an even longer list of people who have made the last six years not only intellectually challenging but just plain fun. Out of the many friends I have made during this six years, I would like to especially thank Russ, Duncan and Julie, Adrian, Chris, Andreas and Eileen, and Brian, for making this six years into much more than

just work. My life will be better for knowing them. Jesper Schou makes this list also, for the four peaks we have stood on together: Mount Whitney, Mount Williamson, Mount Tyndall, and Mount Fuji. I spent many more weekends reaching some smaller summits with Jesper and Brian Roberts as well. Thank you also to everybody who helped me take out my frustrations with a hockey stick. Finally, let me recall an afternoon spent at Candlestick Park in late summer of 1997, with Rick and Tom, a bases-loaded double play and an extra-inning home run to beat the Dodgers.

Thank you also to my family; Mom and Dad, Kristina, and Steve and Angela. It has been a long time and I have been far away, and I have missed you all.

And of course, I wouldn't have done any of this without Kate's love, understanding, and support. The four years that we spent apart have made these last two even more wondrous. Truly she deserves an epic poem or a great novel; for now she will have to settle for the rest of these pages. I hope they will make her proud.

Contents

List of Tables

List of Figures

Chapter 1

Introduction

Helioseismology has been a powerful tool for measuring the structure and rotation of the solar interior. However, there are still many aspects of the Sun's dynamics which are not well understood. This thesis uses the recently developed method of time-distance helioseismology, closely analogous to seismic exploration in geophysics, to search for large-scale flows in the interior of the Sun. With this technique, data from the Michelson Doppler Imager (MDI) have been used to measure the meridional circulation deep in the solar convection zone for the first time. The results show that the measurements are consistent with a meridional circulation which is 20 m/s poleward at the solar surface, and roughly 3 m/s equatorward at the base of the convection zone. The turnover point is just below $r = 0.80\mathrm{R}_\odot$. The meridional circulation is also observed to be varying with time, with the possible appearance of an equatorward surface flow at high latitudes during the rising phase of the solar magnetic cycle. In addition to these important results, the measurements have yielded interesting results for the solar differential rotation, including the possible detection of a highly localized asymmetric feature with an amplitude of 200 m/s.

All of these measurements illustrate the unique capabilities of the time-distance technique for looking at the solar interior in a new way. Furthermore, these results will have a bearing on our understanding of solar dynamics, particularly the solar cycle and the maintenance of the rotation profile.

In the remainder of this chapter, I will discuss large-scale flows, emphasizing those aspects which I believe to be important for understanding the research described in the rest of this dissertation. In section 1.1, I will explain why these measurements are important to our understanding of the Sun and stellar physics in general. Section 1.2 will define some of the terms which are used to describe these flows, and describe the previous observations which are relevant to this work. Finally, in section 1.3 I will briefly summarize the important results contained in this dissertation.

1.1 Large-Scale Flows and Solar Dynamics

The Sun is by far the most studied and well-understood of all the stars in our sky. Scientific observations of the Sun date back to the invention of the astronomical telescope in the first decade of the seventeenth century, when Galileo and other early observers turned their crude early instruments toward the brightest object they could see. With these first observations came the "discovery" and systematic study of sunspots. Almost two hundred years later, it was discovered (Schwabe, 1843) that the number of sunspots visible on the disk of the Sun varied with an eleven-year cycle. Shortly thereafter, Carrington (1858) described what is now known as the *butterfly diagram*, which indicates that sunspots gradually move toward the equator during the progression of the solar cycle.

Despite this long history of observation, the basic puzzle of the eleven-year sunspot cycle is still basically unsolved. Since the work of Hale (1908), it has been known that sunspots are regions of strong magnetic field. In the last few decades it has been shown that all aspects of the solar magnetic field undergo a similar eleven-year cycle. It has also been shown that the cycle is only quasi-periodic, with occasional extended minima. This behaviour has important implications for our technologically advanced civilization, and may even impact on Earth's climate.

Clearly, if we want to understand the solar magnetic cycle we cannot ignore the Sun's dynamics. Flows on the Sun transport mass, energy, momentum and magnetic field from one location to another, and must play an integral role in the solar cycle. Any explanation of the regeneration of the surface magnetic field must also be consistent with the observed flows. Recent models suggest that the main role in this regeneration is played by the Sun's differential rotation, where the angular velocity varies with latitude. However, other flows may also be important for explaining certain aspects of the cycle behaviour.

On a more subtle level, the solar differential rotation is itself a puzzle. How does the Sun maintain a rotation where the angular velocity at the equator is higher than that at the poles? The balance of angular momentum must be acheived through the interplay of meridional and convective motions. Again, models of the Sun's convection and dynamics must be reconciled with the observed velocities.

In this work, my main objective is to measure an aspect of the solar velocity field which has never been measured before: the meridional circulation in the solar interior. The meridional circulation probably has an important role in both the solar dynamo and the angular momentum balance. I will also present some new measurements of the interior rotation. These measurements serve to justify the method, but also contain some hints of interesting new phenomena.

1.2 Previous Observations

1.2.1 Differential rotation

Magnetic feature studies

Recorded observations of sunspots on the solar disk stretch back at least 500 years from the present time. The motion of these features across the solar disk was the first indication that the Sun is a rotating body. A number of observers in the seventeenth and eighteenth centuries observed the rotation of the Sun from the motions of sunspots (see for example Eddy *et al.* (1976)). In 1863 R.C. Carrington published his landmark work *Observations of the Spots on the Sun* from observations made over a period of nine years. In it, he established the orientation of the Sun's rotation axis and defined a heliographic coordinate system that is still in use today, almost 150 years later. Carrington also made the first quantitative measurements of the differential rotation, finding that sunspots at high latitudes have longer rotation periods than those at low latitudes. It is common practice in the literature to desribe the rotation profile with three coefficients,

$$\Omega(\lambda) = A + B\sin^2\lambda + C\sin^4\lambda \tag{1.1}$$

where Ω is the angular velocity and λ is used in this work to refer to the solar latitude.

Most of the early measurements of the Sun's surface flows relied on the same techniques used by Carrington, namely careful observation of sunspots in white-light images. The results have been varied and in some cases confusing. For example, the rotation rates measured by tracking individual sunspots are significantly different from those measured by tracking sunspot *groups* (for examples, see Howard (1984)). Furhermore, large sunspots rotate more slowly than small ones (Howard, 1984), and young sunspots rotate faster than old ones (Zappala and Zuccarello, 1991).

One of the drawbacks of using sunspots as tracers is that the features can exhibit significant evolution during a disk transit, changing in size and shape as time passes. Furthermore, sunspots rarely appear above 30° latitude, and are rare at cycle minina, which makes their spatial and temporal coverage less than ideal.

This last difficulty can be overcome by using magnetic features other than sunspots, such as faculae. Studies of chromospheric and coronal features associated with photospheric magnetic fields stretch back to the early part of this century. Near the equator, such features generally rotate like sunspots (see Howard (1984)); their differential rotation, on the other hand, can be quite different. There is also evidence that the velocity is correlated with feature lifetime and, in some cases, size (Belvedere et al., 1977).

To add to the confusion, the rotation of the large-scale photospheric magnetic field pattern exhibits quite different behaviour. Wilcox and Howard (1970) found that although the field follows a sunspot-like rotation pattern at low latitudes, the velocity is significantly higher than the sunspot rate at higher latitudes. Later investigation (Wilcox et al., 1970) showed that the longest-lived part of the pattern approached a solid-body rotation profile ($B = C = 0$ in equation 1.1).

All of these discrepancies may be related to the extent of the different magnetic features in depth. Since the rotation rate changes with radius, features which are

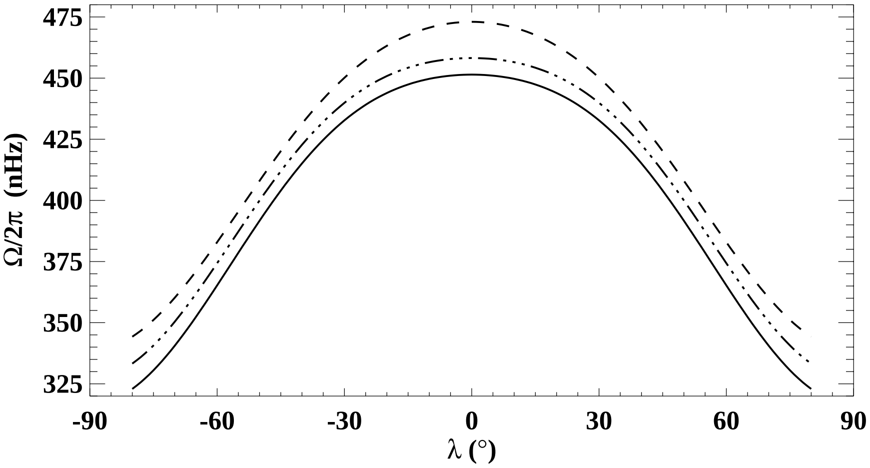

Figure 1.1: Some well-known measurements of the solar surface rotation. The angular frequency $\Omega/2\pi$ is plotted as a function of latitude λ. The solid curve shows a result from Ulrich *et al.* (1988) using direct Doppler measurements from Mount Wilson. The dashed curve is from Snodgrass and Ulrich (1990), using motions of Doppler features; the dash-dot curve is from the same paper, using motions of magnetic features.

rooted at different depths may have different angular velocities[1]. Indeed, measurements using magnetic features all suffer from this ambiguity, since the subsurface structure of the magnetic field is unknown. In order to find the velocity of the photospheric plasma, a spectroscopic approach must be employed.

Surface Doppler measurements

Using the Doppler shift of solar spectral lines, it is possible to measure the line-of-sight velocity of the solar photosphere directly. Because the height of formation of each spectral line is thought to be well-understood, this procedure provides an unambiguous measurement of the velocity of the solar plasma at a particular height. Furthermore, the velocity can be measured at very high latitudes and at any time of the solar cycle, which is an advantage over the use of magnetic tracers.

On the other hand, the determination of the rotation profile from spatially resolved

---

[1] See Beck (2000) for a detailed discussion of this topic.

Doppler observations is a fairly complicated process which is made more difficult by effects such as observer motions, scattered light, and correlations of brightness with velocity. In addition, it is not always possible to unambiguously separate the rotation from the other background velocity fields.

The first attempts to measure the surface motions of the Sun directly from the Doppler effect were made late in the nineteenth century, but the modern era in Doppler measurements began with the invention of the photoelectric spectrograph (Howard and Harvey, 1970). Some of the most precise determinations of the surface rotation profile have been made from very careful analyses of daily observations at Mount Wilson (Snodgrass, 1984; Ulrich et al., 1988). Currently, there are also high-quality data available from the GONG network of instruments (Hathaway et al., 1996). Although the measurements are very precise, there is still significant discrepancy between the different observations. Some of this variation may be solar in origin; in particular, the rotation rate may vary with the solar cycle.

Another way to measure the rotation from Doppler measurements is to observe the motions of "features" in Doppler images. The most common approach is to observe the motions of supergranules. Supergranules are convection cells with a typical size scale of 30 Mm at the solar surface and a typical lifetime of a day. In many ways the measurement of flows using supergranules is much easier than the direct measurement of the surface Doppler velocity (Snodgrass and Ulrich, 1990). Interestingly, the rotation rate as measured using supergranules is significantly faster than that measured from magnetic features or from the direct Doppler observations. This is sometimes interpreted as an indication that the supergranules are "rooted" in layers below the surface which rotate more rapidly than the surface itself.

Figure 1.1 shows some of the most widely quoted measurements of the surface angular velocity, and clearly depicts the differential rotation.

Helioseismic observations

With the advent of helioseismology it became possible to determine the solar rotation profile as a function of radius and latitude[2]. The first such determinations were made in the mid-1980s (Duvall et al., 1984; Brown and Morrow, 1987; Brown et al., 1989). Recent improvements in the accuracy of the observations and in the sophistication of the analysis techniques mean that we can measure the rotation of the convection zone with a precision on the order of 1 nHz (Schou et al., 1998). These results indicate that the angular velocity of the convection zone is roughly a function of latitude alone, with the radiative interior exhibiting a solid-body rotation of about 435 nHz. Betweeen these two regions is a thin layer of strong shear which has been dubbed the *tachocline* (Spiegel and Zahn, 1992). A second region of relatively large radial gradient in the rotation rate is found near the solar surface.

1.2.2 Torsional oscillations

Closely related to the differential rotation is the so-called "torsional oscillation" of the Sun, first observed in 1980 (Howard and LaBonte, 1980) and since confirmed by longer series of measurements (Snodgrass and Howard, 1985b; Snodgrass and Howard, 1985a; Ulrich et al., 1988). The torsional oscillation is a pattern of bands of faster-than-average and slower-than-average rotation. When a constant smooth function of latitude (equation 1.1, for example) is subtracted from the rotation profile, these bands have a residual amplitude of a few metres per second. The peaks in this residual are observed to propagate towards the equator, and the pattern repeats itself on a timescale of $10 - 20$ years. This behaviour is strikingly similar to the well-known butterfly diagram for solar magnetic activity.

Another interesting discrepancy between the expansion in equation 1.1 and the Sun's rotation can be found in the polar regions. With observations at higher spatial resolution and with longer time coverage it has become possible to more accurately determine the rotation rate near the solar poles (Kosovichev and Schou, 1997; Ye and Livingston, 1998). These measurements indicate that the rotation near the poles

---

[2] A brief discussion of the theoretical background will be given in chapter 2.

is in fact significantly slower, compared to the equatorial rate, than would be implied by equation 1.1. There are also indications that this *polar vortex* varies quite substantially during the solar cycle.

Until recently, helioseismology has had relatively little to say about the depth dependence of the torsional oscillation, mainly due to limited latitude resolution (see section 2.2.2). Now, however, instruments like MDI and the GONG network offer the possibility of observing the torsional oscillation below the surface. Kosovichev and Schou (1997) used frequency splittings of the f-mode to show that the bands did have some extent in depth. They also showed that the observed slow rotation near the poles probably persists to some depth also. More recently, Howe *et al.* (2000) and others (Toomre et al., 2000) have been able to observe the torsional oscillation pattern down to a depth of $0.92\,\mathrm{R}_\odot$ using p-modes.

1.2.3 North-south asymmetry in rotation

Some of the surface measurements of the rotation have shown small differences between the rotation rates of the two hemispheres (Howard and Harvey, 1970; Schroter and Vazquez, 1978; Godoli and Mazzucconi, 1979; Arevalo et al., 1982; Howard et al., 1983; Snodgrass, 1983; Komm et al., 1993a). In most cases, the northern hemisphere was found to be rotating slightly more slowly than the southern hemisphere. It is interesting to note that there are also magnetic asymmetries between the two hemispheres, where during the time in question the northern hemisphere has been more magnetically active. The connection between these two observations is not clear, but this asymmetry may be important for both solar-cycle models and for the angular momentum balance of the Sun.

It should be noted that some of the measurement techniques mentioned above cannot be used to measure the difference in rotation between the northern and southern hemispheres. In particular, in the case of global helioseismology, the very accurate frequency-splitting techniques can unambiguously extract only the symmetric component of the angular velocity. This has prevented any measurements of the asymmetry of the internal rotation.

1.2.4 Meridional circulation

The meridional circulation is defined as the flow in meridian planes, which are planes of constant heliographic longitude. To be more precise, I will use the term meridional *flow* to describe any velocity along meridian planes, and meridional *circulation* to describe the axisymmetric (*i.e.* global) component of the flow pattern.

Magnetic feature studies

Like the solar rotation, the meridional circulation was first measured by tracking the motions of sunspots in visible-light images. In the case of the meridional circulation, the small flow velocity makes the measurement even more problematic. If the flow is on the order of 10 m/s, the meridional motion of a sunspot is roughly 10^7m during a disk transit. This corresponds to less than 1% of the solar diameter, an effect which can be swamped by random and systematic motions of the sunspots. As a result, measurements from sunspots have produced widely scattered results: Ribes *et al.* (1985) found alternating poleward and equatorward meridional flows of up to 100 m/s; Howard and Gilman (1986) found a poleward flow of 10 m/s; and Kambry *et al.* (1991) found an equatorward flow of 10 m/s.

Studies using smaller magnetic features are generally more reliable, since the large number of features present reduces the effect of random motions and feature evolution. Most measurements of the meridional flow using these techniques have yielded a poleward flow of about 10 m/s (Komm et al., 1993b; Latushko, 1994; Meunier, 1999)).

As with the tracer measurements of rotation, these observations suffer from an ambiguity of depth. Measurements of Doppler shifts can be used to get a true surface determination.

Surface Doppler measurements

Direct Doppler observations can also reveal the meridional flow of the solar plasma, but again the measurement is much less reliable than measurements of the rotation. The surface motions of the plasma are dominated by the rotation ($\sim$ 2000 m/s) and by small-scale convection ($\sim$ 500 m/s), and acoustic oscillations ($\sim$ 1000 m/s); they are further confused by observational effects like the convective blue shift. The first successful observation of the solar meridional circulation was made by Duvall (1979) using measurements from the Wilcox Solar Observatory. More recently, careful observations from Mount Wilson (LaBonte and Howard, 1982; Ulrich et al., 1988) and from the GONG network (Hathaway et al., 1996) have been successful in measuring the meridional flow more precisely. These observations indicate a poleward flow in both hemispheres, with magnitudes ranging from 10 to 25 m/s. Part of the variation between measurements might be explained by a real time variation of the flow; there have been indications of variation in the meridional circulation with phase of the solar cycle (Komm et al., 1993b; Hathaway, 1996).

It also should be mentioned that in many instances these measurements of the meridional circulation make certain assumptions about the north-south symmetry of the flow, in order to separate it from other, larger flow components with different symmetries. Under this procedure, the velocity determined is the component of the meridional circulation which is antisymetric about the equator (poleward or equatorward), under the assumption that the symmetric (equator-crossing) part is relatively small.

Local helioseismology

Although helioseismology has been extremely successful in measuring the Sun's internal rotation it has only recently been used to measure other velocities. These recent measurements follow the rapid development of *local helioseismology*, techniques which use the local propagation of waves to measure the properties of a relatively small area of the solar interior. Time-distance helioseismology, used for this work, is one of these techniques.

Several such methods have been successfully used to measure meridional flows in the Sun (Patrón et al., 1995; González Hernández et al., 1998; Schou and Bogart, 1998; Basu et al., 1998; Braun and Fan, 1998). Since the measurement of the internal meridional circulation is one of the key results of the work presented here, these other helioseismic measurements are crucial for establishing the validity of the various methods and determining their limitations. Although it is not within the scope of this document to describe these techniques in detail, the above references can be consulted for independent confirmation of some of the results presented here.

1.3 Observations In This Work

This dissertation adds to previous measurements of large-scale flows in the Sun with four key results: the depth and latitude dependence of the meridional circulation in the deep convection zone; the north-south asymmetry of the differential rotation; the time variation of the near-surface meridional circulation during the ascending phase of the solar sycle; and the depth dependence of the torsional oscillation. In addition, appendix A offers a new measurement of the direction of the solar rotation axis.

1.3.1 The deep meridional circulation

The first helioseismic measurement of meridional flow below the solar surface was made using ring diagrams (Patrón et al., 1995); the first measurement of the global component was published by Giles *et al.* (1997). Subsequent measurements of the flow in the near-surface layers (Giles and Duvall, 1998; Braun and Fan, 1998) have confirmed that the poleward flow observed at the surface persists to the limit of observation, with a relatively weak dependence on radius. This thesis contains the extension of these measurements all the way to the base of the solar convection zone. Although the sensitivity to flows at this depth is very small, the measurements are consistent with a single-cell meridional circulation with a surface amplitude of 20 m/s, an equatorward flow at the base of the convection zone with amplitude 3 m/s, and a turnover radius of $r \sim 0.80\mathrm{R}_\odot$.

1.3.2 North-south asymmetry in rotation

Early time-distance measurements (Kosovichev, 1996; Giles and Duvall, 1998; Giles et al., 1998) indicated that the near-surface solar rotation was slightly asymmetric. Such measurements are probably complicated somewhat by observational effects, including the uncertainty in the Carrington elements (see appendix A) and the MDI plate scale uncertainty (section 4.7.2). In this work, however, an interesting and highly localized asymmetry is observed in the rotation profile at a latitude of about 40° and a radius of $0.92\,\mathrm{R}_\odot$. The asymmetry seems to be persistent during two years of observation.

1.3.3 Time variation of meridional circulation

Since the meridional circulation plays an important role in some dynamo models of the solar cycle, the variation of the flow during the cycle is of interest. The observations in this thesis show that there was a significant change in the velocity profile between 1997 and 1998. During this time there was also a significant increase in magnetic activity. Although the measurements at highest latitudes are rather uncertain, it appears that the single-cell pattern observed in 1996 (Giles et al., 1997; Schou and Bogart, 1998) and 1997 changes dramatically, with a possible equatorward surface flow for latitudes above 60°.

1.3.4 Depth variation of torsional oscillation

Although the torsional oscillation is clearly visible at the solar surface, the observations presented here show no indication of a torsional oscillation pattern below $0.95\,\mathrm{R}_\odot$. This contradicts recent results from global analysis which show the pattern down to $0.92\,\mathrm{R}_\odot$. It is possible that the measurements in this work are too noisy to resolve the small velocity signal at that depth.

1.3.5 New Carrington elements

During a search for longitudinal variation of the meridional and zonal flows, it was discovered that the velocities showed strong periodic signals with periods equal to the orbital period of the SOHO spacecraft. Appendix A shows that this variation can be largely explained by a small error in the Carrington elements i_c and Ω_c which describe the direction of the Sun's axis of rotation; the data suggest corrections $\Delta i = -0.091°$, $\Delta\Omega = -0.18°$.

These central results, along with a more complete explanation of their scope and limitations, will be described in the remainder of this dissertation. In chapter 2, I will discuss the technique of time-distance helioseismology as it applies to the measurement of solar flows. In chapter 3, I will briefly describe the Michelson Doppler Imager and the images that are produced by that instrument. The fourth chapter outlines the methods that I have used to analyze those images, including the various interpolation, filtering and fitting procedures. Chapter 4 also includes a discussion of some of the instrumental uncertainties which influence the measurements, and how they have been accounted for. In chapter 5, I will discuss the interpretation of the measurements, in particular the solution of an ill-posed inverse problem to reconstruct the velocity in the solar interior. Chapter 6 will present in more detail the main results outlined in section 1.3; chapter 7 briefly outlines the impact that these results might have on our understanding of the Sun's evolution and dynamics, in particular theories of the solar dynamo and angular momentum balance. The final chapter concludes by summarizing the key results and discusses how this work might be improved and extended in the future.

Chapter 2

Time-Distance Helioseismology

2.1 Solar Oscillations

Solar oscillations were first observed in 1960 by Leighton *et al.* (1960; 1962), who saw ubiquitous vertical motions of the solar photoshere with periods of about 5 minutes and amplitudes of about 1000 m/s. Ten years later, it was suggested that these oscillations might be manifestations of acoustic waves trapped below the photosphere (Ulrich, 1970; Leibacher and Stein, 1971). Deubner (1975) later confirmed this hypothesis by showing that the observed relationship between the spatial and temporal frequencies (see figure 2.1) of the oscillations was close to that predicted by theory. This confirmation marked the birth of helioseismology as a tool for probing the solar interior.

The identification of the solar oscillations with waves trapped in a resonant cavity leads naturally to an analysis in terms of normal modes. In section 2.2 I will briefly describe this formalism and mention some of the earliest helioseismic results. Since this work is concerned with the large-scale dynamics of the Sun, I will describe in slightly more detail the methods used to measure the Sun's internal rotation using a normal mode analysis. After pointing out some of the limitations of this method, section 2.3 will describe the foundations of time-distance helioseismology, the method used in this work, and its application to the measurement of flows.

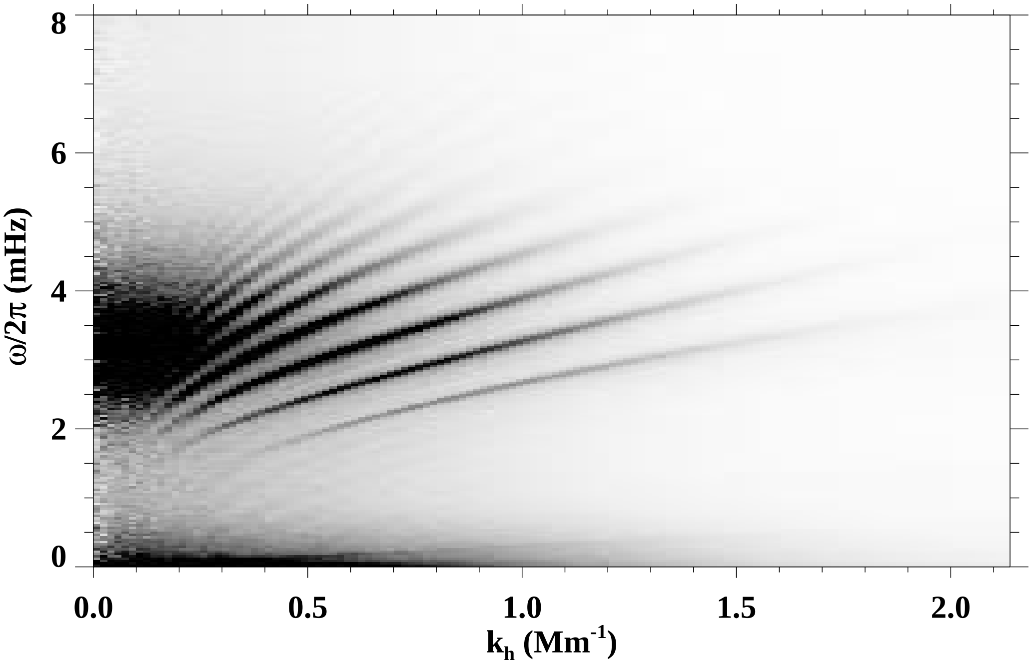

Figure 2.1: The greyscale denotes the power spectrum computed from 8 hours of Dynamics Dopplergrams from MDI. Dark regions are areas of high power. The vertical axis is the temporal cyclic frequency, and the horizontal axis is the horizontal wavenumber. The ridges in the spectrum are regions of resonance which indicate the presence of normal modes of oscillation. The horizontal wavenumber determines the spherical harmonic degree l of the normal mode (see section 2.3.2). The lowest-frequency ridge is the fundamental mode (see section 4.2.3)

2.2 Normal Modes of Oscillation

The Sun forms a resonant cavity for acoustic waves; since the temperature increases with depth, waves which propagate inward from the surface are refracted toward the horizontal and eventually return to the surface. At the surface, they are reflected by the sudden decrease in density. The depth of penetration depends on the horizontal phase speed of the waves.

These oscillations are generally observed by measuring either intensity fluctuations or Doppler motions of the Sun's surface. One way to represent the oscillations is as a sum of standing waves or normal modes, where the signal observed at a point (r, θ, ϕ) at time t is given by

$$f(r, \theta, \phi, t) = \sum_{nlm} a_{nlm} \xi_{nlm}(r, \theta, \phi) \exp(i[\omega_{nlm} t + \alpha_{nlm}]). \tag{2.1}$$

In this equation, the three integers n, l, and m identify each mode and are commonly called the *radial order*, *angular degree*, and *azimuthal order* respectively. For each mode, a_{nlm} is the mode amplitude, ω_{nlm} is the eigenfrequency, and α_{nlm} is the phase.

The spatial eigenfunction for each mode is denoted by ξ_{nlm}. For a spherically symmetric Sun, the eigenfunctions can be separated into radial and angular components:

$$\xi_{nlm}(r, \theta, \phi) = \xi_{nl}(r) Y_{lm}(\theta, \phi), \tag{2.2}$$

where Y_{lm} is the spherical harmonic and the radial eigenfunction is denoted now by $\xi_{nl}(r)$.

The surface manifestation of solar oscillations can therefore be decomposed into a sum of spherical harmonics for each instant of observation. The result is that the power spectrum of the acoustic signal shows resonant peaks at a particular set of temporal frequencies for each pair (n, l). These peaks identify the eigenfrequencies ω_{nlm} of the normal modes, which can then be used as a diagnostic of the solar interior.

The basic procedure is to identify the eigenfrequencies for a set of normal modes, and then to "invert" these measurements for some property (for example, the sound speed) of the solar interior. In the earliest days of helioseismology, the frequencies were interpreted using simple models and analytical formulae derived from asymptotic analysis. For example, Deubner's measurements implied that the solar convection zone was significantly deeper than predicted by standard models of the day (Gough, 1976). Helioseismology also put an important constraint on the solar helium abundance (Christensen-Dalsgaard and Gough, 1980). More quantitative results were later derived from sophisticated inverse methods.

In a spherically symmetric Sun, all the modes with the same n and l would have the same eigenfrequency ω_{nl}, regardless of the value of $m = \{-l, -l+1, ..., l-1, l\}$. The

Sun, however, is not spherically symmetric, which causes this $(2l+1)$-degeneracy in the frequencies to be broken. This splitting of the frequencies is the basis for helioseismic measurements of the solar internal rotation.

2.2.1 Measuring rotation with mode frequencies

The most obvious symmetry breaker is rotation about a fixed axis. The Sun's rotation causes a splitting of the m-degeneracy in frequency which can be described by

$$\Delta\omega_{nlm} = m \int K_{nlm}(r,\theta)\Omega(r,\theta)\, r\, dr\, d\theta \tag{2.3}$$

Here $\Omega(r,\theta)$ is the angular velocity in the solar interior, $\Delta\omega_{nlm}$ is the frequency difference between the rotating and non-rotating case, and the rotation kernel $K_{nlm}(r,\theta)$ is a weighting function which describes the sensitivity of the mode (n,l,m) to different regions of the solar interior. The kernels are determined by the structure of the eigenfuntions $\xi_{nlm}(r,\theta,\phi)$ in equation 2.2.

In practice, the measured frequency splitting as a function of m and l is often parametrized as an expansion in terms of Legendre polynomials[1]

$$\omega'_{lm} \equiv \bar{\omega}(l,m) - \bar{\omega}(l,0) = l \sum_{k=0}^{k_{max}} a_l^k P_k\left(\frac{m}{l}\right). \tag{2.4}$$

In this expansion, the rotation contributes only to the odd-k a-coefficients, whereas the even-k a-coefficients for each l arise from aspherical effects which cannot distinguish east from west (Brown and Morrow, 1987).

2.2.2 Limitations of the global approach

As noted in section 1.2.1, helioseismic measurements of the solar rotation have become incredibly precise. However, there are several ways in which this approach to the problem is somewhat limited.

---

[1] Other possibilites exist and are also used.

First, the approach is inherently global. This results in a high precision of measurement but is also an important limitation. In equation 2.3, the frequency splitting is shown to be related to the internal angular velocity through the sensitivity kernels K_{nlm}. Because of the symmetry of the mode eigenfunctions, all the kernels K_{nlm} are symmetric about the equatorial plane. Therefore one consequence of the global approach is that the frequency splitting is sensitive only to that part of Ω which is symmetric about the equatorial plane. Furthermore, since the spherical harmonics depend on longitude ϕ only through $e^{im\phi}$, the kernels are also independent of longitude. Any variations in the angular velocity due to, for example, active regions, are therefore hidden.

Second, until recently the resolution in latitude has been somewhat limited. This resolution is basically limited by the value of k_{max} in equation 2.4. Signal-to-noise considerations have meant that most early results from ground-based observations were limited to $k_{max} = 5$; the resulting rotation profile had three independent points in latitude. This limitation has been largely removed with the advent of the GONG network and the SOHO spacecraft, as frequency splittings are now being extracted for larger values of k_{max} (sometimes up to 35). This higher resolution is needed to resolve small-scale structures like the torsional oscillation.

Third, as noted in the previous section, all the spherically asymmetric effects other than rotation — magnetic fields, structural asphericity, and meridional circulation, for example — cause a splitting of the normal mode frequencies which appears in the even a-coefficients of expansion 2.4. Thus, it is impossible to disentangle any one of these effects from the others (Zweibel and Gough, 1995).

2.3 Time-Distance Helioseismology

Solar oscillations are essentially the only tool astronomers have for looking into the interior of the Sun. Naturally, with the successes of helioseismology on global scales, solar physicists were intrigued by the possibilty of probing the solar interior on smaller scales. Some of the earliest work in this area involved measurements of the interaction between acoustic waves and sunspots (Braun et al., 1988). More recently, there has been a great interest in using propagating waves to measure the meridional circulation and other flows. The local approach hopes to be complementary to the global approach by overcoming some of the limitations outlined in section 2.2.2.

The various local methods all rely on the interaction of traveling acoustic waves with small perturbations to the background state. Although it is not within the scope of this document to describe all of these methods in detail, each one has its own assumptions, advantages, and disadvantages. The time-distance approach, which is the method used in this work, is described here.

2.3.1 Wave travel times

In the time-distance approach to helioseismology the key concept is the notion of wave travel time. Travel time is a familiar concept in geophysics, where waves are generally excited at specific sources which are localized in space and time. On the Sun, the excitation of acoustic waves is stochastic and it is not yet possible to isolate individual sources in space or time[2]. However, as Duvall (1993) postulated, it is still possible to measure wave travel times[3]. This is done by computing the temporal cross covariance of the signal at a point on the solar surface with the signal at another point.

The *cross covariance* function of the oscillation signals f for two points at coordinates $\mathbf{r_1}$ and $\mathbf{r_2}$ on the solar surface is defined as the integral

$$\psi(\tau,\Delta) = \int_0^T f(\mathbf{r_1}, t+\tau) f^*(\mathbf{r_2}, t)\, dt. \tag{2.5}$$

Here Δ is used to denote the angular distance between the two points and T is the total length of the observations. The time delay τ measures the amount that one signal is shifted relative to the other. The difference between ψ and the *cross correlation* function is a difference of normalization. In this work, all the computed

---

[2] In one case wave generation due to a solar flare has actually been observed directly (Kosovichev and Zharkova, 1998).

[3] A similar idea was proposed in geophysics by Claerbout (1976).

cross covariances have been normalized according to

$$\psi_0(\tau,\Delta) \equiv \frac{\psi(\tau,\Delta)}{\psi(0,0)} \tag{2.6}$$

where the term in the denominator is computed by setting $\mathbf{r_1} = \mathbf{r_2}$ and $\tau = 0$ in equation 2.5. I will refer to this function as the cross correlation; however, the exact normalization is almost always irrelevant in time-distance helioseismology.

In practice, it is quite time-consuming to compute the cross correlation with the integral in equation 2.5. Fortunately, the correlation theorem (see, for example, Bracewell (1986)) allows us to change the integral into a product in the Fourier domain,

$$\Psi(\omega_\tau,\Delta) = F(\mathbf{r_1},\omega)\, F^*(\mathbf{r_2},\omega). \tag{2.7}$$

Here Ψ is used to represent the temporal (τ) Fourier transform of ψ, and F represents the temporal Fourier transform of f. The length T of the observations is assumed to be long compared to any time lag τ of interest. Since Fourier transforms can be computed very efficiently, equation 2.7 provides a relatively fast way to compute cross correlations.

Assuming that the oscillation signal f can be written in the form of equation 2.1, the Fourier transform F of the observed oscillation signal is given by

$$F(\omega, R_\odot, \theta, \phi) = \sum_{nlm} a_{nlm}\xi_{nl}(R_\odot)Y_{lm}(\theta,\phi)e^{-i\alpha_{nlm}}\delta(\omega-\omega_{nlm}). \tag{2.8}$$

Here the solar surface is denoted by $r = R_\odot$. In practice, the power spectrum of solar oscillations is band-limited. For convenience, let us assume that the amplitudes depend on n and l in the following way:

$$\begin{aligned}\sum_{nlm} a_{nlm}\xi_{nl}(R_\odot)Y_{lm}(\theta,\phi)e^{-i\alpha_{nlm}}\delta(\omega-\omega_{nlm}) &= \\ \sum_{nlm} G_l(\omega_{nl})Y_{lm}(\theta,\phi)e^{-i\alpha_{nlm}}\delta(\omega-\omega_{nlm}),&\end{aligned} \tag{2.9}$$

where

$$G_l^2(\omega) = \sqrt{2l+1}\exp\left(-\frac{(\omega-\omega_0)^2}{\delta\omega^2}\right). \tag{2.10}$$

If I then compute the product in equation 2.7 and perform the inverse Fourier integral, the result is

$$\psi(\tau,\Delta) = \sum_{nl} G_l^2(\omega_{nl}) e^{i\omega_{nl}\tau} \sum_m \sum_{m'} Y_{lm}(\theta_1,\phi_1) e^{i\alpha_{nlm}} Y_{lm'}^*(\theta_2,\phi_2) e^{-i\alpha_{nlm'}}. \tag{2.11}$$

Since the phases are random, I will assume that on average the terms $e^{i(\alpha_{nlm}-\alpha_{nlm'})}$ will tend to cancel, except of course when $m = m'$. In this case, equation 2.11 becomes

$$\psi(\tau,\Delta) = \sum_{nl} G_l^2(\omega_{nl}) e^{i\omega_{nl}\tau} \sum_m Y_{lm}(\theta_1,\phi_1) Y_{lm}^*(\theta_2,\phi_2). \tag{2.12}$$

The addition theorem for spherical harmonics (see for example Jackson (1975)) allows the simplification

$$\psi(\tau,\Delta) = \sum_{nl} G_l^2(\omega_{nl}) e^{i\omega_{nl}\tau} \left(\frac{2l+1}{4\pi}\right) P_l(\cos\Delta), \tag{2.13}$$

where Δ is the distance between the two points (θ_1,ϕ_1) and (θ_2,ϕ_2):

$$\cos\Delta = \cos\theta_1\cos\theta_2 + \sin\theta_1\sin\theta_2\cos(\phi_1-\phi_2), \tag{2.14}$$

and P_l is the Legendre polynomial of order l.

Again following Jackson (1975), I can approximate

$$P_l(\cos\Delta) \simeq J_0\left([2l+1]\sin\frac{\Delta}{2}\right) \simeq \sqrt{\frac{2}{\pi L\Delta}}\cos\left(L\Delta - \frac{\pi}{4}\right), \tag{2.15}$$

where J_0 is the Bessel function of the first kind. I have introduced the new symbol $L \equiv l + 1/2$; these approximations are valid where Δ is small, but $L\Delta$ is large. Then I have

$$\psi(\tau,\Delta) = \sum_{nl} \frac{2}{\sqrt{\pi\Delta}} \exp\left(-\frac{(\omega_{nl}-\omega_0)^2}{\delta\omega^2}\right)\cos(\omega\tau)\cos(L\Delta). \tag{2.16}$$

Now the double sum can be reduced to a convenient sum of integrals if we regroup the modes so that the outer sum is over the ratio $v \equiv \omega/L$ and the inner sum is over ω. I will show in section 2.3.2 that the travel distance Δ of an acoustic wave is determined by the ratio v; Δ is otherwise independent of ω. In this case, given the band-limited nature of the function G, only values of L which are close to $L_0 \equiv \omega_0/v$ will contribute to the sum, and I expand L near the central frequency ω_0:

$$L\Delta \simeq \Delta \left[L(\omega_0) + \frac{\partial L}{\partial \omega}(\omega - \omega_0) \right] = \Delta \left[\frac{\omega_0}{v} + \frac{\omega - \omega_0}{u} \right], \qquad (2.17)$$

where $u \equiv \partial\omega/\partial L$. Furthermore, the product of cosines in equation 2.16 can be changed into a sum; one term is

$$\cos \left[\left(\tau - \frac{\Delta}{u} \right) \omega + \left(\frac{1}{u} - \frac{1}{v} \right) \Delta\omega_0 \right], \qquad (2.18)$$

and the other term is identical except that τ has been replaced with $-\tau$ (*i.e.* the time lag is negative). The result is that the double sum in equation 2.16 becomes

$$\psi(\tau, \Delta) = \sum_v \frac{2}{\sqrt{\pi\Delta}} \sum_\omega \exp\left(-\frac{(\omega - \omega_0)^2}{\delta\omega^2} \right) \cos\left(\left[\pm\tau - \frac{\Delta}{u} \right] + \left[\frac{1}{u} - \frac{1}{v} \right] \Delta\omega_0 \right). \quad (2.19)$$

The inner sum can be approximated by an integral over ω; it can be shown (see Gradshteyn and Ryzhik (1994)) that

$$\int_{-\infty}^{\infty} d\omega \, \exp\left(-\frac{(\omega - \omega_0)^2}{\delta\omega^2} \right) \cos\left(\left[\tau - \frac{\Delta}{u} \right] \omega - \left[\frac{1}{u} - \frac{1}{v} \right] \Delta\omega_0 \right) =$$
$$\sqrt{\pi\, \delta\omega^2} \exp\left(-\frac{\delta\omega^2}{4} \left[\tau - \frac{\Delta}{u} \right]^2 \right) \cos\left(\omega_0 \left(\tau - \frac{\Delta}{v} \right) \right). \qquad (2.20)$$

The limits $(-\infty, \infty)$ pose no particular problem since the amplitude function G^2 is essentially zero for very large and very small frequencies. Finally, then, the cross correlation can be expressed as

$$\psi(\tau, \Delta) \propto \sum_v \exp\left(-\frac{\delta\omega^2}{4} \left[\tau \pm \frac{\Delta}{u} \right]^2 \right) \cos\left(\omega_0 \left[\tau \pm \frac{\Delta}{v} \right] \right) \qquad (2.21)$$

The cross correlation function at any particular distance is thus described by two characteristic times; the *group time*, defined as $\tau_g \equiv \Delta/u$, and the *phase time*, defined as $\tau_p \equiv \Delta/v$. Furthermore, the cross correlation will have two peaks; one near $+\tau_g$, and the other near $-\tau_g$. These two peaks correspond to the two directions of propagation.

A note is necessary here regarding this rather inelegant derivation of equation 2.21. Several assumptions have been made in the derivation which may not be exactly satisfied in the Sun. Furthermore, I will use the final result in regions well outside the range of validity of the small-angle approximation in equation 2.15. However, these difficulties should not obscure the fact that the form of 2.21 gives a very accurate description of the measured cross correlation! Mathematical details aside, this practical consideration was in fact the original justification for the use of this formula in time-distance helioseismology.

In interpreting the phase and group times in the cross correlation, it is necessary to model the propagation of acoustic waves in the Sun. For this work and almost all time-distance results to date, the propagation is modeled with the ray approximation.

2.3.2 The ray approximation

The acoustic waves observed in this work can be considered high-frequency acoustic waves. In most of the region in which these waves are confined, their wavelengths are short compared to the local temperature and density scale heights. In this wavelength regime, the wave propagation can be approximated with ray theory.

Calculating ray paths

Calculation of ray paths (D'Silva and Duvall, 1995; Gough, 1984) begins with the local dispersion relation, which for the Sun can be written as

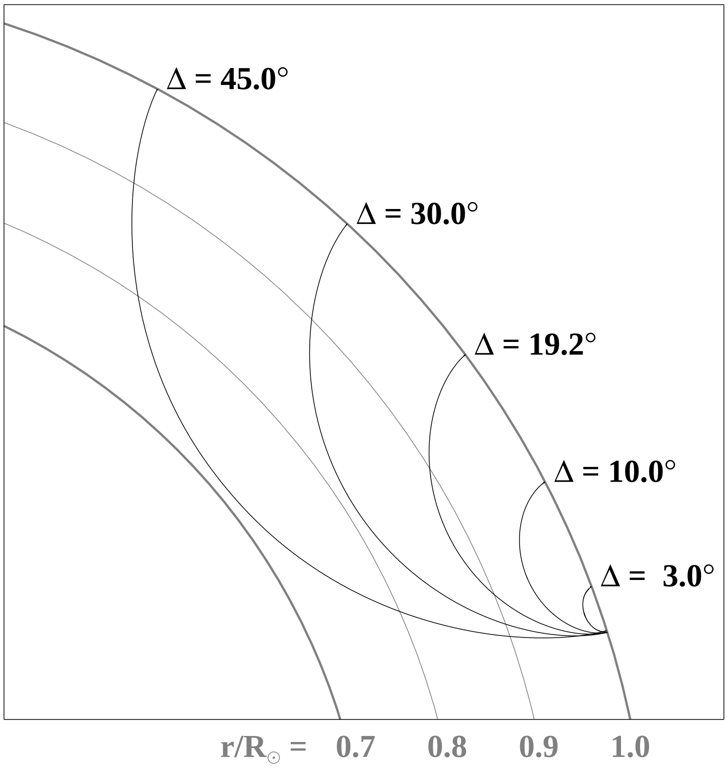

Figure 2.2: A great circle plane containing several sample rays. The grey arcs indicate the fractional radius, and the five black curves show the path taken by waves propagating in the convection zone. The largest ray shown travels a distance of 45° and reaches to $r = 0.71\,\mathrm{R}_\odot$; this is the largest distance for which cross correlations were computed in this work.

$$\begin{aligned} k_r^2 &= \frac{1}{c^2}\left(\omega^2 - \omega_{AC}^2\right) - k_h^2\left(1 - \frac{\omega_{BV}^2}{\omega^2}\right), \\ k_h^2 &= \frac{L^2}{r^2}. \end{aligned} \tag{2.22}$$

The quantity k_h is the horizontal wavenumber; the relation (rk_h = constant) follows from spherical symmetry of the background state. In the modal analysis, it can be shown that $L^2 = l(l+1)$; for large l, $L \simeq (l+1/2)$ and is the same as the variable L from section 2.3.1.

The symbol k_r denotes the radial wavenumber, c is the sound speed, and the quantity ω_{BV}, called the Brunt-Väisälä frequency, is given by

$$\omega_{BV}^2 = g\left(\frac{1}{\Gamma_1}\frac{d\ln p}{dr} - \frac{d\ln\rho}{dr}\right), \tag{2.23}$$

where g is the acceleration due to gravity at radius r. The other characteristic frequency is the acoustic cutoff frequency, for which I use the approximation

$$\omega_{AC}^2 = \frac{c^2}{4H_p^2} \tag{2.24}$$

where H_p is the pressure scale height, defined as

$$H_p = -\left(\frac{d\ln p}{dr}\right)^{-1}. \tag{2.25}$$

The path of an acoustic ray is defined by the equation

$$\frac{dr_p}{r_p\,d\theta_p} = \frac{v_{gr}}{v_{gh}}, \tag{2.26}$$

where the coordinates (r_p, θ_p) describe the path of the ray within a plane containing the center of the Sun. Using the dispersion relation for solar acoustic waves, the radial (v_{gr}) and horizontal (v_{gh}) components of the group velocity can be expressed as

$$\begin{aligned} v_{gr} &\equiv \frac{\partial\omega}{\partial k_r} = \frac{k_r\omega^3c^2}{\omega^4 - k_h^2c^2\omega_{BV}^2}, \\ v_{gh} &\equiv \frac{\partial\omega}{\partial k_h} = k_h\omega c^2\left(\frac{\omega^2-\omega_{BV}^2}{\omega^4 - k_h^2c^2\omega_{BV}^2}\right), \end{aligned} \tag{2.27}$$

In practice, a solar model (Christensen-Dalsgaard et al., 1996) is used to calculate the characteristic frequencies (2.23 and 2.24), and these are used in turn to calculate the horizontal and radial wavenumbers (equation 2.22) and group velocities (2.27). The *turning points* of the ray are defined as those points where the radial wavenumber (and hence the group velocity) goes to zero. Roughly speaking, since $\omega_{BV}^2 \ll \omega^2$ in the convection zone, and $\omega_{AC}^2 \ll \omega^2$ except very near the surface, the upper turning

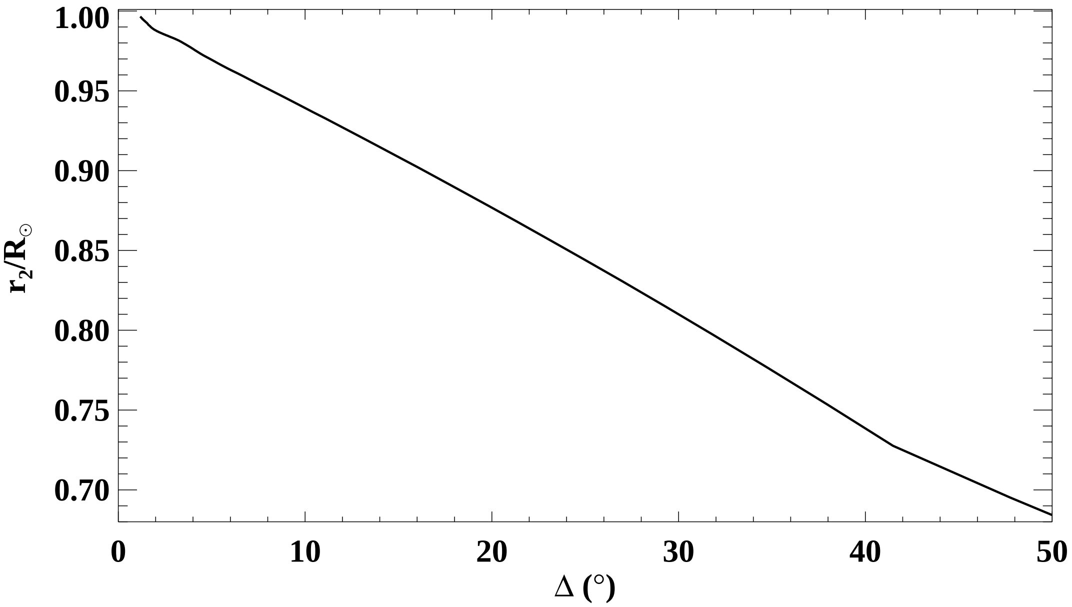

Figure 2.3: The lower turning point r_2 is plotted as a function of the travel distance for acoustic rays with temporal frequency $\omega/2\pi = 3.1\,\mathrm{mHz}$.

point (which I denote by r_1) occurs where $\omega \approx \omega_{AC}$, and the lower turning point (r_2) occurs where $\omega \approx k_h c$. This latter statement leads to the approximate determination of r_2:

$$\frac{c(r_2)}{r_2} \simeq \frac{\omega}{L}. \tag{2.28}$$

This implies that all waves with the same value of ω/L follow the same ray path, a fact that I made use of in section 2.3.1.

Once the turning points have been determined, the angular coordinate θ_p is computed from the integral of equation 2.26:

$$\theta_p(r) = \theta_1 + \int_{r_1}^{r} \frac{v_{gh}(r')}{v_{gr}(r')} \frac{dr'}{r'}, \tag{2.29}$$

where the turning points are defined as (r_1, θ_1) and (r_2, θ_2). Figure 2.2 shows some sample ray paths. The travel distance of the ray is defined as the angular distance between photospheric reflection points,

$$\Delta \equiv 2|\theta_2 - \theta_1|. \tag{2.30}$$

The relationship between travel distance and turning point depth is shown in figure 2.3. The group travel time can be defined as

$$\tau_g \equiv \int_\Gamma \frac{ds}{v_g} = 2\int_{r_1}^{r_2} \frac{dr}{v_{gr}}, \tag{2.31}$$

where the first integral is a line integral along the ray path (denoted by ,). The phase time can be defined similarly as

$$\tau_p = \int_\Gamma \frac{k\,ds}{\omega} = \int_\Gamma \frac{ds}{v_p}. \tag{2.32}$$

The integrands in equations 2.29, 2.31 and 2.32 are singular at the turning points r_1 and r_2, but the singularities are integrable. For the purposes of numerically performing the integrals, I have used the procedure outlined by Christensen-Dalsgaard *et al.* (1989).

In what follows, I will deal almost exclusively with phase time as defined by equation 2.32. I will leave off the subscript p unless it is ambiguous to do so.

Fermat's Principle

A powerful property of ray paths is that they obey Fermat's Principle, which states that the travel time along the ray is stationary with respect to small changes in the path. This implies that if a small perturbation is made to the background state, the ray path is unchanged.

The perturbation to the travel time can then be expressed as

$$\tau - \tau_0 = \frac{1}{\omega}\int_{\Gamma_0} \delta k\,ds. \tag{2.33}$$

Here δk is the perturbation to the wavevector due to inhomogeneities in the background state, and Fermat's principle allows us to make the integral along the unperturbed ray path Γ_0 (see, for example, Gough (1993)).

In the solar convection zone, the Brunt-Väisälä frequency ω_{BV} is small compared to the acoustic cutoff frequency and the typical frequencies of solar oscillations. Neglecting this frequency, the dispersion relation 2.22 can be written as

$$\begin{aligned} k_r^2 &= \frac{1}{c^2}\left(\omega^2 - \omega_{AC}^2\right) - k_h^2, \\ k_h^2 &= \frac{l(l+1)}{r^2}. \end{aligned} \tag{2.34}$$

If we allow small perturbations (relative to the background state) in ω, c^2, and ω_{AC}^2, then the integrand in equation 2.33 can be written to first order as

$$\frac{\delta k \, ds}{\omega} = \left[\frac{\delta\omega}{c^2 k} - \left(\frac{\delta c}{c}\right)\frac{k}{\omega} - \left(\frac{\delta\omega_{AC}}{\omega_{AC}}\right)\left(\frac{\omega_{AC}^2}{c^2\omega^2}\right)\frac{\omega}{k}\right] ds, \tag{2.35}$$

where I have neglected terms which are second-order in $\delta c/c$ and $|u|/c$.

One possible perturbation to the spherically symmetric background state is a velocity field. If the flow field is described by $\mathbf{u}$ then the observed frequency will be Doppler shifted by the advection of the oscillations,

$$\delta\omega = -k\hat{\mathbf{n}} \cdot \mathbf{u}, \tag{2.36}$$

so that equation 2.33 becomes

$$\tau^{\pm} - \tau_0 = -\int_{\Gamma_0}\left[\frac{\mathbf{u}\cdot(\pm\hat{\mathbf{n}})}{c^2} + \left(\frac{\delta c}{c}\right)\frac{k}{\omega} + \left(\frac{\delta\omega_{AC}}{\omega_{AC}}\right)\left(\frac{\omega_{AC}^2}{c^2\omega^2}\right)\frac{\omega}{k}\right] ds, \tag{2.37}$$

where $\hat{\mathbf{n}}$ is a unit vector tangent to the ray path. Here I have defined the quantity τ^+ as the perturbed travel time in one direction along the ray path (unit vector $+\hat{\mathbf{n}}$) and τ^- as the perturbed travel time in the opposite (reciprocal) direction (unit vector $-\hat{\mathbf{n}}$). To separate the effects of the velocity field from the other perturbations, we thus define

$$\begin{aligned} \delta\tau \equiv \tau^{+} - \tau^{-} &= -2\int_{\Gamma_0} \frac{\mathbf{u}\cdot\hat{\mathbf{n}}}{c^2}\, ds & (2.38) \\ \langle\tau\rangle \equiv \frac{(\tau^{+} + \tau^{-})}{2} &= \tau_0 - \int_{\Gamma_0} \left[\left(\frac{\delta c}{c}\right)\frac{k}{\omega} + \left(\frac{\delta\omega_{AC}}{\omega_{AC}}\right)\left(\frac{\omega_{AC}^2}{c^2\omega^2}\right)\frac{\omega}{k}\right] ds. & (2.39) \end{aligned}$$

Equation 2.38 thus provides the link between the measured travel time differences and the flow field along the ray path. This simple equation will be the heart of the measurements made in this work. The quantities δc and $\delta\omega_{AC}$ contain effects such as perturbations to the temperature and magnetic field[4], which appear in the mean times.

2.3.3 Horizontal and radial flows

Equation 2.38 shows that the time difference $\delta\tau$ for waves traveling on reciprocal ray paths is sensitive to the component of the flow along the ray path. If the radial flow is uniform everywhere, then the net time difference due to the radial velocity will be zero, as reciprocal rays will experience the same net flow. However, it may be the case that the radial component of the velocity is not uniform; imagine a ray path which lies in a meridian plane with a velocity field like the one shown in figure 2.4. This model circulation is horizontal at the surface and satisfies the continuity equation

$$\frac{\partial\rho}{\partial t} + \nabla\cdot(\rho\mathbf{u}) = 0. \qquad (2.40)$$

Since the density in the solar convection zone deceases quite rapidly with radius, a meridional circulation which satisfies conservation of mass must have a small radial component.

---

[4] Strictly speaking, in the presence of a magnetic field the sound speed c should be replaced by the fast magnetoacoustic speed c_f in equation 2.34. See Kosovichev and Duvall (1997) for more details. In this section I am including magnetic effects as perturbations to the quantity c. For further development of the perturbations to the mean times due to magnetic field, see also Ryutova and Scherrer (1998).

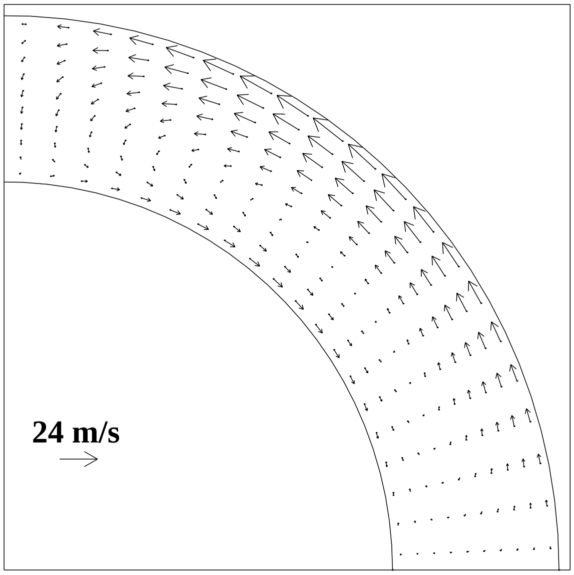

Figure 2.4: A meridional cross section of the solar convection zone. The bottom of the plot represents the equatorial plane. The arrows denote a possible meridional circulation, with the reference length shown in the lower left representing a velocity of 24 m/s. The model shown here satisfies the continuity equation and is horizontal at the solar surface.

We can write the time difference in two components

$$\delta\tau = \delta\tau_h + \delta\tau_r, \tag{2.41}$$

where

$$\begin{aligned} \delta\tau_h &= 2\int_{r_1}^{r_2} \frac{u_h v_{gh}}{v_{gr} c^2} dr, &(2.42)\\ \delta\tau_r &= 2\int_{r_1}^{r_2} \frac{u_r}{c^2} dr. &(2.43) \end{aligned}$$

Using these equations, it is possible to calculate the relative contributions of the horizontal and radial flows for a selection of latitudes and distances. The results are

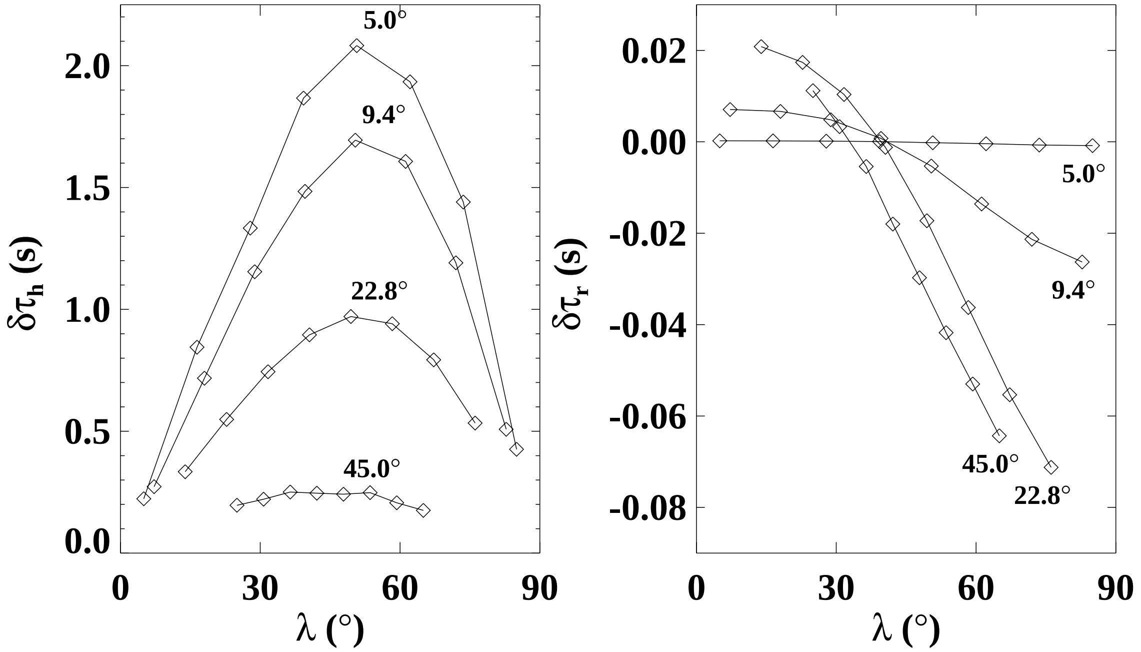

Figure 2.5: The two plots show travel time differences computed using the model in figure 2.4. The left-hand plot shows the time differences due to the horizontal part of the meridional circulation, and the right-hand plot shows the contribution of the radial part of the velocity. The curves in each plot are labelled with their travel distance. Note the different scales in the two plots.

shown in figure 2.5. Since the contribution of the radial flow is always much smaller than the contribution of the horizontal flow, I will always neglect the former; the symbol u will hereafter be used to denote the horizontal flow field. Equation 2.38 can then be replaced by

$$\delta\tau = 2\int_{r_1}^{r_2} \frac{u v_{gh}}{v_{gr} c^2} dr, \tag{2.44}$$

which is used to infer the velocity u from the time differences, as explained in chapter 5.

2.3.4 Wave Effects

Clearly the ray approximation is extremely useful in time-distance helioseismology. However, it is often questioned whether this approximation is entirely justified (see for example Bogdan (1997)). On theoretical grounds, the ray expectation is invalid in the region near the solar surface, where the pressure and density scales vary rapidly. This means that the approximation is worse for very short travel distances where the waves propagate only in the near-surface region. As the travel distance increases, the rays penetrate to depths where the variation of the background is much slower, and the approximation is expected to work quite well.

One important consequence of wave effects is that the travel time is sensitive not only to the local velocity field along the ray path, but also to conditions in the surrounding medium as well. This "broadening" has been clearly demonstrated by Bogdan (1997). In practice, this effect is probably not as important as it might seem at first glance. In almost all time-distance measurements, travel times are averaged over a small range of travel distances and locations. That is, cross correlations are computed for a large number of pairs of points, and then pairs with "similar" distances and locations have their cross correlations averaged together to get a single measurement $\delta\tau$. In interpreting this measurement, then, the ray path used is actually a "ray bundle" consisting of a number of rays covering the region of propagation. The broadening of such a bundle by wave effects might be small compared to the extent of the bundle itself. Some critics of the ray approximation seem to miss this subtlety.

Another possible consequence of wave effects is that the sensitivity along the ray path might be different from that predicted by the ray theory. Some numerical simulations have shown this to be true, with the sensitivity actually being slightly lower along the ray path than in the nearby regions (Birch, 1999). Some work is currently being done to compute more realistic sensitivity functions, using various more general approximations to the wave equation (Jensen et al., 1998). These models will probably play an important role in the future development of time-distance helioseismology.

Finally, let me make the point that ray theory has been used in helioseismology for some time (see, for example, Gough (1984)). The ray approximation is one of several methods that have been applied to *asymptotic inversions* of helioseismic frequency measurements. In many cases, these analytic methods have been shown to be in very good agreement with more sophisticated numerical techniques which include the full wave nature of the oscillations.

So far, this discussion has glossed over the actual observation and measurement of acoustic wave travel times or even of solar oscillations in general. This question leads to considerations of a more practical nature, which will be expanded in the next two chapters. Chapter 3 describes the MDI instrument and the helioseismic observations it makes. Chapter 4 describes the subsequent analyses which are necessary to extract travel times using the time-distance approach.

Chapter 3

The Michelson Doppler Imager on SOHO

The Michelson Doppler Imager (hereafter referred to as MDI) is an instrument designed to probe the interior of the Sun by measuring the photospheric manifestations of solar oscillations[1]. The MDI observables include line and continuum intensity, magnetic field strength, and line-of-sight (Doppler) velocity. Although it is possible to use intensity images of the Sun for the purposes of time-distance helioseismology — in fact, the first ever application of the method was made with intensity images (Duvall et al., 1993) — the technique has been more commonly applied to velocity images. A *Dopplergram* is an image where the value of each pixel is a measurement of the line-of-sight velocity of the surface of the Sun. The rest of this chapter briefly describes the MDI instrument and the production of Dopplergrams.

3.1 The SOHO Spacecraft

The Solar and Heliospheric Observatory (SOHO) is a spacecraft constructed, launched, and operated under the joint auspices of the European Space Agency (ESA) and the National Aeronautics and Space Administration (NASA). SOHO

---

[1] For a more detailed description of the MDI instrument see Scherrer *et al.* (1995) and the MDI Web site at `http://soi.stanford.edu/`.

was launched in December, 1995 and placed in a halo orbit about the Earth-Sun L_1 Lagrange point. From this vantage point (about 1.5×10^6 km sunward of the Earth), SOHO has an uninterrupted view of the Sun, and a small and slowly changing spacecraft-Sun velocity.

SOHO carries a payload of a dozen instruments[2], which can be divided into three broad categories (Domingo and Fleck, 1995): remote sensing of the solar atmosphere, *in situ* measurement of the solar wind, and helioseismology.

The spacecraft was designed for an initial mission duration of two years, but with sufficient on-board fuel for up to six years. The instruments and spacecraft components were designed and tested for a six-year lifetime as well. At the time of this writing, the spacecraft continues to operate, almost four years after launch. Most of the observations used in this dissertation were made between May, 1996 and June, 1998, at which time flight engineers lost contact with SOHO. They were able to reacquire spacecraft control only after several months of painstaking effort, so there is a considerable gap in the helioseismic record.

SOHO is three-axis stabilized, with the means to control the pointing, roll angle, and orbital motion quite accurately. When operating with its full capabilities, the spacecraft has its optical axis pointing at the center of the Sun, with an accuracy of better than 10 arcseconds over six months and 1 arcsecond over fifteen minutes. The roll of the spacecraft is maintained such that the Sun's axis of rotation is always contained in the spacecraft XZ plane; in practical terms, this means that the effective position angle[3] of MDI images is always zero. The roll error is less than 1.5 arcminutes over fifteen minutes.

3.2 MDI

SOHO offers an unprecedented opportunity for helioseismologists because of the uninterrupted observation, the lack of intervening atmosphere, and the relatively long

---

[2] Further information about SOHO and its instruments can be found on the World Wide Web at `http://sohowww.nascom.nasa.gov/`.

[3] See also appendix A.

observation time. MDI, along with the other helioseismology instruments on SOHO, has been designed to take advantage of that opportunity.

MDI is based on a modification of the Fourier Tachometer technique (Brown, 1980; Evans, 1980). A refracting telescope feeds sunlight through a series of filters onto a charge-coupled device (CCD) camera. The optical elements in the filter system include the front window, the blocker, the Lyot filter, and two tunable Michelson interferometers.

The fixed filters have bandpasses centered on the nickel (Ni) absorption line at 6768 angstroms, which is formed near the middle of the photosphere. The front window bandpass has a full width at half maximum of 50 Å, and also efficiently blocks infrared radiation. It is the only filtering element which is not located inside the temperature-controlled oven. The second element in the filter system, the blocker, has an 8 Å bandpass. The Lyot filter, the third of three fixed elements, is a wide-field, temperature-compensated design (Title and Rosenberg, 1981) with a bandpass of 465 mÅ. The combination of the fixed filters has a transmission bandpass of 454 mÅ.

The light in this frequency band then passes through the two tunable Michelsons, which are the heart of the filter system. The two Michelsons have sinusoidal bandpasses with periods of 377 mÅ and 189 mÅ and are operated as analogs of birefringent elements. The bandpass can be positioned, or tuned, simply by rotation of half-wave plates. In this way it is possible to make spatially resolved images, called *filtergrams*, in a narrow (94 mÅ) bandpass anywhere in the vicinity of the Ni 6768 line.

3.2.1 MDI filtergrams

In normal operation, filtergrams are obtained at five tuning positions which are 75 mÅ apart, spanning the 377 mÅ tuning range. All of the standard observables are computed from these sets of five filtergrams. The filtergrams are labelled F_0 through F_4 according to their central spectral frequency: F_0 is nearly in the continuum, F_1 and F_4 are centered in the wings, and F_2 and F_3 are centered about the core of the Ni 6768 line at disk center. The Doppler velocity is given by

$$v_{LOS} = c\frac{\Delta\lambda}{\lambda}, \tag{3.1}$$

where v_{LOS} is the component of the velocity along the line of sight, c is the speed of light, λ is the wavelength of the absorption line, and $\Delta\lambda$ is the Doppler shift. In the case of MDI, the line shift is measured from the light intensity in the four filter bands F_1 through F_4:

$$\begin{aligned} x &= (F_1 + F_2) - (F_3 + F_4) \\ \alpha &= \begin{cases} x/(F_1 - F_3), & x < 0; \\ x/(F_4 - F_2), & x \geq 0 \end{cases} \end{aligned} \tag{3.2}$$

The MDI onboard processor then calculates the velocity from α using a lookup table that was contructed from simulations using parameterized solar line profiles and measured transmission characteristics.

3.2.2 Observing modes

In normal operation, MDI can make Dopplergrams with a one minute cadence without interruption. In practice, the amount of data that can be returned to Earth is limited by telemetry constraints. The basic observing mode is known as the Structure program. In this mode, the onboard processor computes vector-weighted averages of the 1024×1024 pixel Dopplergrams to reduce them to 192×192 pixels. One of these lower-resolution images is transmitted each minute.

The Dynamics program runs during a two- or three-month continuous timespan each year. During this time, MDI is able to send one full-disk (1024×1024) Dopplergram per minute, along with selected other observables. In addition to this continuous coverage, full-disk images are recovered for an eight hour period of each day. These short periods are known as campaigns. About once per month, there are opportunities for extended campaigns of three to five days. For this work, images were used from three Dynamics periods: June and July, 1996; April and May, 1997; and

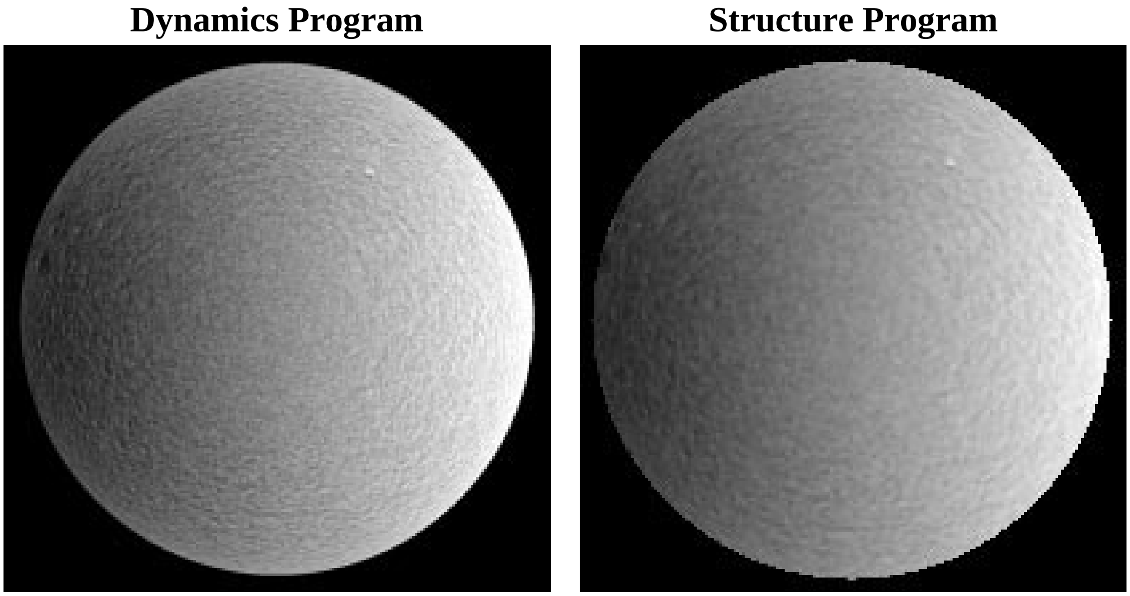

Figure 3.1: Typical Dopplergrams from MDI. The left-hand figure is a Dopplergram from the Dynamics program (full 1024 × 1024 pixels) and the right-hand figure is a Dopplergram from the Structure program (192 × 192 pixels). Dark pixels represent motion towards the observer, and light pixels away from the observer. Note the gradient across the image due to the solar rotation.

January, 1998.

During Dynamics programs or campaigns, it is also possible to record Dopplergrams in high-resolution mode. In this mode the spatial resolution is increased by a factor of 3.2 by taking magnified filtergrams of a restricted region of the solar disk.

Figure 3.1 shows a typical Dynamics and a typical Structure Dopplergram. Dark pixels represent velocites toward the observer, and bright pixels velocities away from the observer. The most prominent feature of the Dopplergrams is the gradient from east to west (left to right) across each image. This velocity is about 2000 m/s at the solar equator. Superimposed on this large-scale gradient are patterns which correspond to convection cells on various scales, and the solar five-minute oscillations. It is easy to see the difference in spatial resolution between the two Dopplergrams. Another, less obvious, difference is the fact that the Structure image has been cropped to remove a few pixels near the limb.

In practice, an image cannot be captured every minute. Some images are lost due to instrument calibration and spacecraft manoeuvres, telemetry gaps, and cosmic ray hits to the onboard storage memory. For this work, the effective duty cycle is about 95% on average.

The work included in this thesis will concentrate on data from the full-disk Dynamics and Structure programs. The images from the Dynamics program offer two principal advantages over the images from the Structure program: they have a higher spatial resolution (2 arcsecond pixels, which corresponds to a solar size scale of 0.12° at disk center); and they allow observation closer to the limb, since the Structure images are cropped before transmission to the ground. On the other hand, the Structure images (10 arcsecond pixels, or 0.6° scale at disk center) are made continuously, interrupted only for spacecraft maintenance maneuvers or other anomolous events. Furthermore, the decreased spatial resolution can be an advantage from a computational point of view. I will make a few more comments on the relative advantages and disadvantages of the two observing modes in the following chapter, which explains the details of the data analysis procedures.

Chapter 4

Data Analysis Methods

As outlined in section 2.3, the essence of time-distance helioseismology is the measurement of acoustic wave travel times. This chapter describes the various processing steps involved in measuring travel times from the MDI Dopplergrams described in chapter 3.

4.1 Remapping of Images

For the purposes of time-distance analysis (and indeed almost all helioseismic measurements) it is convenient to remap the images onto a new grid which is regular in some desired coordinate system. For reasons which will hopefully become clear, the remapping used in this work was the "cylindrical equal area" projection[1]. In this projection, the remapped image has points which are equally spaced in longitude and sine of latitude; all output pixels in a particular column have the same longitude, and all pixels in a row have the same latitude. The scale of the map is chosen such that at disk center it matches the scale of the input images. It follows that the image is oversampled at all other locations.

The remapping algorithm for each image takes into account the latitude and longitude of solar disk center, the effective solar position angle, and all other relevant

---

[1] The author is grateful to R.S. Bogart and the MDI software development team for the remapping software.

orbit parameters. The interpolation between input pixels uses a cubic convolution algorithm (Keys, 1981). In addition, the remappings used in this thesis were "tracked" in the sense that the remapped area was moved to follow regions as they rotated across the disk. The Sun, of course, does not rotate with a single angular velocity, so this tracking cannot exactly match the rotation at all latitudes.

The procedure for remapping, then, is to take a time series of images (typically several hours to several days) and produce a "data cube" where longitude is the first axis, sine of latitude the second axis, and time the third axis. This cube then forms the input to subsequent processing stages.

4.2 Filtering and Image Correction

Since the signal of interest in helioseismology is the acoustic wave (p-mode) signal, it is advantageous to remove other velocities which do not contribute to the desired output and therefore fall into the general category of "noise." Also, there are some instrumental effects which can be removed or corrected in order to enhance the final results.

4.2.1 Rotation gradient

It can be seen in figure 3.1 that a strong gradient is present in every Dopplergram. Most of this gradient does not vary with time, so it can be removed by subtracting a fixed pattern from each image. In almost all cases this was done during the remapping procedure. Typically, a background image was produced by computing the average of the input time series of Dopplergrams. This average image was then subtracted from each Dopplergram in the series before remapping. The signal in each pixel is thus forced to have a mean value near zero.

4.2.2 Supergranulation

Supergranules cause a problem for time-distance measurements because they are coherent velocity structures which cause nearby points on the solar surface to have

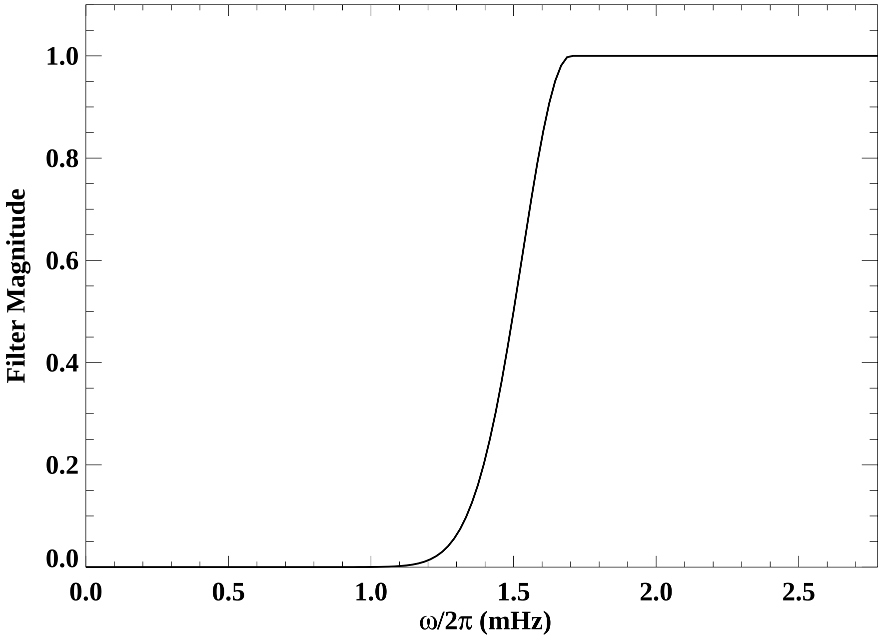

Figure 4.1: To remove supergranulation noise, a high-pass filter is applied to the data. The period at the cutoff shown here is roughly 10 minutes. Note that the horizontal axis does not extend all the way to the temporal Nyquist frequency ($\omega_N/2\pi = 8.33\,\mathrm{mHz}$). The filter shown is applied by multiplying with the power spectrum of the input data.

highly correlated velocities. Since time-distance measurements rely on the correlation of signals due to acoustic wave propagation from one point to another, it is necessary to remove as much of the supergranular signal as possible. Fortunately, supergranulation can be largely removed from the input data by use of a simple high-pass filter (see figure 4.1). Typically the filter used for this purpose was a gaussian roll-off with full transmission above 1.7 mHz (periods corresponding to about 10 minutes) and a full width at half maximum of 0.40 mHz.

4.2.3 Surface gravity waves

Although the supergranulation is easily separated from the acoustic signal in the temporal frequency domain, some other sources of noise are not. One such source

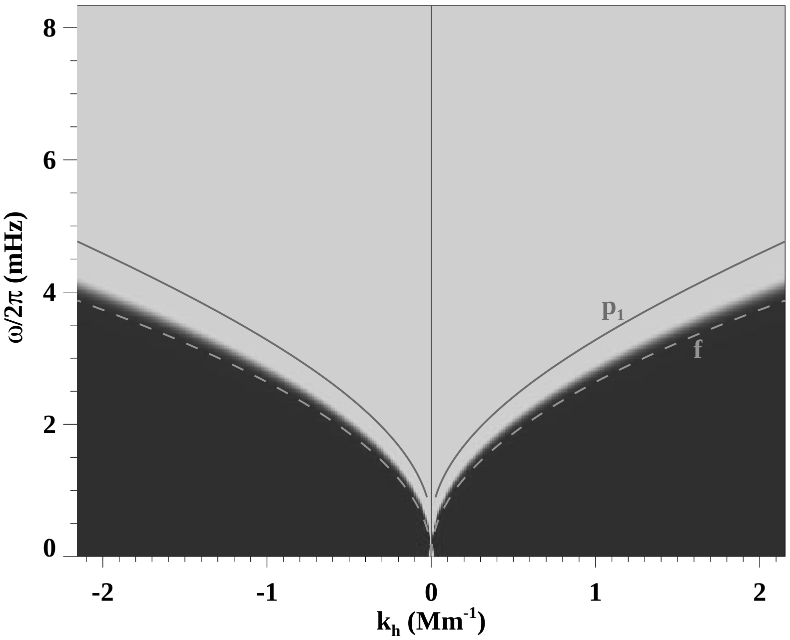

Figure 4.2: A depiction of the filter used to remove the oscillation due to the fundamental or f mode. The darkest greyscale indicates a filter magnitude of 0.0; the brightest, a magnitude of 1.0. The three-dimensional filter is multiplied by the power spectrum of the input data. The solid line shows the location of the p_1 ridge (see equation 4.2) in the k-ω diagram, and the dashed line the position of the f-mode (equation 4.1). The filter is constructed so that the f-mode is attenuated by a factor of 100.

of coherent velocity signals is the so-called "fundamental" mode (f-mode) of solar oscillation. The waves which make up this mode are surface gravity waves (analogous to waves on the surface of the ocean). Since these are propagating disturbances which do not follow acoustic ray paths, they pose a problem in the interpretation of measured travel times if not isolated from the acoustic signal.

The solution to this problem can be found in the k-ω diagram of figure 2.1. At each temporal frequency, the power of the f-mode appears at a larger value of horizontal spatial frequency k_h than for the p-modes. Thus it is possible to design a filter that removes all power beyond a certain value of k_h, where that value depends on ω. The locations of the f- and p_1-mode ridges in k-ω space were approximated with polynomial forms:

$$l_0 \approx \mathrm{R}_\odot k_{0h} = 100\nu^2 \tag{4.1}$$

$$l_1 \approx \mathrm{R}_\odot k_{1h} = \sum_{k=0}^{4} c_k \nu^k, \qquad c = \{17.4, -841, 95.6, -0.711, -0.41\} \tag{4.2}$$

where the cyclic frequency $\nu \equiv \omega/2\pi$ is measured in milliHertz. The filter was then constructed at each frequency as a low-pass filter in the spatial domain, with gaussian roll-off, full transmission halfway between k_{0h} and k_{1h}, and 1% transmission at $k_h = k_{0h}$ (see figure 4.2).

4.2.4 Phase velocity filtering

Since the travel time between two points is computed as the cross correlation of their respective velocity signals, it is beneficial to consider only those waves which travel between the two points. As described in section 2.3.2, the travel distance Δ between photospheric reflections is determined by the ratio of the temporal and spatial frequencies, ω/k_h. All waves with the same value of ω/k_h travel approximately the same distance, and all other waves travel different distances. If we are only interested in a finite range of distances, then, we can increase the signal-to-noise ratio of the measurement by filtering out waves which do not have the appropriate horizontal phase speed. In the k-ω diagram, the waves of interest have power which lies within a wedge-shaped region (see figure 4.3); in the three-dimensional power spectrum the surfaces are cones of constant ω/k_h. Again the filter is constructed to have a gaussian rolloff from each surface.

It should be noted that this filter should be used with caution when distances become large. It has been my experience that using a phase speed filter for large distances (large values of ω/k_h) can cause systematic errors and reduce the signal-to-noise ratio of the cross correlations. This may be due to projection effects on the power spectrum; since the remapping used is equally spaced in sine of latitude, the spatial wavelength scale in that direction is difficult to disentangle in an FFT.

In addition, for the work described here the measurement is always of a flow

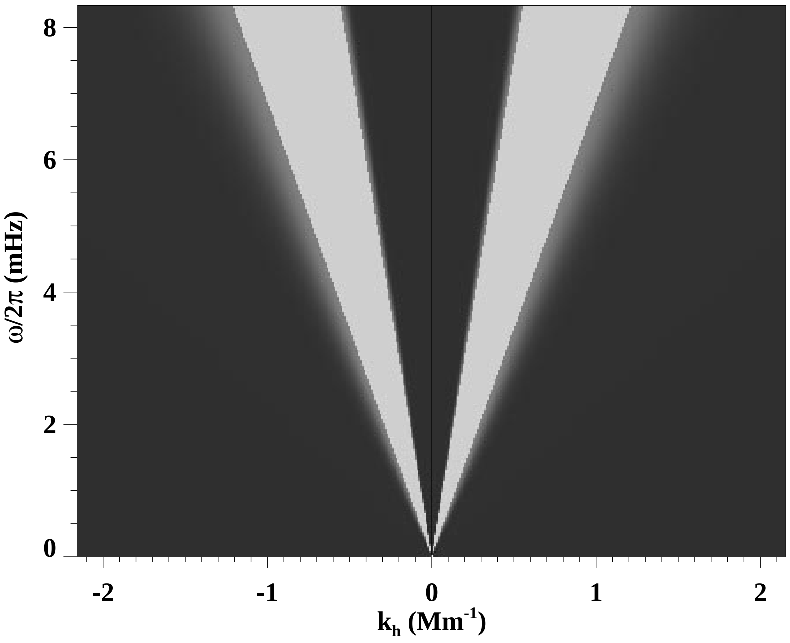

Figure 4.3: An example of a phase speed filter used for the anlysis. The horizontal phase speed is given by the ratio of the temporal frequency ω to the spatial frequency k_h. This figure shows a section of the power spectrum of the filter which is applied to the data; the Fourier transform of the filter is multiplied by the Fourier transform of the data. Here the lightest greyscale represents a filter value of 1, and the darkest a value of 0. The upper cutoff is the phase speed corresponding to a travel distance $\Delta = 10°$, and the lower corresponds to $\Delta = 3°$.

in a particular direction. In this case it is also beneficial to remove those waves whose horizontal phase velocities are in different directions. If I denote the horizontal wavenumber in the longitude coordinate as k_x, and in the latitude coordinate as k_y, then the waves of interest lie in a wedge-shaped region in the k_x-k_y plane centered on either the k_y axis (to measure the meridional flow: see figure 4.4) or the k_x direction (to measure the rotation). In three-dimensions the surfaces are planes of constant $\phi_k = \arctan(k_y/k_x)$.

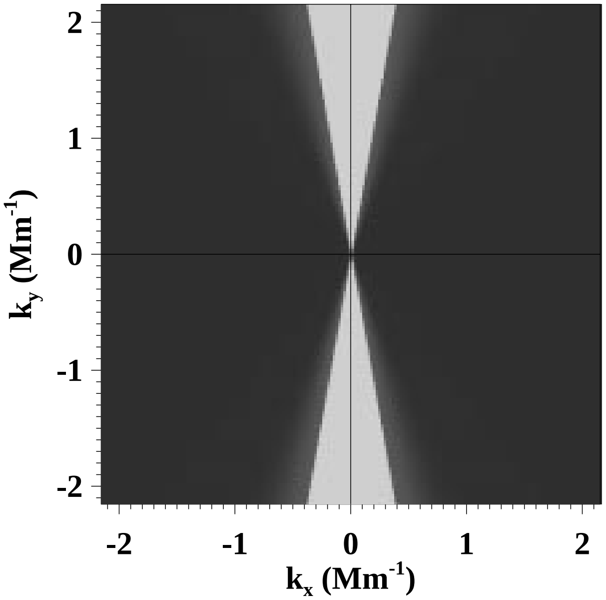

Figure 4.4: An example of a directional filter used for the anlysis (see text). The axis coordinates are the horizontal wavenumber in the longitude and latitude. The lightest greyscale represents a filter value of 1, and the darkest a value of 0.

4.2.5 Instrument modulation transfer function

The modulation transfer function (MTF) of the MDI instrument has the property that signals of high spatial frequency are attenuated relative to signals of lower spatial frequency (Scherrer et al., 1995). A typical measured power spectrum is shown in figure 4.5. For the purposes of time-distance helioseismology, the low power at high wavenumber means that waves with short travel distances are more difficult to observe and hence that the surface layers are less easily resolved. To correct for this effect, the input power spectrum is divided by the measured MTF. In practice, I have

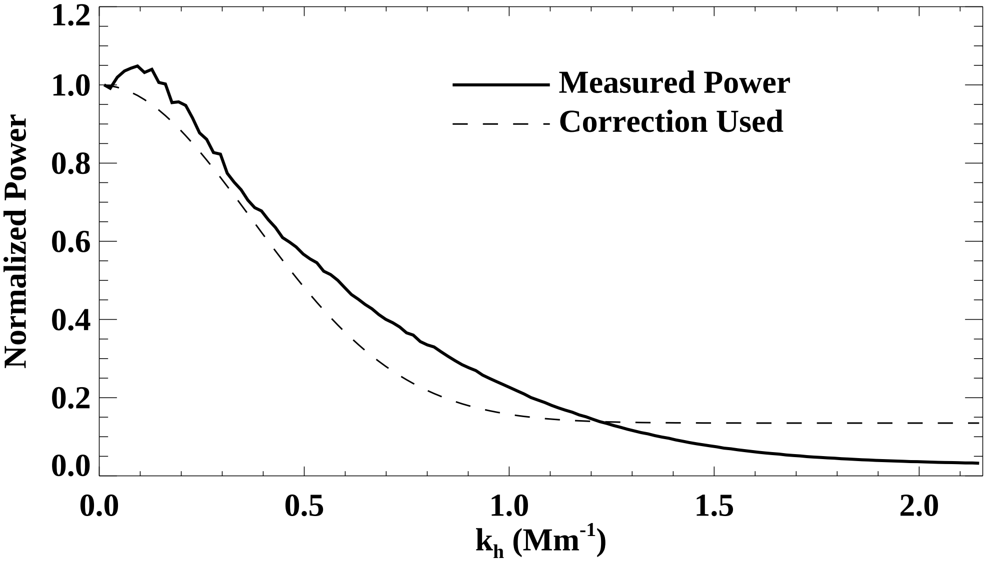

Figure 4.5: The MDI instrument attenuates the power at high spatial frequencies compared to the power at low spatial frequencies. The solid curve shows the power, averaged over temporal frequency and direction, from eight hours of Dynamics images. The power at low wavenumber has been normalized to 1. (Compare to Scherrer *et al.* (1995), figure 5.) The dashed curve is described by equation 4.3.

approximated the MTF by a smooth function:

$$M(k_h) = 0.865 \exp\left[-(\mathrm{R}_{\odot} k_h/364)^2\right] + 0.135, \tag{4.3}$$

This function describes the attenuation of the oscillation *power* as a function of wavenumber; to remove this effect, the Fourier transform of the input data is divided by the square root of M. The function M is constructed with a flat response at the highest values of k_h, since in this region the noise (non-oscillatory signal) in the solar velocity spectrum becomes large and it is not desirable to overamplify the power in this region.

In addition to the expected attenuation of high-k oscillation power, it has been observed that the power measured in MDI Dopplergrams varies with the direction of

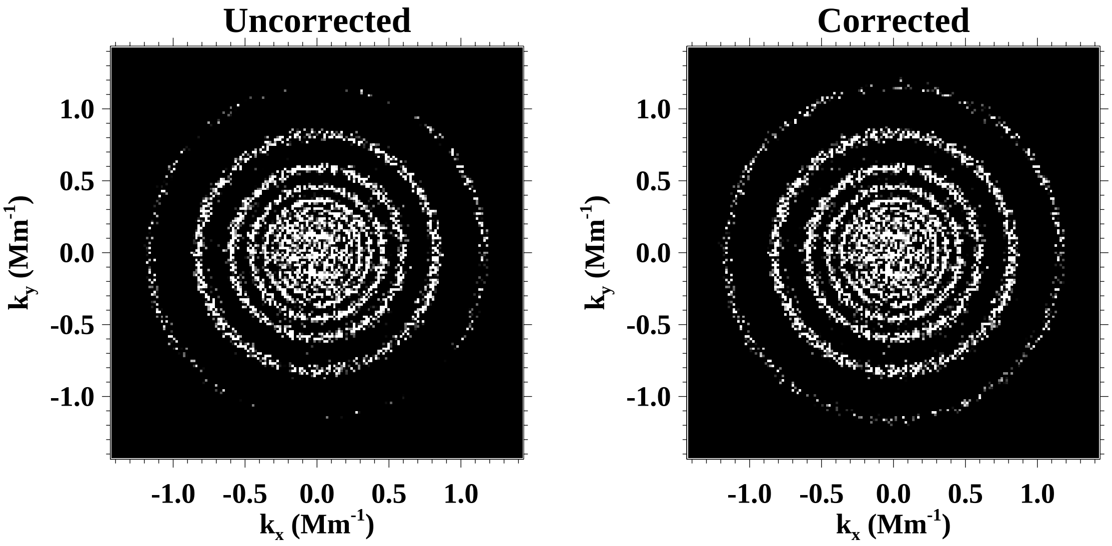

Figure 4.6: "Ring diagrams" for eight hours of Dynamics images from MDI. Each figure is a slice through the three-dimensional power spectrum of the series of images, at temporal cyclic frequency $\omega/2\pi = 4.16\,\mathrm{mHz}$. The horizontal axis is the horizontal wavenumber in the longitude direction and the vertical axis is the horizontal wavenumber in the latitude direction. The greyscale in each case is saturated to emphasize the variation of power with angle in the outermost ring, where the effect is most pronounced. The left figure is the uncorrected image; on the right, the power spectrum has been corrected with the function described in equation 4.4.

propagation; there is less apparent power in the north-south direction than in the east-west direction. This astigmatism can, like the MTF, be measured and then corrected for in the input power spectrum (see figure 4.6). The measurement is done at disk center and then applied to data from any position on the disk. Note that near the limbs there is some variation of acoustic power with direction due to foreshortening and the fact that the acoustic signal is mainly radial; this effect is not corrected for. The measured astigmatism is given by

$$\begin{aligned} A(k_h, \phi_k) &= [1 - Q(k_h)]\, P(\phi_k) + Q(k_h) \\ Q(k_h) &= \begin{cases} 0.56, & \mathrm{R}_\odot k_h > 1100; \\ \exp\left[-(\mathrm{R}_\odot k_h/1457)^2\right], & \mathrm{R}_\odot k_h \le 1100 \end{cases}, \\ P(\phi_k) &= \begin{cases} \cos^4(\phi_k - 0.153)\,, & k_h \neq 0; \\ 0, & k_h = 0 \end{cases}. \end{aligned} \tag{4.4}$$

where $\phi_k \equiv \arctan(k_y/k_x)$ is the direction east of north on the disk. Equation 4.4 describes the power as a function of direction and degree; to remove the astigmatism, the Fourier transform of the input data is divided by the square root of A. Note that for small values of the horizontal wavenumber k_h the astigmatism is quite small; in particular, the correction is not very important for images from the Structure program, which contain information only for small and moderate wavenumbers.

4.3 Computing Cross Correlations

Once the Fourier transform of the three-dimensional data cube has been filtered and corrected as described in section 4.2, the inverse Fourier transform is computed in the two spatial dimensions. This leaves an array of temporal Fourier tranforms, one for each input pixel. These are used to compute temporal cross correlations between pairs of points, taking advantage of the special relationship between cross correlation and multiplication in the Fourier domain (see equation 2.7). This relationship greatly simplifies the computation of cross correlations. It remains to discuss how pairs of pixels are chosen.

Since for this work it is desired to measure the flow in a particular direction (either east-west or north-south), it is necessary to measure travel times for waves which propagate parallel to that direction. For example, to measure a meridional flow, pairs of points are chosen which have the same longitude. For any particular latitude, there are a number of pairs of pixels which have the same longitude and which are the same distance apart. These cross correlations are computed and then averaged together to improve the signal-to-noise ratio in the final result. Furthermore, pairs with similar — but not exactly the same — latitudes and separations are also added to the average, since they are expected to have similar travel times. Finally, cross correlations are computed for pairs of points which are only approximately on the same line of longitude.

The analysis for measuring solar rotation proceeds similarly, except that target pairs of points have the same latitude instead of the same longitude.

4.3.1 Observing modes and computational burden

As described in section 3.2.2, two kinds of Dopplergrams have been used for the measurements in this thesis. Let me make a few comments on the two cases.

First, the increased spatial resolution of the Dynamics images is obviously an advantage when it comes to measuring cross correlations for short distances. This is not only because the centers of the pixels are closer together, therefore permitting measurements for short distances, but because the larger number of pixels leads to an increase in the number of pairs and an increase in the number of cross correlations which can be computed. This is equivalent to an increase in the number of measurements, and leads to an improvement in the signal-to-noise ratio.

For longer distances, however, it is not clear that a great gain is made by using higher-resolution images. Waves which travel longer distances have a larger spatial wavelength and therefore a larger coherent wavefront. Taking more samples of this large wavefront should not improve the noise characteristics of the measurement. Therefore I expect that for large distances the resolution of the Structure images should be adequate. I will show some evidence for this claim in section 4.5.

This is also fortunate from a computational point of view. Since the Structure images have many fewer pixels (by a factor of 25), the number of cross correlations to be computed is greatly decreased. This means that one month's worth of Structure images can be analyzed in a few days, up to a distance of 45°, whereas the same amount of time is required to compute cross correlations from about 6 days of Dynamics images, for distances up to only 6°.

On the other hand, the Dynamics images have a great advantage over the Structure images at high latitudes. This is partly due to the increased spatial resolution, which

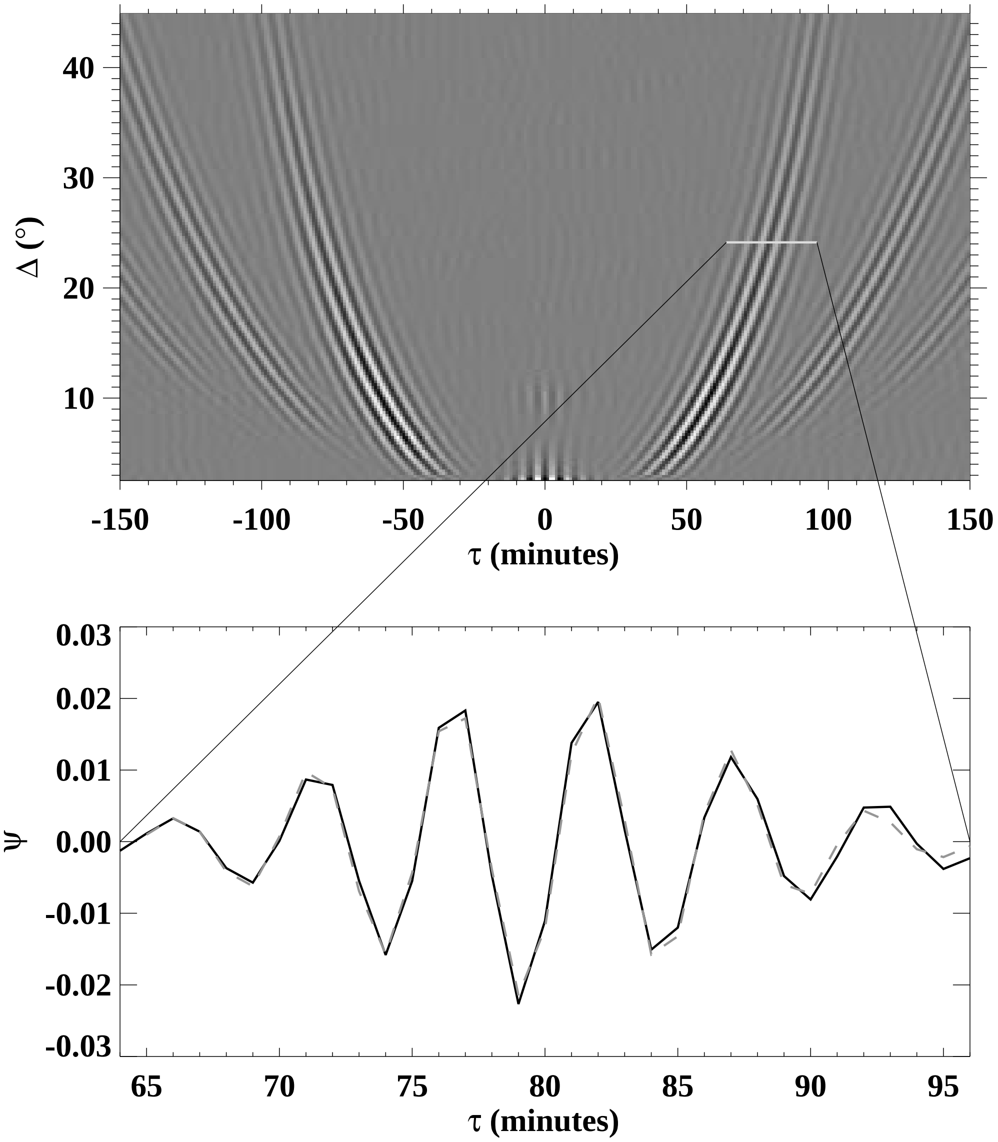

Figure 4.7: This "time-distance diagram" shows some cross correlations typical of those used in this work. In the upper plot, the greyscale denotes the cross correlation amplitude as a function of the time lag τ and the distance Δ. The lower plot displays the cross correlation for a particular distance ($\Delta = 24.1°$), near the maximum. The dashed line in the lower plot shows the function $G(\tau)$ (equation 4.5), where the free paramaters have been determined by a non-linear least squares technique.

allows more pixels in regions near the limb. In addition, the Structure images are cropped by the on-board processor to allow them to fit into the telemetry stream.

4.3.2 Averaging of cross correlations

In order to improve the signal-to-noise characteristics of the measurements, it is often necessary to average the cross correlations together over certain ranges in distance, latitude, and time. The averaging in distance is fairly minimal, generally over a range of 0.25 degrees. It is not possible to average the cross correlations very much in this dimension because the position of the peak depends strongly on distance (figure 4.7) and excessive averaging tends to smear the result.

Averaging in latitude is more flexible, since the dependence of the cross correlation on latitude is fairly weak. Generally, the results presented here have been averaged over latitude bands of five degrees. Some care is taken to ensure that the contribution of each cross correlation to the average is properly weighted. The weight is proportional to the total number of pairs of pixels used in each component cross correlation. This is especially important at high latitudes, where the number of available pixels drops off sharply as the region of interest approaches the limb.

Finally, since the cross correlations are generally computed on relatively short time series of images (a few hours to a few days), it is sometimes desirable to average together many such series. For example, to examine the axisymmetric component of the meridional circulation, it is obviously important to observe the Sun for at least one rotation period. The results presented here have been averaged over different time spans, depending on the object of the measurement; the results for the flows very deep in the convection zone come from averages over more than 700 days. Many measurements are averaged over one or a few solar rotations. In any case, some care is again taken to compute a properly weighted average. In the case where the observations do not each span the same length of time, the contribution of each cross correlation to the sum is proportional to the length of the observation.

4.4 Travel Times From Cross Correlations

Section 2.3.1 illustrates that the peak in the cross correlation function can be interpreted as the wave travel time between points on the solar surface. The second peak at negative time lag τ is interpreted as the travel time in the opposite direction. Each travel time is located by fitting a function of the form (compare to equation 2.21)

$$G(\tau) = A \exp\left(-\frac{\delta\omega^2}{4}(\tau - \tau_g)^2\right) \cos(\omega_0(\tau - \tau_p)) \tag{4.5}$$

to the cross correlation near its peak. Here, A is the cross correlation amplitude, ω_0 is the central frequency of the traveling wave packet, and $\delta\omega$ is the frequency bandwidth. The two parameters τ_g and τ_p are the group and phase travel times, respectively. Figure 4.7 shows the function $G(\tau)$ and a typical measured cross correlation. Because the phase time is more accurately determined in the fitting procedure, I have used the phase time in all cases and will drop the subscript p.

The end result of the fitting is a collection of travel times τ^+ in the "positive" direction (southward or eastward) and τ^- in the "negative" direction (northward or westward). From these, the time differences are computed:

$$\delta\tau(\lambda, \Delta) = \tau^+ - \tau^-. \tag{4.6}$$

These can then be interpreted as a measure of the subsurface velocity.

4.5 Measurement Uncertainties

The fitting procedure described in section 4.4 does not, unfortunately, give a realistic estimate of the uncertainty in the fitted parameters and hence in the measured travel time τ.

In order to estimate the uncertainty in the travel times, I examine the scatter of the measurements about their mean. Fortunately, there are a large number of measurements and it is possible to get meaningful statistics from their distribution. However, some care must be taken in the process and it is worth describing in some detail.

First, it is obviously important to weed out any outliers from the measurements. These are principally points where the fitting did not converge because the function 4.5 is a poor fit to the cross correlation. The most reliable way to remove these points is by visual inspection of the fits and the cross correlations. Fortunately, this is generally only a problem for the shortest distances. The problem is accentuated at high latitudes, but there are still relatively few fits (a few dozen out of a few thousand, say) which need to be inspected by eye.

Next, I compute the travel time difference for each pair of travel time measurements. These can be used to compute the mean travel time difference, and the scatter about that mean, as a function of latitude and distance. This is accomplished by selecting small subsets of points, with similar distances and latitudes, and computing the statistical moments for that subset of measurements. Then each of the measurements in the subset is assigned an uncertainty which is equal to the standard deviation of the subset. Finally, the uncertainties are smoothed in both latitude and distance to remove any discontinuities in the distribution of errors.

Figures 4.8 and 4.9 show the distribution of measurement errors as a function of latitude and distance. These measurements were made from the first two years of Structure images and make use of almost the entire disk for averaging of cross correlations. The two measurement directions give somewhat different distributions of errors because of the geometry of the remapped regions.

Earlier I stated that the Structure program Dopplergrams, despite their lower spatial resolution, could be used to measure travel times for large distances with no degradation of the signal-to-noise ratio. Figure 4.10 shows a comparison of the Dynamics and Structure measurements for time series of equal length which were nearly contemporaneous and covered comparable areas of the solar image. Clearly the Dynamics images have a significant advantage for measuring time differences at short distances; in fact, it is quite difficult to make measurements from Structure images for distances less than three degrees. However, the Structure images are quite adequate for distances larger than about ten degrees.

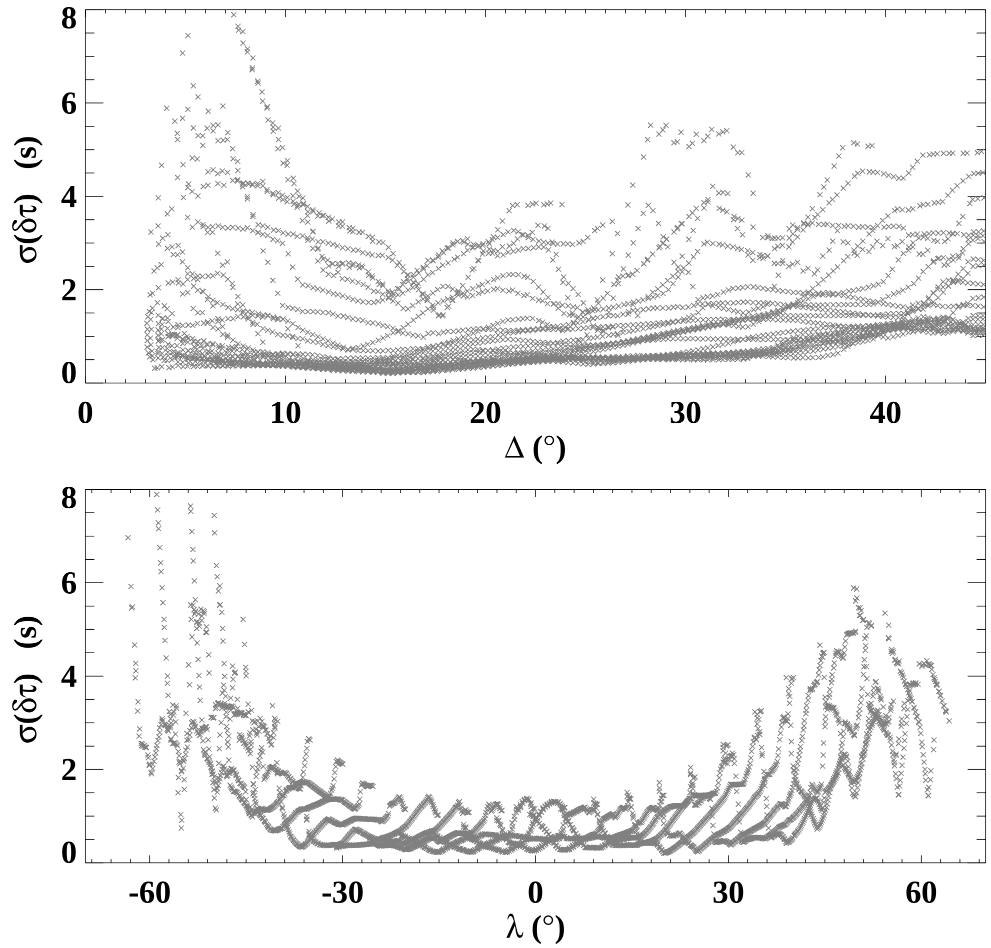

Figure 4.8: Measurement errors for the south-north time differences are shown as a function of distance and latitude. The measurements are from 792 days of Structure images. Each × represents a single measurement with unique coordinates (Δ, λ).

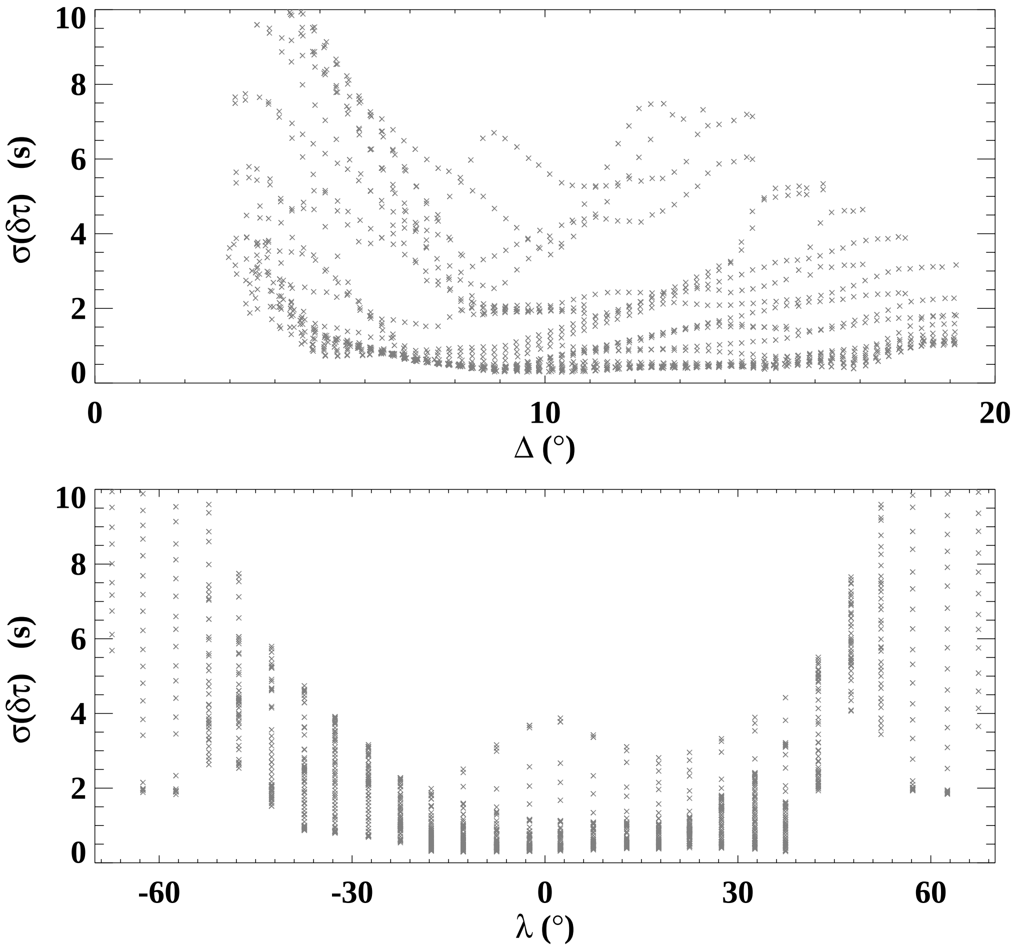

Figure 4.9: Measurement errors for the west-east time differences are plotted as a function of distance and latitude. The measurements are from 792 days of Structure images. Each × represents a single measurement with unique coordinates (Δ, λ).

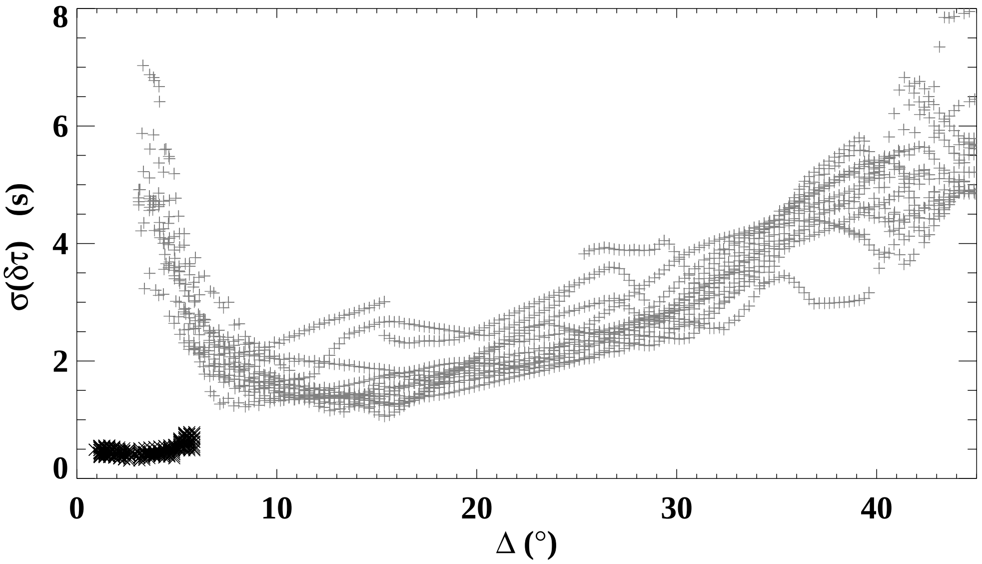

Figure 4.10: The measurement errors σ are shown as a function of distance. The errors σ are for a selection of south-north time differences, measured at locations within 30° of the equator. The points in the lower left corner, marked with a black ×, were made from one month of Dynamics images from 1998. The points marked with a gray + were made from one month of nearly contemporaneous Structure images. The spatial averaging was also comparable in the two datasets.

4.6 Typical Measurements

The set of time difference measurements $\delta\tau(\lambda, \Delta)$ contains information about the solar velocity field $\mathbf{u}(\lambda, r)$. One interesting way to display the measurements is to simply average them over different distance ranges and display the results as a function of latitude. Figure 4.11 shows a typical set of measurements of south-north travel time differences. This plot includes a particular range of distances and the results are averaged in latitude bins of five degrees. When the distances Δ are not too large compared to the latitude bins, a plot like figure 4.11 can be said to describe an average of the meridional flow over a certain depth range near the surface.

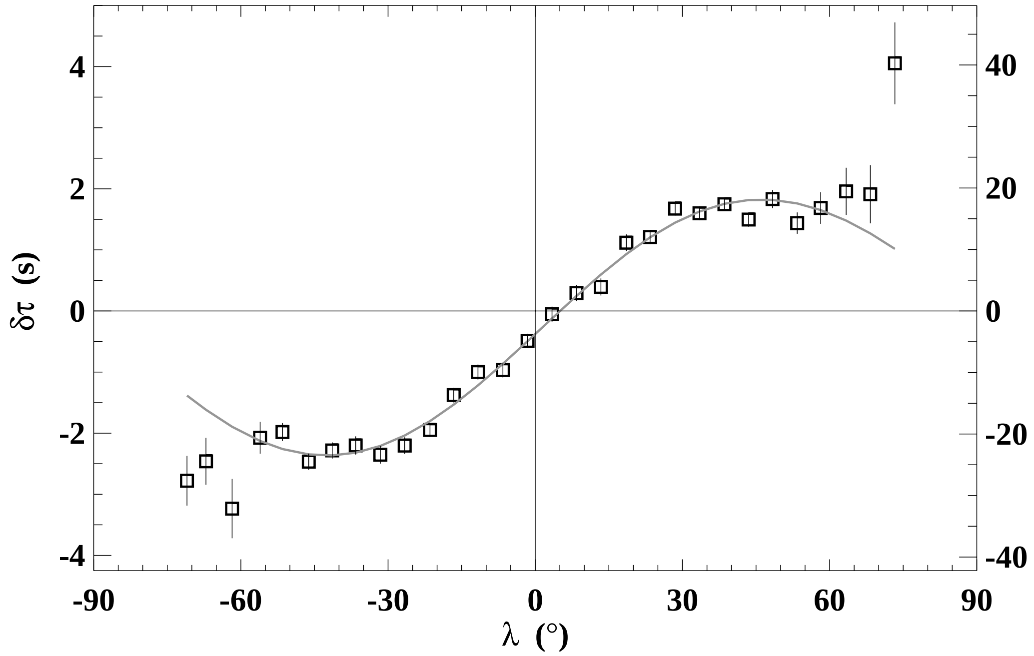

Figure 4.11: A typical set of measurements, from the Dynamics period of 1996. The time difference $\delta\tau$ is plotted as a function of latitude λ; the measurements have been averaged in distance for ($1° \leq \Delta \leq 6°$). The sense of the time difference is south – north, so that a positive time difference indicates a northward flow. The solid curve is a least-squares fit of the form 4.7. The right-hand axis indicates the corresponding meridional velocity in m/s. This velocity was calculated by assuming that the velocity does not vary with depth over the range in question; a ray with $\Delta = 6°$ penetrates to $r = 0.963\,\mathrm{R}_\odot$.

Following some past observers, I sometimes will use a smooth function to approximate the latitude dependence of the meridional circulation:

$$\delta\tau = \sum_{k=1}^{N} a_k \sin(k[\pi/2 - \lambda]). \tag{4.7}$$

Generally the fit is made with $N = 4$ and with coefficient a_3 set to zero.

Figure 4.12 is a similar plot for the east-west time differences, and thus represents a measurement of the solar near-surface rotation. In the case of the rotation,

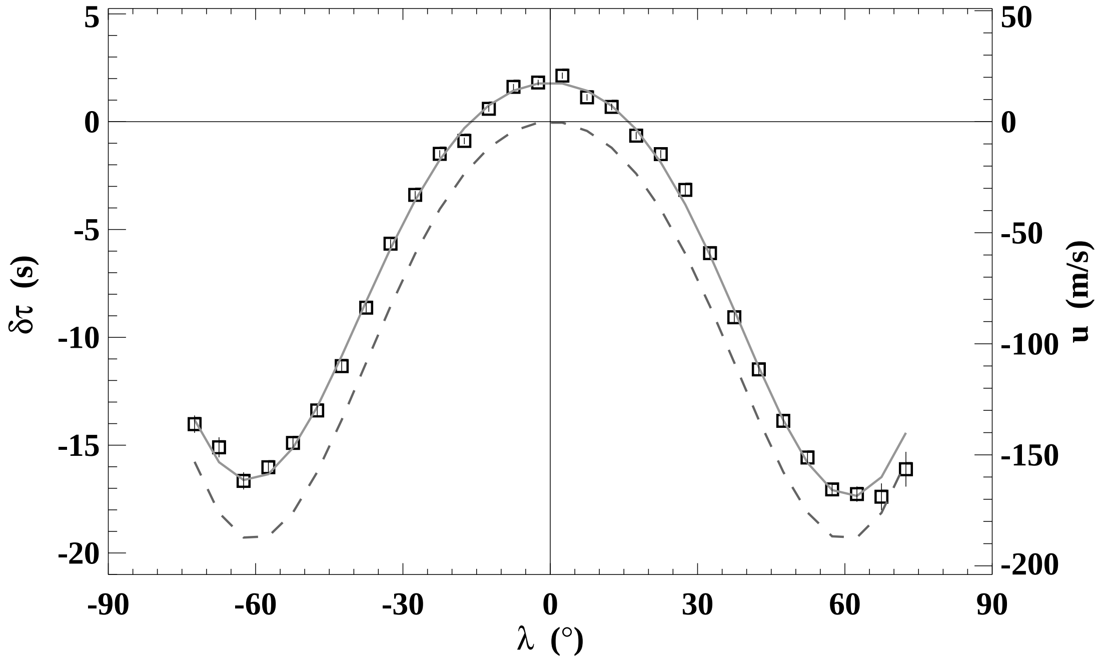

Figure 4.12: A typical set of measurements, from the Dynamics period of 1996 (see also figure 4.11). For these measurements, the sense of the time difference is east – west, so that a positive time difference indicates a prograde flow. The solid curve is a least-squares fit of the form 4.8. The right-hand axis indicates the corresponding zonal velocity in m/s, calculated as described in figure 4.11. The dashed curve shows the rotation velocity at the solar surface as measured by Snodgrass (1984), plotted with respect to the right-hand axis. The tracking velocity at each latitude has been subtracted, to compare with the measurements.

as described in section 1.2.1, both the surface and interior values are already quite well known, so we are able to check our results against those from other methods. Figure 4.12 shows a measured surface rotation rate for comparison with the time-distance measurement. Clearly the time-distance measurements give a larger velocity than the surface measurements; this is in agreement with other helioseismic measurements which indicate an increasing angular velocity in the layers just below the solar surface. I will have more to say about this when I discuss inversion results in section 6.1.2.

The solid curve in figure 4.12 is a least squares fit of the following expansion:

$$\delta\tau = \sum_{k=1}^{N} a_k \sin(\pi/2 - \lambda)\cos^k(\pi/2 - \lambda) \tag{4.8}$$

Comparing this to equation 1.1, we see that the two forms are equivalent if $N = 4$ and $a_1 = a_3 = 0$.

4.7 Instrumental and Systematic Errors

4.7.1 Roll angle uncertainty

One of the most obvious features of the meridional flow measurement in figure 4.11 is the southward flow across the equator (about 5 m/s for that particular measurement) which suggests that the meridional circulation is not antisymmetric about the equator. It has been pointed out that such a velocity pattern could result from an error in the orientation of the MDI camera of a few arcminutes (Giles et al., 1997). This would mean that the nominal "north" direction would not be truly orthogonal to the solar rotation velocity; a small component of this velocity (which is roughly 2000 m/s at the equator) could leak into the meridional circulation measurement.

Although the MDI instrument had its camera aligned very precisely with the SOHO spacecraft reference direction prior to launch, it is possible that some shift occured during the launch. Furthermore, thermal stresses may cause the spacecraft itself to deform. One way to evaluate this misalignment would be to assume that the cross-equator meridional circulation was entirely due to such an effect. However, this assumption may not be entirely justified. Another way to evaluate the orienation of the MDI camera is to compare with observations from ground-based instruments where the absolute orientation can be carefully measured. Evans (1999) has performed a comparison between images from MDI and Dopplergrams from the Mount Wilson Solar Observatory and finds that the MDI images are rolled by 0.3° with respect to the Mount Wilson images. The sense of this roll is the same as that required to explain a southward flow across the equator; however, the magnitude is large enough to produce a flow of 10 m/s, which is larger than the average value observed. Evans estimates that the random error in the determination of the roll angle is about 0.05°.

Another possibility along this same line is that the coordinates used by SOHO to maintain the correct attitude do not accurately describe the direction of the solar rotation axis. Interestingly, this error would cause the cross-equator component of the meridional circulation to vary with time as SOHO moves in its orbit. This possibility offers an intriguing way to measure the direction of the Sun's rotation axis, as outlined in appendix A.

It is possible, of course, that the equator-crossing flow is not an error at all. There is no requirement from first principles that the meridional circulation has to be zero at the equator. Other measurements of the meridional circulation using different techniques have also found similar effects (Schou and Bogart, 1998; Basu et al., 1998; Meunier, 1999); but all of these results were obtained using MDI images and so are subject to the same intrumental errors. An independent observation of an equator-crossing flow has been noted by Komm *et al.* (1993b), using magnetic field observations from the Vacuum Telescope at the National Solar Observatory on Kitt Peak. These researchers noted that there was a northward flow across the equator which averaged 10 m/s during the period from 1978 to 1990, but attributed this to telescope misalignment. It is probably fair to say that the question of the equator-crossing meridional circulation is still unresolved. Further information can be gathered by looking at the depth dependence of the flow and comparing to the profile which would be expected if the flow was due to a roll angle. I will comment on this again in later sections.

4.7.2 Plate scale uncertainty

Another effect which is common to a large number of measurements from MDI has been labelled the plate scale error. The observational effect is that the solar rotation rate appears to be larger on the receding (westward) side of the disk than it does on the approaching (eastward) side. The solar plasma thus appears to be moving faster and faster as it traverses the disk. (see figure 4.13). This is seen in measurements

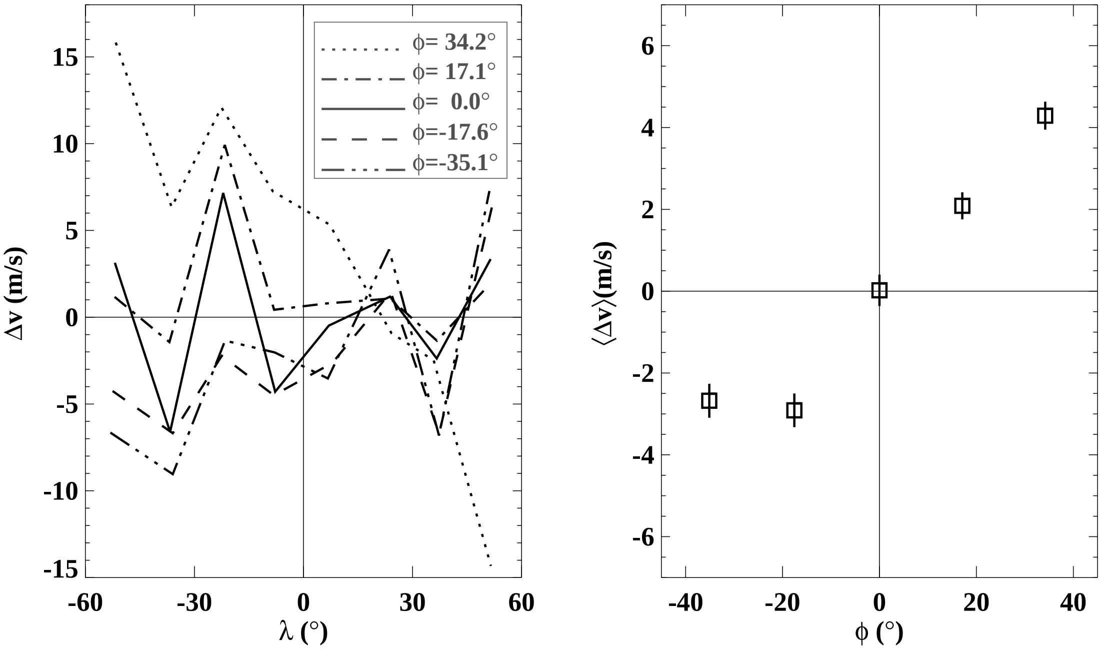

Figure 4.13: The left-hand figure shows the zonal velocity as a function of latitude for different positions on the disk. The measurements were made for one complete Carrington rotation during the Dynamics run of 1998. The different curves are for different longitudes ϕ, measured westward from the center of the disk. A smooth fit of the form of equation 4.8 has been removed from each of the five curves, and the residuals are plotted. The right-hand plot shows the latitude-averaged residuals as a function of ϕ, with error bars to give an idea of the significance of the effect.

from time-distance helioseismology, ring diagram analysis, and correlation tracking, although the magnitude of the effect seems to vary from method to method. The fact that this is seen even when the measurements are averaged over several months indicates that it cannot be a real solar phenomenon.

The cause of this effect is probably the fact that image focus is not uniform over the MDI camera. This means that the plate scale, defined as the heliocentric distance between pixels, is also not uniform. In remapping the MDI images as described in section 4.1, the plate scale is assumed to have some uniform value; if the plate scale is in fact smaller on the west side of the image than it is on the east side, then a feature

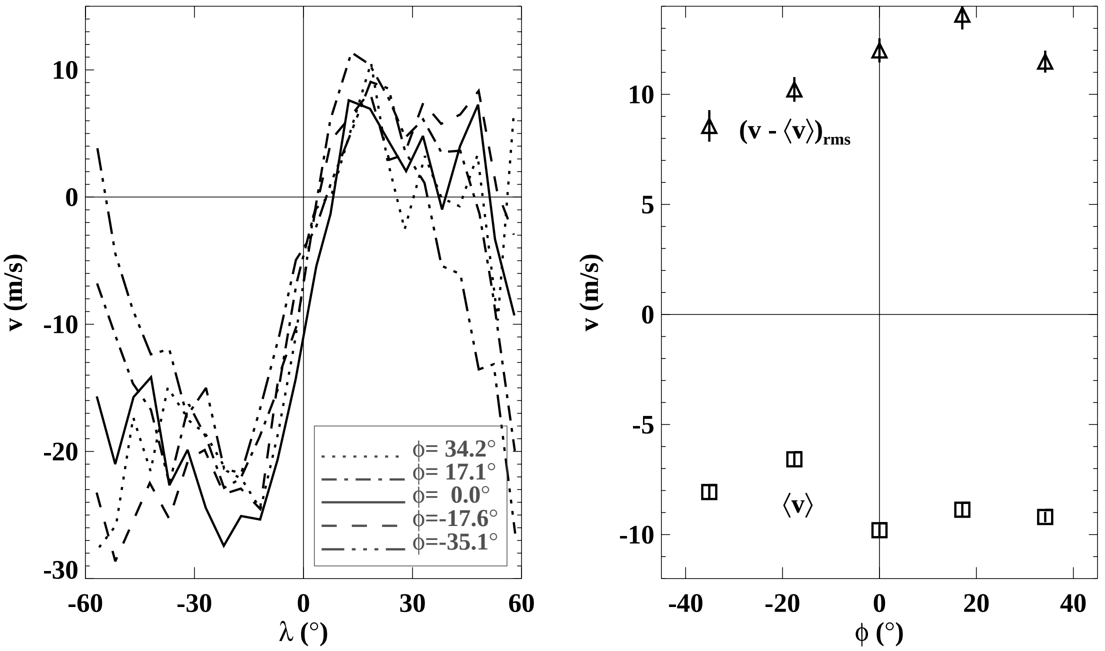

Figure 4.14: The left-hand figure shows the meridional velocity as a function of latitude for five different positions on the disk. The measurements were made for one rotation during the Dynamics run of 1998. The different curves are for different longitudes ϕ, measured westward from the center of the disk. The right-hand plot shows the latitude-averaged mean flow (squares), and the deviation from the mean (triangles), As a function of longitude. Although the mean velocity does not show a strong systematic dependence on longitude, the shape of the profiles clearly varies systematically according to the position of the observed region on the disk.

on the solar surface will appear to accelerate as it rotates across the solar disk.

It should also be noted from figure 4.13 that the effect is clearly more pronounced at some latitudes than at others. If it is indeed due to a non-uniform focus of the image, then it also probably changes when the instrument focus is changed.

The meridional flow measurements also show a similar effect. Figure 4.14 shows the measured time differences as a function of longitude on the disk. While the mean flow does not show a strong systematic dependence on position, the poleward amplitude does increase from east to west. Note that although the spread between the curves is largest at high latitude, the pattern does not appear to be systematic; this scatter is probably due to the large uncertainties near the limb.

In order to account for the uncertainty in the plate scale, in this work some care has been taken to ensure that all of the measurements were made on the same location on the disk. In most cases, the measurements were made during a time period where the remapped region crossed the central meridian. This reduces the chance of relative errors between measurements, but the absolute plate scale is still somewhat uncertain. Thus any comparisons between these measurements and those from different instruments may suffer from a small absolute offset.

Chapter 5

Solution of the Inverse Problem

Once the travel time differences have been computed as a function of travel distance Δ and latitude λ, it remains to compute the subsurface velocity $u(r, \lambda)$. This process is rather more complicated than it might appear at first glance, and its solution requires some knowledge of inverse problems. The terminology and formalism of this subject are briefly described here.

5.1 The Integral Equation

Equation 2.44 relates the horizontal velocity u of the solar plasma to a particular measured time difference $\delta\tau$, under the assumptions of the ray approximation. The object, then, is to determine the function $u(r, \lambda)$ which best fits the measurements. A naive approach would be to discretize the problem and then find the "best fit" model u in a least-squares sense. In the discussion which follows, I will describe this procedure in slightly more detail, explain why it must fail, and then describe the use of regularization to obtain a stable and reasonable solution.

5.2 The Regularized Least Squares Method

5.2.1 Discretization of the problem

In order to convert the equation 2.44 into a matrix equation which can be solved by a computer, it is simply necessary to model the region of wave propagation with a suitable grid. One approach is to create a grid which is equally spaced in radius and latitude. Assume that there are M_1 latitude gridpoints and M_2 radial gridpoints, where $M = M_1 M_2$. These M model velocities can be thought of as forming a vector u. For a particular measurement $\delta\tau_i$, where the index i denotes the coordinates (λ, Δ) which determine the ray path, the relationship between the model and the data can be expressed as

$$\delta\tau_i = \sum_{j=1}^{M} K_{ij} u_j. \tag{5.1}$$

The *sensitivity kernel* K_{ij} has elements which are given by

$$K_{ij} = 2 \int_i \frac{v_{gh}}{v_{gr} c^2} dr_j, \tag{5.2}$$

where the integral is along the particular element of the ray path determined by i which lies within grid cell j. In other words, the velocity u is assumed to be constant within each cell of the grid.

The choice of the grid spacing is intimately related to the question of the resolution of the solution, which is discussed in section 5.2.4. However, the radial coordinate deserves special mention. The simplest choice is to make a grid which is equally spaced in radius as well as latitude. However, analysis of the inversion results has shown that this offers a somewhat misleading view of the resolution of the solution deep in the convection zone. A better choice is to create a grid which has equal spacing in *acoustic radius*, defined[1] as

$$r_\tau \equiv \int_0^r \frac{dr'}{c}. \tag{5.3}$$

---

[1] Here I use the symbol r_τ rather than the standard τ, so as not to become confused with travel time.

In this case the grid points are equally spaced in travel time, assuming radially propagating waves and ignoring dispersion.

A typical sensitivity kernel is shown in figure 5.1. Since each measurement $\delta\tau_i$ actually is made from the average of a large number of cross correlations, the kernel is not actually constructed for a single ray path but for the weighted mean of all of the ray paths which have contributed to the average. The weight for each ray path is proportional to the number of pairs of pixels used which had exactly the same distance, latitude, and direction (see also section 4.3.2).

Once the problem has been discretized, the equation 5.1 can be recast in matrix form,

$$Ku = z, \tag{5.4}$$

where the N elements of the vector z are $z_i = \delta\tau_i$, the vector u has the M model velocities for components, and each row of the $N \times M$ matrix K is a sensitivity kernel with components given by equation 5.2. If we define two new quantities A and b,

$$b_i = z_i/\sigma_i, \qquad i = (1, \ldots, N) \tag{5.5}$$

$$A_{ij} = K_{ij}/\sigma_i, \qquad j = (1, \ldots, M) \tag{5.6}$$

then we want to find the solution $\hat{u}$ which minimizes

$$\chi^2 \equiv |Au - b|^2 \tag{5.7}$$

with respect to u. This is equivalent to solving the set of linear equations (see for example Press *et al.* (1992))

$$A^T Au = A^T b. \tag{5.8}$$

In practice, however, this will not give us a useful answer for $\hat{u}$, if it gives an answer at all. The problem here is that since the operator K is an integral operator it will act to smooth the response of the data to the model. This "smoothed out" information cannot be recovered by solving the set of linear equations in equation 5.8. In addition, since the operator K is a smoothing operator, the inverse operator (if it exists), when operating on the noisy measurements, will cause the solution to be unstable. Finally,

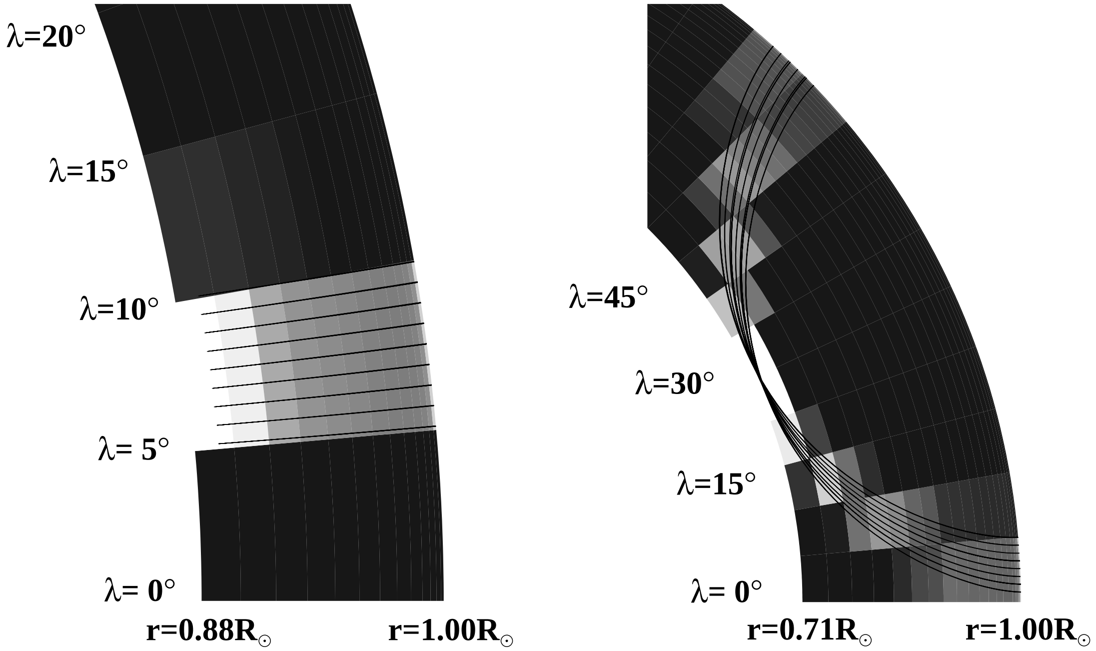

Figure 5.1: The left-hand figure shows the sensitivity kernel for the zonal velocity, for the measurement with $\lambda = 7.5^\circ$, $\Delta = 18.1^\circ$. The right-hand figure shows the sensitivity to the meridional velocity for the measurement with $\lambda = 24.4^\circ$, $\Delta = 44.1^\circ$. The greyscale shows the sensitivity to horizontal flows, with black areas being those with no sensitivity. The black curves depict ray paths for the individual measurements which were averaged together to get the single kernel shown here; that is, each black curve represents a different pair of MDI pixels. There are 52 rays in the left-hand figure, and 39 on the right, although many of the curves overlap. In the left-hand figure, note that the rays do not propagate at constant latitude.

the problem may be *underdetermined* — we may attempt to solve for more model parameters than there are measurements. This is, strictly speaking, mathematically impossible, but can be accomplished if some *a priori* knowledge can be used to select the proper solution from the set of possible solutions given by the measurements.

5.2.2 Regularization

A common and very useful approach to this problem is to add an additional constraint which causes the chosen solution to be "smooth" in some way. For example, rather than minimize χ^2 alone, we can try to find the solution $\hat{u}$ which minimizes the quantity

$$|Au - b|^2 + \gamma u^T H u, \tag{5.9}$$

where the second term represents some sort of smoothing operation. As examples, four forms have been used for the matrix H in this work:

$$\begin{aligned}
u^T H_0 u &\Longrightarrow \int\int |u|^2 r\, dr\, d\theta && (5.10)\\
u^T H_1 u &\Longrightarrow \int\int |\nabla u|^2 r\, dr\, d\theta && (5.11)\\
u^T H_{u/r} u &\Longrightarrow \int\int \left|\nabla \frac{u}{r}\right|^2 r\, dr\, d\theta && (5.12)\\
u^T H_\Omega u &\Longrightarrow \int\int \left|\nabla \frac{u}{r\cos\lambda}\right|^2 r\, dr\, d\theta && (5.13)
\end{aligned}$$

where the matrix operations on the left are discrete approximations of the integrals on the right. The chosen matrix H is called the *regularization operator*, and adding it to the problem constrains the solution to be smooth in some sense.

Minimizing the quantity 5.9 is equivalent to solving the set of linear equations

$$(A^T A + \gamma H)u = A^T b. \tag{5.14}$$

The solution $u = \hat{u}$ obviously depends not only on the data z, the errors σ, and the model K, but also on the regularization scheme chosen (choice of H). The relative influence of the regularization is controlled by the free parameter γ in equation 5.14, which is called the *regularization trade-off parameter*.

5.2.3 Trade-off parameter

When γ is large, the influence of H is great compared to the influence of the model A, and the solution obtained, although very smooth, probably will not be a good fit to the data. On the other hand, when γ is small, the influence of the regularization term is relatively small. The solutions in this case can provide an arbitrarily good fit to the (noisy) data, but will have unreasonably large magnitudes and derivatives.

In general, model solutions $\hat{u}$ are usually computed for a range of different values of γ, and then the "best" model in some sense is chosen from the set of solutions. At the two extremes, it is easy to rule out the solutions obtained, but the determination of the "best" solution is often a matter of art.

One way to look at the effect of the trade-off parameter in a somewhat quantitative way is to plot the magnitudes of the two terms in the quantity 5.9. Such a diagram is shown in figure 6.1 and is known as an *L-curve*. The trade-off parameter is increasing in magnitude from right to left, so the smoothness of the solution is increasing. The bend in the L-curve is an optimal solution for this particular choice of regularization; it is the smoothest solution possible with a "small" value of χ^2. If the errors σ in the measurements can be trusted, then we can hope that the bend in the L-curve will be located near a solution with $\chi^2 = N$, the number of measurements.

5.2.4 Spatial averaging kernels

Another way to think about the effect of γ is to examine the interplay between the stability and the resolution of the inversion solution. For the sake of a convenient notation, define the matrix D as

$$D \equiv A^T A + \gamma H. \tag{5.15}$$

We can therefore express the solution $\hat{u}$ to equation 5.14 as

$$\hat{u} = D^{-1}(A^T b). \tag{5.16}$$

Substituting for b from equation 5.8,

$$\hat{u} = D^{-1} A^T A u. \tag{5.17}$$

Equation 5.17 shows that each parameter of the model solution $\hat{u}$ can be expressed as a linear combination of the parameters of the "real" velocity u. For this reason, each row of the $M \times M$ matrix $D^{-1}A^T A$ is called an *averaging kernel* for the solution. For the particular problem under consideration here, each element of the vector u corresponds to a particular latitude and radius, so the kernel gives a representation of the spatial resolution of the solution.

5.2.5 Error analysis

As in the case of all least squares fitting techniques, the uncertainties in the model parameters are determined by the uncertainty in the measurements and by the characteristics of the kernels K. In both the regularized and standard forms, the error information is contained in the covariance matrix of the solution. In the case of regularized least squares, however, the formulation is slightly more complicated.

The variance in the model velocity $\hat{u}_j$ is defined as

$$\sigma^2(\hat{u}_j) = \sum_{i=1}^{N} \sigma_i^2 \left(\frac{\partial \hat{u}_j}{\partial z_i} \right)^2 \tag{5.18}$$

where σ_i^2 is the variance in measurement z_i. Writing equation 5.16 in component form,

$$\hat{u}_j = \sum_{k=1}^{M} [d_{jk}]^{-1} \sum_{i=1}^{N} \frac{z_i K_{ki}}{\sigma_i^2} \tag{5.19}$$

so that

$$\frac{\partial \hat{u}_j}{\partial z_l} = \sum_{k=1}^{M} [d_{jk}]^{-1} \frac{K_{kl}}{\sigma_l^2}. \tag{5.20}$$

Here I have represented the elements of D^{-1} symbolically as $[d_{ij}]^{-1}$. Inserting this result into definition 5.18 gives

$$\sigma^2(u_j) = \sum_{k=1}^{M} \sum_{l=1}^{M} [d_{jk}]^{-1} [d_{jl}]^{-1} [A^T A]_{kl}, \tag{5.21}$$

or in matrix form,

$$\sigma^2(u_j) = [D^{-1} A^T A (D^{-1})^T]_{jj}. \tag{5.22}$$

Note that in the case with no regularization ($\gamma = 0$) the variance reduces to $[D^{-1}]_{jj}$ as we expect.

Equation 5.22 shows that the *error propagation* — the way that uncertainty in the measurements is transformed into uncertainty in the velocities — depends not only on the model, but also on the choice of regularization parameter γ and the regularization operator H in equation 5.15.

In fact, another way to visualize the effect of the tradeoff parameter γ is to imagine the balance between the error propagation and the resolution. With little regularization, the averaging kernels are well localized, but the solution is very sensitive to errors in the measurements; when γ is large, the solution is stable with respect to errors but the resolution is very poor.

5.3 Additional Constraints

The previous section describes how *regularization* is used to select a “good” solution from the infinity of models which might be compatible with a set of noisy measurements. However, the use of such a selection mechanism is not really based on physics, but on some *a priori* ideas about what the velocity field should look like.

In addition to some type of smoothness, it would also be desirable to select a model solution where the velocity field $\mathbf{u}$ satisfies the continuity equation 2.40. In the case of the large-scale, steady flows measured here, this reduces to

$$\nabla \cdot (\rho(r)\, \mathbf{u}) = 0. \tag{5.23}$$

Unfortunately, as noted in section 2.3.3, the radial component of the meridional circulation is essentially undetectable in the time-distance technique, so that it is not possible to constrain the flow field by applying equation 5.23 at each grid point. However, there is one important case where the conservation of mass can be applied to constrain the solution.

If the model is allowed to extend all the way to the bottom of the convection zone, and if the meridional circulation is assumed not to penetrate into the radiative zone, then the total amount of mass flowing northward must be equal to the total amount flowing southward. In fact, it is possible to state the constraint in stronger terms: for every latitude, the net amount of mass crossing that latitude must be zero.

The method used in this work to impose this condition is a so-called "barrier method." The condition of mass conservation is cast in matrix form by creating a matrix C which satisfies

$$u^T C u = \sum_{i=1}^{M_1} \left(\sum_{j=1}^{M_2} \rho_j U_{ji}\, dr_j \right)^2 = 0. \tag{5.24}$$

Here the velocity vector u is treated symbolically as a $(M_2 \times M_1)$ matrix U inside the sum; the indices j and i indicate radius and latitude, respectively.

Once the matrix C has been formed, the condition $u^T C u = 0$ is satisfied in an approximate sense by solving a modified version of equation 5.14:

$$(A^T A + \gamma H + \beta C) u = A^T b. \tag{5.25}$$

Thus, the condition that mass be conserved is treated as an extra regularization condition; the deviation from perfect continuity can be made arbitrarily small by making β arbitrarily large.

Solving inverse problems is an art and a science in itself; the methods described here have been used as a starting point. No doubt the methods of inversion, and the approximations used in the modeling, will be greatly improved as time-distance helioseismology becomes more mature. The next chapter will describe the numerous results which can be obtained using this relatively simple approach.

Chapter 6

Results

The results of this work can be divided into two broad categories: measurements of the meridional circulation; and measurements of the rotation and other zonal flows. This chapter is therefore divided into two corresponding sections. I begin with the section on the rotation, since it allows for some explanation of the methods and a comparison with more established techniques in helioseismology. The most important new results in this work can be found in section 6.2 on the observations of the meridional circulation.

6.1 Rotation and Zonal Flows[1]

For the purposes of measuring the rotation deep in the solar convection zone, I used measurements from 792 days of Structure images. The maximum distance used in the cross correlations was 19.2°, which corresponds to a turning radius of $0.88\,\mathrm{R}_\odot$.

6.1.1 Inversion method and regularization

The discussion in chapter 5 shows that the solution of equation 2.44 for the internal velocity $u(r, \lambda)$ involves the choice of a particular regularization scheme and then a

---

[1] Early versions of these results appeared in the conference proceedings of IAU Symposium 185 (Giles and Duvall, 1998) and the SOHO6/GONG98 Workshop (Giles et al., 1998). Additional results have been presented in oral or poster form at the GONG99 Workshop and other conferences.

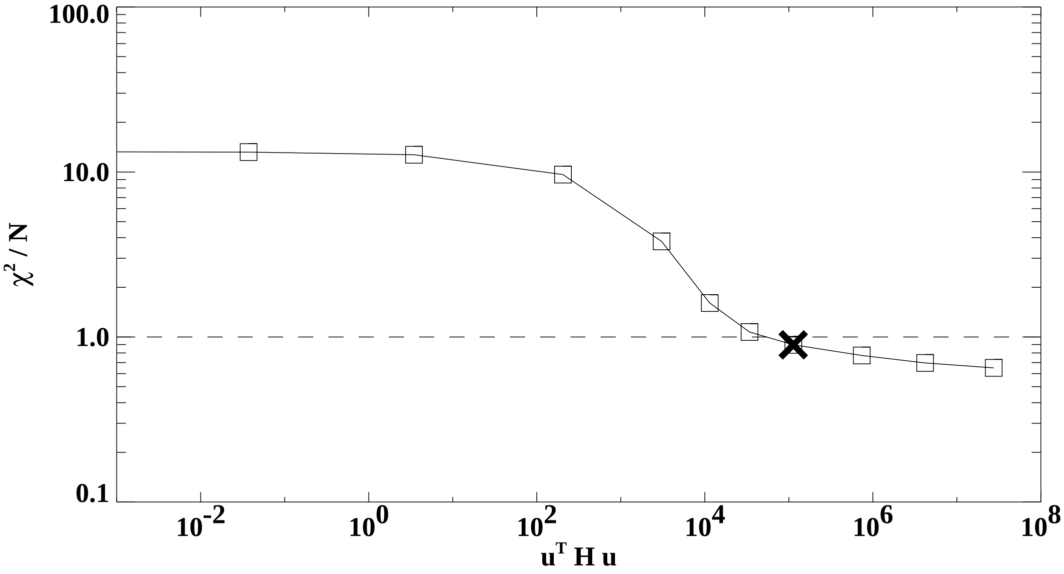

Figure 6.1: This L-curve shows the relationship between the "smoothness" and the "goodness-of-fit" of the solutions to an inversion for the rotation velocity. The dashed line marks the point where χ^2 (see equation 5.7) is equal to the number of measurements. The horizontal axis represents the deviation from perfect smoothness, with $u^T H u$ being mathematically described by equation 5.13. The point marked with × marks the solution which is shown in figures 6.2 and 6.3.

choice of trade-off parameter which gives the "best" solution. This necessarily involves some *a priori* assumptions about the real velocity profile in the Sun.

For the results presented here, the matrix H in equation 5.14 was chosen to be H_Ω from equation 5.13. The tradeoff parameter γ was then chosen by examining a trade-off curve like the one shown in figure 6.1. In this plot, each square represents a solution of equation 5.14 for a particular choice of γ, which is increasing from right to left. The solutions on the right side of the plot fit the data best, but are not physically appealing because of the large gradients in velocity. The solutions on the left side are very smooth but do not fit the measurements.

There are several criteria which can be used for choosing the best value of γ using the L-curve in figure 6.1. First, the optimal compromise between "smoothness" and "goodness-of-fit" can be achieved by choosing a solution near the bend in the L.

Once we have achieved such a solution, any further increase in the magnitude of the regularization causes a relatively small improvement in smoothness, at the expense of a large decrease in the agreement with the measurements. Furthermore, if the measurement errors have been reliably determined, then the chosen solution should have a value of χ^2 which is roughly equal to the number of measurements; this then gives the solution which is as smooth as possible and yet still fits the data by some objective criterion.

In this particular case, the inversion results can be compared to the known internal rotation, as determined from normal mode frequency splittings. This is the method that has been used to choose a particular solution from the set of solutions depicted in figure 6.1. The symmetric part of the time-distance solution has been compared with a solution from the MDI frequency splittings (Larsen, 1999). It is reassuring that this solution is also near the bend in the L, and that the calculated χ^2/N is close to 1. The consistency of these different criteria lend confidence to the estimated measurement errors and to the final results. The value of χ^2/N is 0.90, which I interpret as an indication that the estimated measurement errors are slightly too large.

6.1.2 Comparison to modal approach

Since the use of the time-distance method to measure flows is a relatively new area of scientific exploration, it is useful to compare the results of this method with the results of the more well-established modal approach. As outlined in section 2.2.1, the global approach in helioseismology yields information about the component of the angular velocity which is symmetric about the solar equator. Therefore, for the purpose of comparison it is necessary to take the symmetric part of the time-distance results.

The inversion techniques outlined in chapter 5 give a reconstruction of the velocity as a function of radius and latitude; this can be converted to an angular frequency by the formula

$$\frac{\Omega}{2\pi}\,[\mathrm{nHz}] = v\,[\mathrm{m/s}]\,\frac{10^9}{r\cos\lambda}. \tag{6.1}$$

I then obtain the symmetric part of $\Omega/2\pi$ by calculating the mean of the velocities

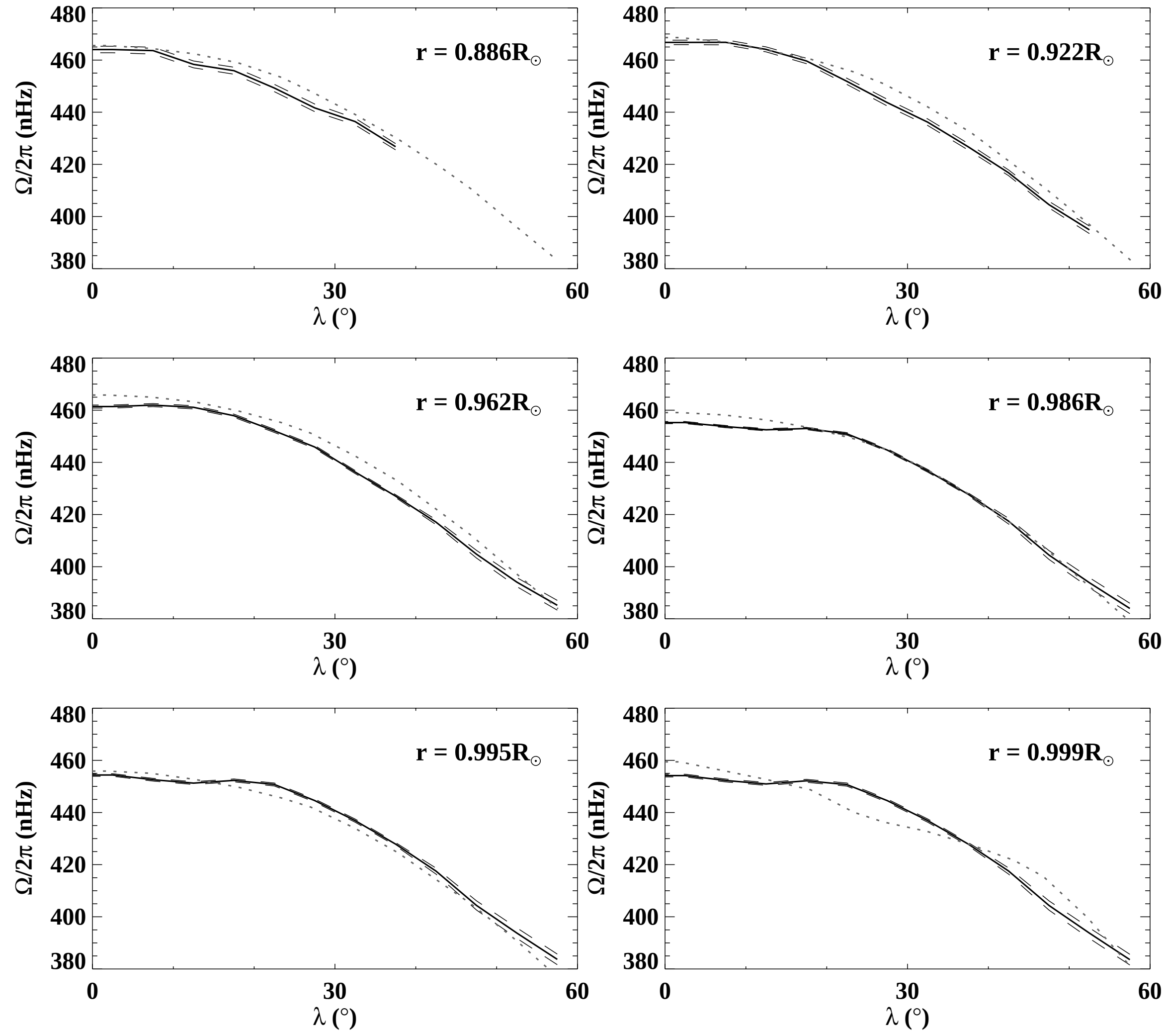

Figure 6.2: Comparison of the time-distance and normal mode methods for determining the solar rotation. The angular frequency is plotted versus latitude for six different choices of radial coordinate. The dotted curve is the result of an OLA inversion of MDI frequency splittings. The solid curve is the symmetric component of the time-distance result from this work; the dashed lines are the formal errors from the inversion.

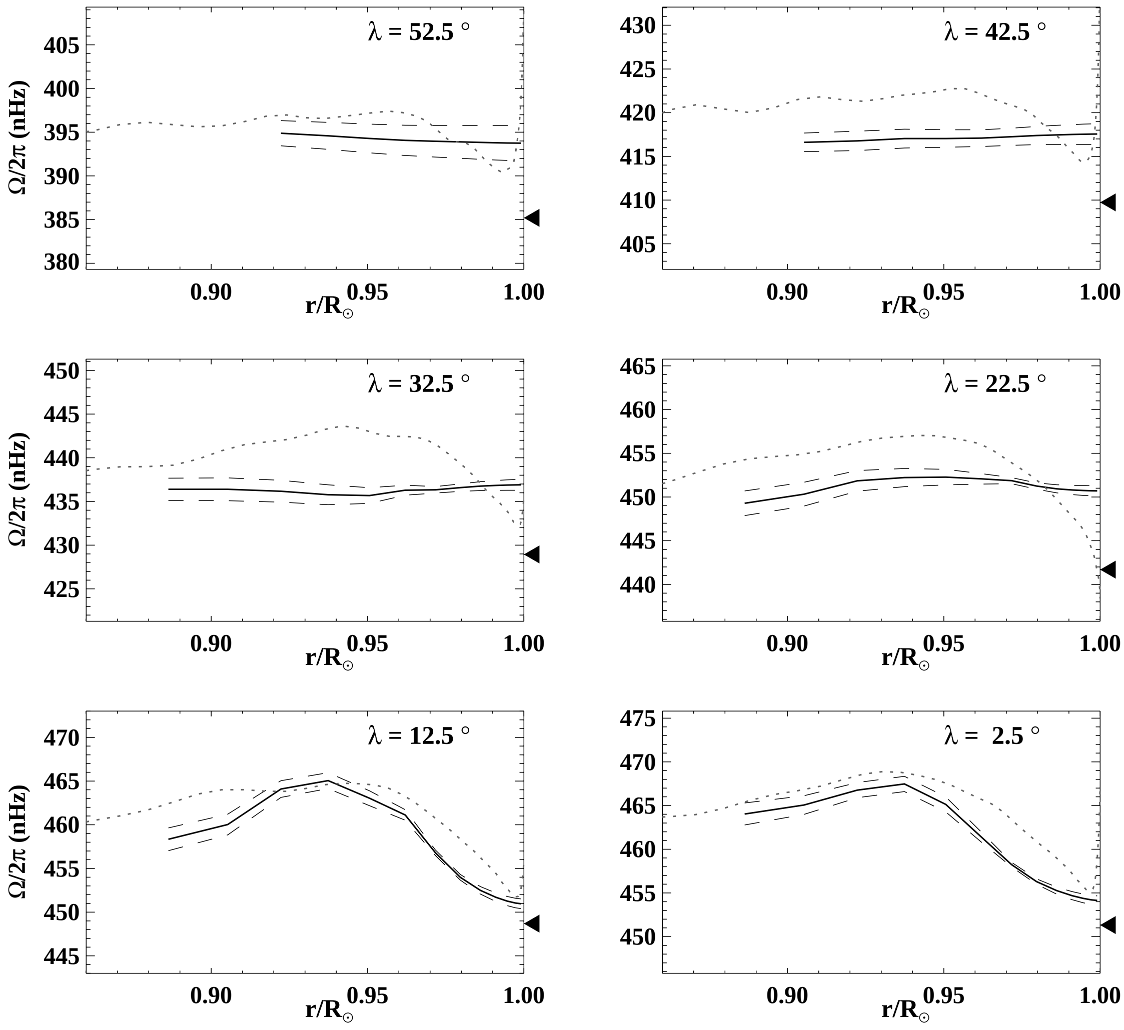

Figure 6.3: Comparison of the time-distance and normal mode methods for determining the solar rotation. The angular frequency is plotted versus radius for six different latitudes. The dotted curve is the result of an OLA inversion of MDI frequency splittings. The solid curve is the time-distance result from this work; the dashed lines are the formal errors from the inversion. The arrow on the right-hand axis in each plot represents the surface rotation rate from Snodgrass (1984).

in the northern and southern hemispheres, weighted by the formal errors from the inversion. For comparison, I use an OLA inversion of the MDI frequency splittings[2] The frequency splittings were measured from 144 days of Structure program images, and the inversion results extend to below the bottom of the convection zone; only the region which overlaps with the time-distance results is presented here.

Figures 6.2 and 6.3 show a quantitative comparison of the two measured profiles. The first set of figures shows the angular velocity as a function of latitude, for different depths; obviously, the time-distance method can accurately capture the differential rotation. The plots for the smallest values of r do not extend as far in latitude because of geometrical considerations which limit the maximum travel distance. In both figures 6.2 and 6.3, the dashed lines represent the formal errors (one standard deviation) from the time-distance inversion, calculated as described in section 5.2.5. The errors for the frequency splitting result are on the order of 1 nHz, which is so small as to be unimportant in the comparison.

Although figure 6.2 shows that there is good qualitative agreement between the two methods, the large range of angular velocities means that the differences between the two measurements can be hidden. These differences can be more clearly seen in figure 6.3, where the angular velocity is plotted, as a function of radius, for different latitudes. At low latitude, the two results are in good qualitative agreement; at higher latitudes, the agreement is not as good.

In figures 6.2 and 6.3, it should be noted that the "flattening" of the angular velocity seen, for example, at high latitudes, is characteristic of the particular choice of the regularization matrix $H = H_\Omega$ in equation 5.14. The regularization, if allowed to act independently of any measurements, will give an angular velocity which is uniform everywhere. This is the "default" solution in regions where the model is essentially unconstrained by the data, either due to large measurement errors or low sensitivity.

Another way to think about this behaviour is in terms of spatial averaging kernels,

---

[2] The OLA inversion result and averaging kernels were provided by R. M. Larsen. Although different inversion techniques and different instruments give slightly different results for the frequency measurements (Schou et al., 1998), at the level of precision considered here all the inversions are identical.

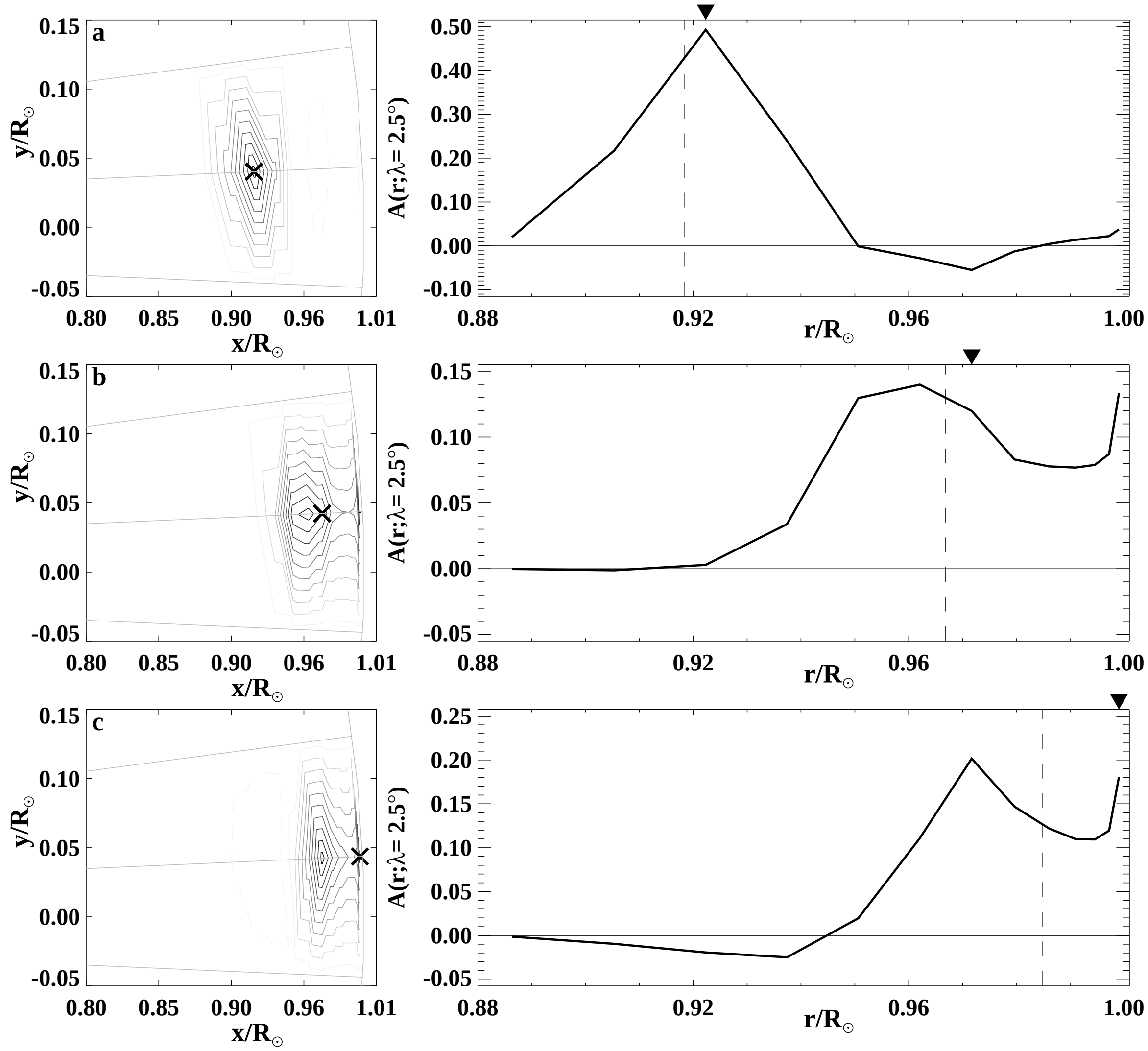

Figure 6.4: Selected averaging kernels for the time-distance inversion in figures 6.2 and 6.3. The plots in the left-hand column are contour plots of three different averaging kernels. The contour spacing is 5% of the maximum amplitude of each kernel; dashed contour lines indicate a negative amplitude. The nominal locations for the three kernels, marked with the symbol ×, are: (a) $r = 0.920\,\mathrm{R}_\odot, \lambda = 2.5°$; (b) $r = 0.966\,\mathrm{R}_\odot, \lambda = 2.5°$; and (c) $r = 0.986\,\mathrm{R}_\odot, \lambda = 2.5°$. In the right-hand column, a cross section of each kernel is plotted, as a function of radius, at the central latitude. The arrow on each plot marks the nominal radius of the kernel; the dashed line marks the location of the centroid.

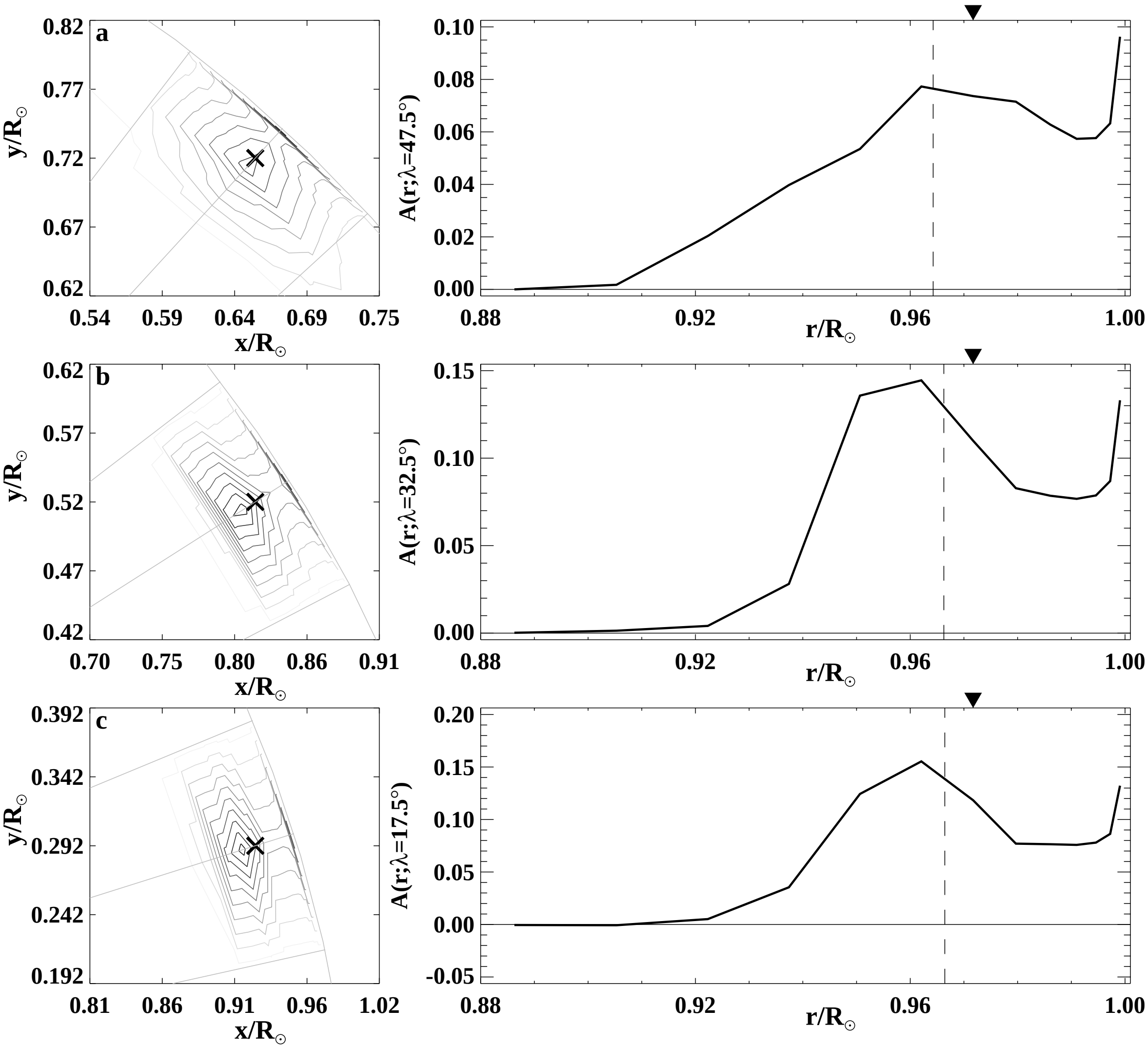

Figure 6.5: Selected averaging kernels for the time-distance inversion in figures 6.2 and 6.3. The symbols and contours are the same as for figure 6.4. In this case the kernels all have the same nominal radius $r = 0.966\,\mathrm{R}_\odot$, but different latitudes: (a) $\lambda = 47.5°$; (b) $\lambda = 32.5°$; and (c) $\lambda = 17.5°$. Note for comparison that the nominal radius is also the same as for figure 6.4(b).

as outlined in section 5.2.4. To make a more even comparison between the two methods, it is important to examine the differences between the averaging kernels. Figures 6.4 and 6.5 show selected averaging kernels for the time-distance inversion. One striking feature of the averaging kernels is that they are very well localized in latitude. If we recall that each averaging kernel is created from a weighted sum of the sensitivity kernels, this is perhaps not surprising (a typical sensitivity kernel is shown in figure 5.1). However, it should be noted as an advantage of this method over the frequency-splitting approach. In fact, the latitude resolution in this case is limited by the extent of the averaging used in making the measurements; because I averaged together all the cross correlations for five-degree bands of latitude, the averaging kernels cannot be narrower than five degrees in that dimension.

In the radial direction, on the other hand, the averaging kernels are not well localized; in fact, in some regions they have very small amplitudes near their nominal location. Again, this is related to the shape of the sensitivity kernels. For example, the shortest travel distance included in this analysis is $\Delta = 3^\circ$; the lower turning point for a ray with this travel distance is about $0.98\,\mathrm{R}_\odot$. Since the ray sensitivity kernels are rather small between the upper and lower turning points, it is not possible to construct an averaging kernel which is localized between about $0.98\,\mathrm{R}_\odot$ and the surface.

Given the width of the averaging kernels, it is perhaps not surprising that there are some significant differences between the two different profiles in figures 6.3. One way to compare the two methods more evenly is to convolve the frequency splitting result with the averaging kernels from the time-distance result, and vice versa. This results in two models with comparable (although very poor) resolution.

Figure 6.6 shows the results of this comparison. Clearly there is great improvement in the agreement between the two models. Direct comparison of the averaging kernels shows that although the time-distance kernels span a narrower range in latitude, the modal kernels in general have smaller sidelobes and better resolution in the radial direction. Since the OLA (Optimally Localized Averaging) technique is explicitly designed to construct well-behaved averaging kernels, this is perhaps not surprising. A similar approach might be applied to the time-distance measurements

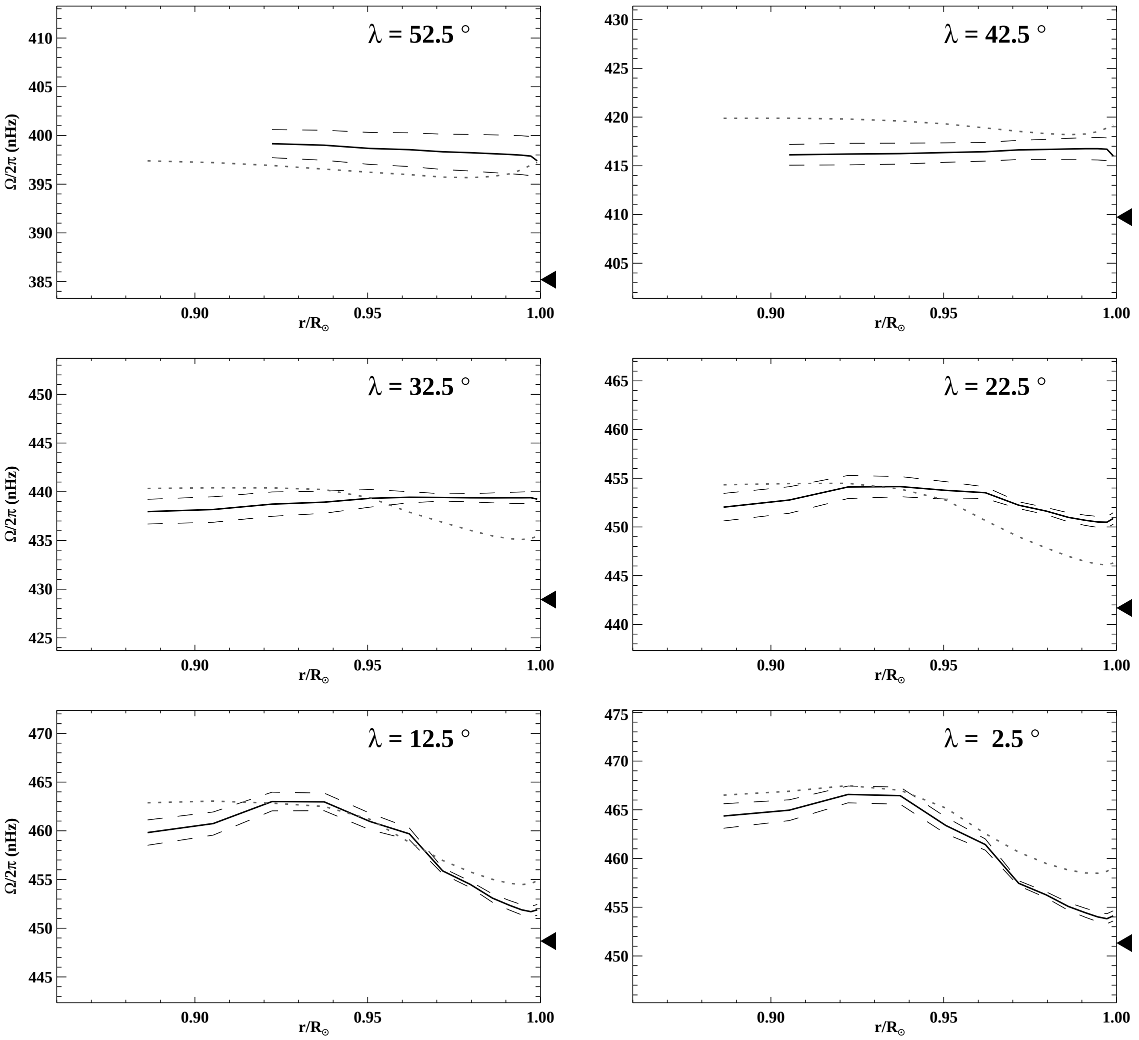

Figure 6.6: The comparison in figure 6.3 is repeated here, but the frequency splitting result (dotted line) has been convolved with the averaging kernels from the time-distance inversion, and vice versa, reducing the spatial resolution of both models so that the two methods are comparable in that regard.

in the future. The construction and optimization of inversion techniques in analysis of mode frequency splittings has been an area of vigorous study in helioseismology for nearly fifteen years; it is hoped that the expertise gathered in this research can be applied to the time-distance method as well.

6.1.3 North-south asymmetry

The comparison with the modal approach, while a useful check on the method, is not very interesting from a scientific point of view. After all, the modal approach to determining rotation — having nearly a decade head start — is unlikely to be surpassed in the first attempt. However, it is possible to learn something new about the solar rotation by looking for asymmetries between the northern and southern hemispheres.

A first step is to examine the measurements themselves. Figures 6.7 and 6.8 show the complete set of time differences for the rotation study. These measurements were made over the 792-day Structure run by the process outlined in chapter 4. The sense of the time difference is (east – west), so that a positive time difference reflects a flow in the prograde (westward) direction.

To look for asymmetries between the two hemispheres, the measurements have been divided into two groups. The open circles represent the measurements for the northern hemisphere, and the filled circles for the southern hemisphere. The measurements for particular latitudes fall along distinct curves because the velocity decreases rapidly as the latitude increases. Thus, the points with the largest time differences are for measurements made near the equator, and the smaller time differences are for measurements closer to the poles. It should be stated that this spreading is largely removed by the image tracking procedure mentioned in section 4.1. The removed velocities have here been added back into the data using the known interior profile (from global helioseismology) and the ray sensitivity kernels calculated for the time-distance inversion[3].

As might be expected, the measurements from the two hemispheres in figure 6.7

---

[3] Since the model interior profile is symmetric, the time differences added on are also symmetric.

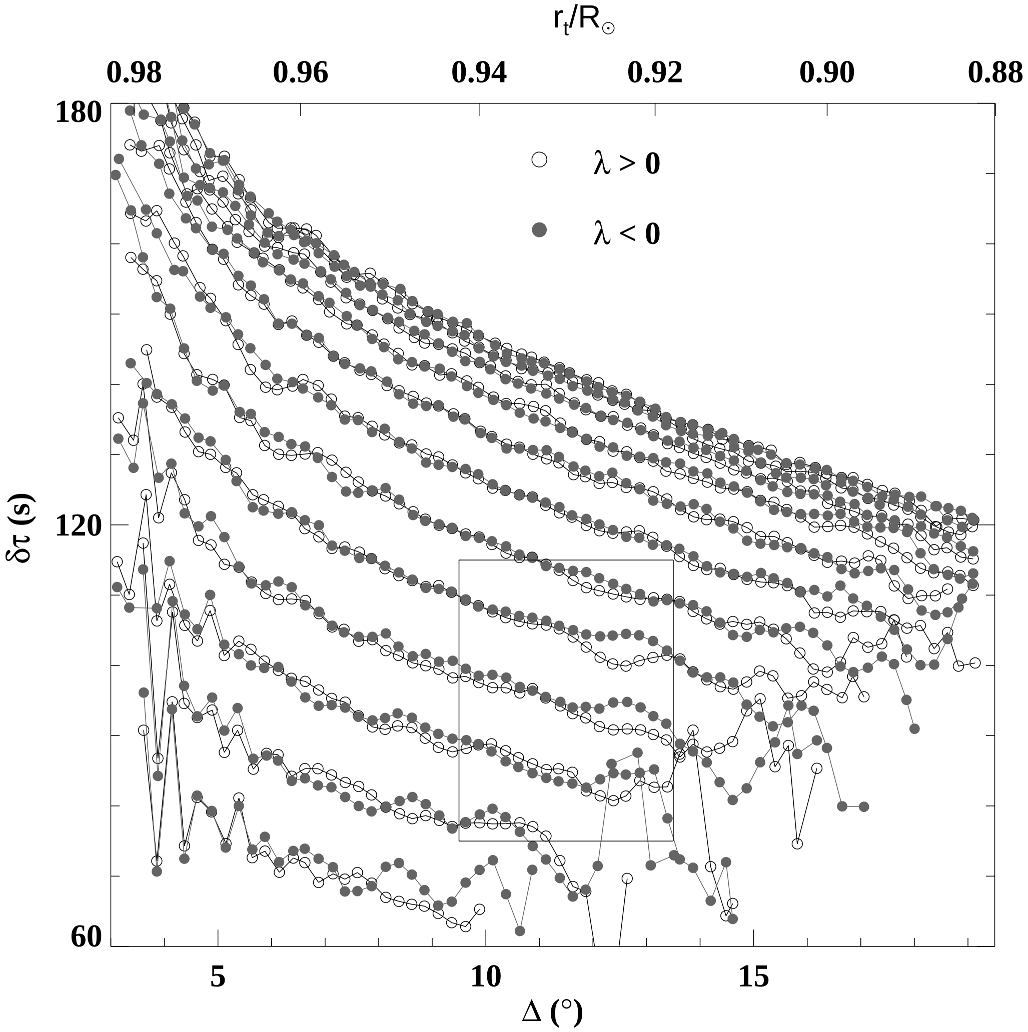

Figure 6.7: Measurements of the time differences from 792 days of MDI Structure program Dopplergrams. The vertical axis shows the time difference, in seconds, between eastward- and westward-propagating waves; the horizontal axis on the bottom shows the travel distance, in degrees. The upper horizontal axis shows the turning point r_t for rays which travel a distance Δ between surface reflections. The open circles are for measurements in the northern hemisphere, and the filled circles for measurements in the southern hemisphere. The interesting feature inside the small box is shown in more detail in figure 6.8.

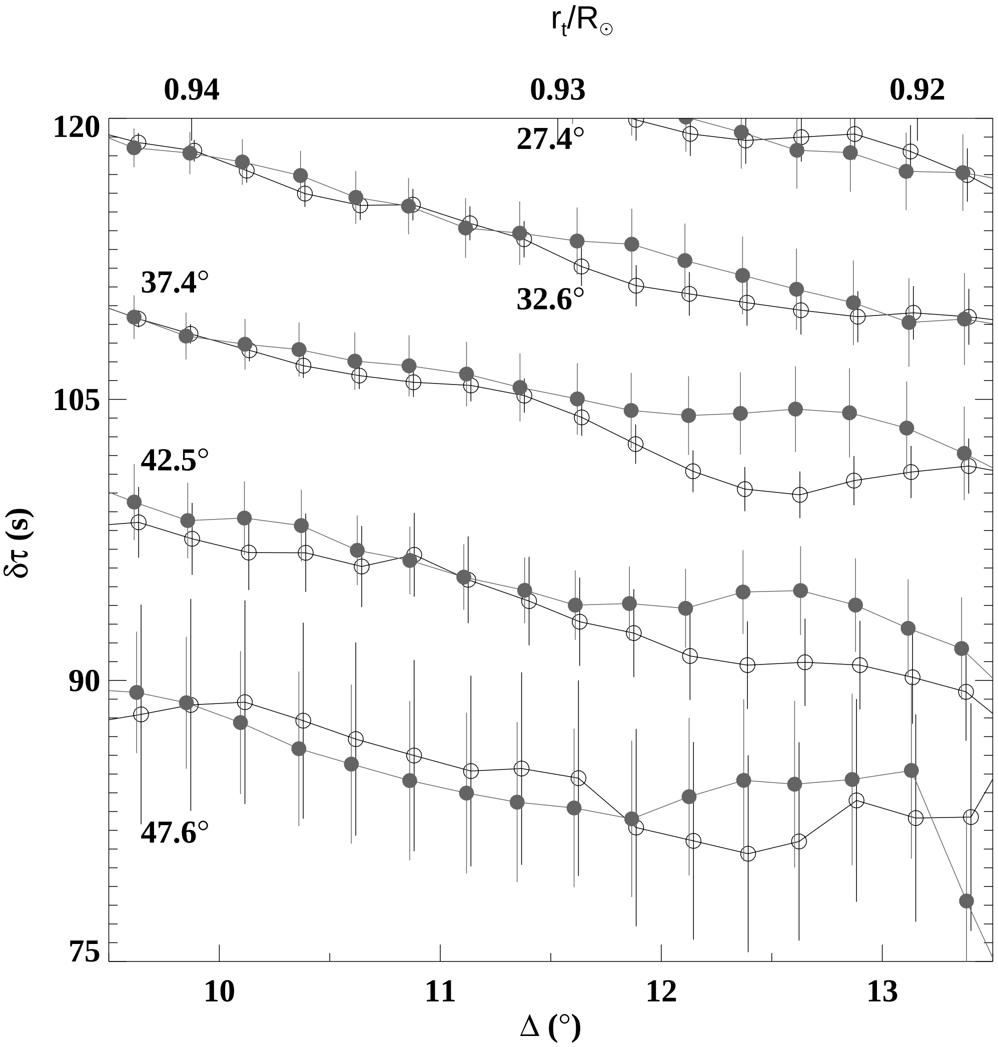

Figure 6.8: A smaller region of figure 6.7 has been replotted here, with measurement errors. Again the open circles are for measurements in the northern hemisphere, and filled circles for the southern hemisphere. Measurements for particular latitudes have been joined together by line segments; the latitude for each set of measurements is indicated on the left-hand side of the figure. The measurements fall along well-separated curves, reflecting the decrease in the zonal velocity at higher latitudes. There is an interesting and significant asymmetry noted between the northern and southern hemispheres, localized above 35° latitude and near a radius of $0.925\,\mathrm{R}_\odot$.

generally agree quite well with each other. However, one obvious deviation from this symmetry can be seen in some of the measurements near $\Delta = 12.5°$. This region has been expanded in figure 6.8. There is a marginally significant difference between the northern and southern hemispheres for latitudes between 30 and 50 degrees and distances between 12 and 13 degrees. These distances correspond to rays with turning points near $r = 0.925\,\mathrm{R}_\odot$. The amplitude of the difference is about 4 seconds, or roughly 3% of the surface rotation rate at that latitude. Since the time difference is accumulated as the integral along the ray path, the local perturbation must be considerably larger than this.

It is worth noting that the measurement process is exactly symmetric about the equator, with two exceptions. The first is that the solar B_0 angle[4] varies during the course of the year, which causes the oscillation signal at high latitudes to vary in strength, due to line-of-sight projection effects. The measurements shown here were made over a period slightly longer than two years, so the effect of this asymmetry should be small. Second, the image scale[5] is not accurately known and may not be exactly symmetric. However, any north-south differences in the plate scale should be quite small. At any rate, it is difficult to imagine a distortion which would give rise to such a localized asymmetry in the measurements.

The evidence therefore points to an asymmetry in the rotation of the solar interior. To estimate the location and magnitude of this perturbation, I have created a series of velocity profiles with different asymmetric perturbations. The "reference" model was the result of the frequency splitting inversions presented in figures 6.2 and 6.3. To this profile I then added a localized perturbation which was positive (fast) in the northern hemisphere and negative (slow) in the southern hemisphere. The perturbation is described by the smooth function

$$v_p = A \exp\left[-\frac{(r - r_p)^2}{2\,\delta r^2}\right] \exp\left[-\frac{(\lambda - \lambda_p)^2}{2\,\delta\lambda^2}\right]. \tag{6.2}$$

With this perturbation added to or subtracted from the reference velocity, I then

---

[4] See also the discussion in appendix A.

[5] See also the discussion in section 4.7.2.

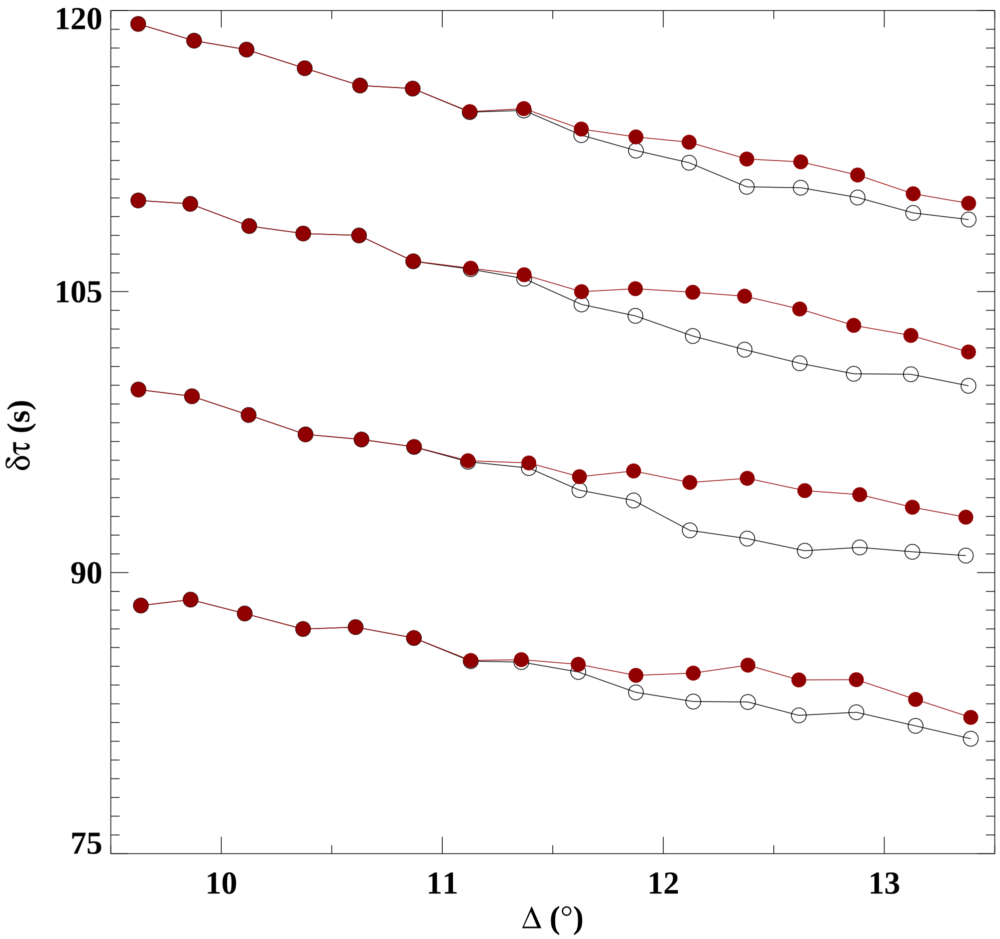

Figure 6.9: Travel time differences $\delta\tau$ have been calculated as a function of distance Δ for an asymmetric rotation profile. The velocity profile used was the frequency-splitting measurement of the internal rotation, with a localized perturbation added in each hemisphere as described in the text. The set of measurements chosen is the same as that in figure 6.8.

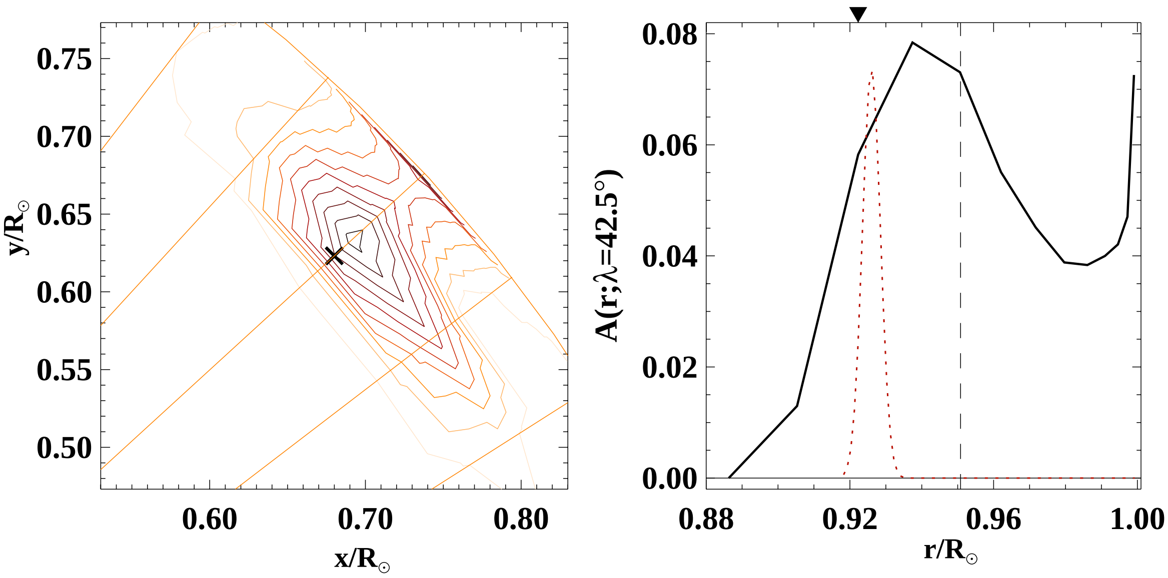

Figure 6.10: The left-hand figure shows the averaging kernel for $r = 0.920\,\mathrm{R}_\odot$ and $\lambda = 42.5°$, which is where the postulated asymmetry in the rotation is localized. The contour levels are 5% of the kernel amplitude, as in figures 6.5 and 6.4. The right-hand plot shows the radial cross section. The dotted curve shows the shape of the cross section of the perturbation which was used to create figure 6.9.

calculated the travel time differences for the set of measurements shown in figure 6.8. The results for one such perturbation v_p are shown in figure 6.9. For this particular case, I used the parameters $A = 200\,\mathrm{m/s}$, $r_p = 0.926\,\mathrm{R}_\odot$, $\delta r = 0.0025\,\mathrm{R}_\odot$, $\lambda_p = 41.0°$, and $\delta\lambda = 6.0°$. The general behaviour seen in figure 6.8 is reproduced quite well by this model, in particular the fact that the time differences are quite well-localized in latitude and distance, and that there appears to be no significant asymmetry for distances shorter than about 11.5°. The magnitude of the perturbation is quite large — about 14% of the unperturbed velocity at (r_p, λ_p). Also, the perturbation is extremely narrow in the radial direction, with a full width at half maximum of only 4×10^6 m.

Unfortunately, such a perturbation is impossible to find in the inversions described in section 6.1.2. The problem is essentially one of spatial resolution; figure 6.10 shows

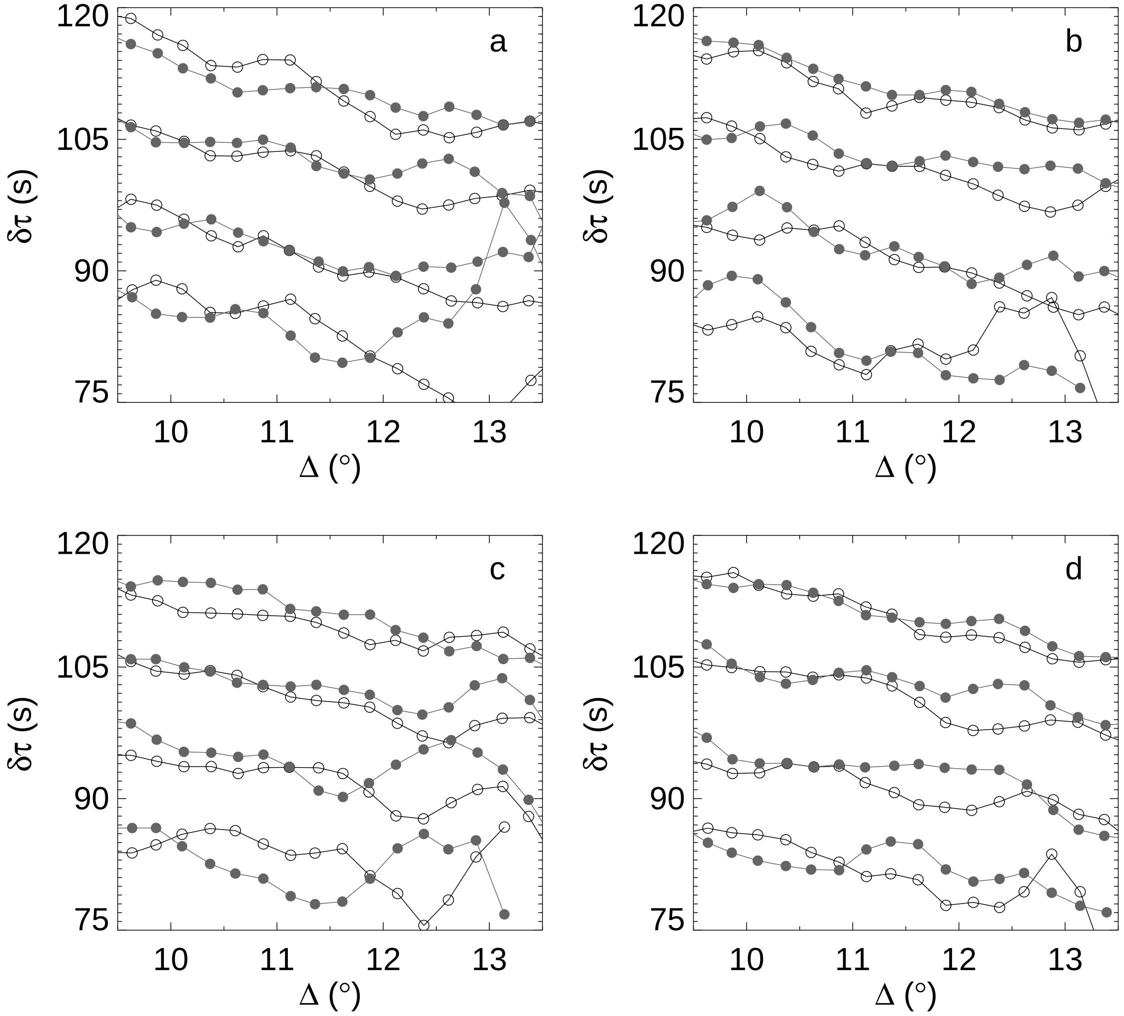

Figure 6.11: The measurements from figure 6.8 have been made for four six-month intervals: (a) May to November, 1996; (b) November, 1996 to May, 1997; (c) May to November, 1997; (d) November, 1997 to June, 1998. The latitude of each curve is the same as for figure 6.8, and again the open circles are for the northern hemisphere and the filled circles for the southern. For the two central curves (latitudes 37.4° and 42.5°), the rotation is persistently higher in the southern hemisphere than in the northern.

the averaging kernel for $\lambda = 42.5°, r = 0.920\,\mathrm{R}_\odot$. Clearly the narrow asymmetric perturbation shown in the right-hand panel is not going to be resolved.

In light of the fact that solar activity changed quite dramatically over the two years of observation, it is interesting to ask whether the asymmetry in the rotation rate was present during the whole period. Figure 6.11 shows the same set of measurements as figure 6.8, but this time the time series has been divided into four time intervals. The four plots show that although the location and magnitude of the asymmetry vary somewhat, the sense and rough magnitude are basically constant over the time period in question.

6.1.4 Torsional oscillation

Since the torsional oscillation is a time-varying phenomenon, it is necessary to make time-resolved observations of the rotation velocity in order to see any motions which might be present. Since the objective is to make an estimate of the depth dependence of the zonal flow bands, it is best to have as long a time series as possible for each observation, in order to increase the signal-to-noise of the measurements. As a compromise, I divided the 792-day time series of Structure images into four parts and inverted each set of measurements separately.

The torsional oscillation is clearly visible in the measurements themselves; figure 6.12 shows measurements of the east-west time differences for the four different time periods. In each case, the large-scale variation of the time differences (equation 4.8) has been removed. The lowest curve is for measurements from May to November, 1996; the next is for the period from November, 1996 to May, 1997; the third is for measurements from May to November, 1997; and the highest curve covers the period from November, 1997 to June, 1998. The displacement between the curves was artificially added to show the time dependence of the torsional oscillation more clearly. The torsional oscillation is demonstrated in the way that the peaks and valleys in the velocity residual move toward the equator as time progresses.

To further study the torsional oscillation pattern at different depths, I inverted the measurements in figure 6.12 for each time period. Figure 6.13 shows the results. From

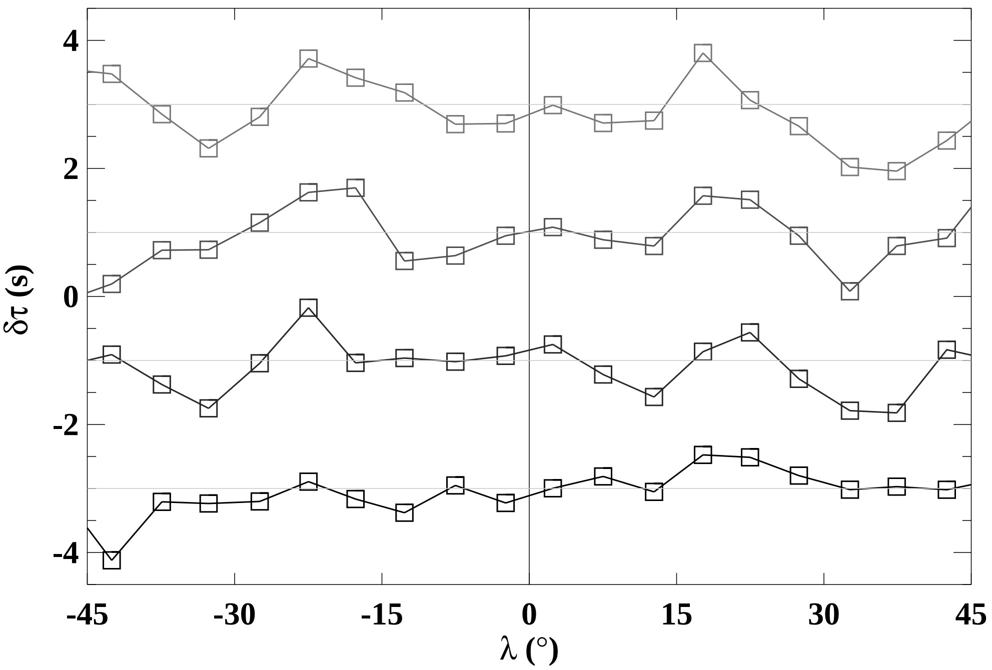

Figure 6.12: The four curves are residual time differences for the rotation measurements from four different time intervals. In each case, the time differences have had a smooth function (see equation 4.8) subtracted. The measurements shown here as a function of latitude are averaged over distances from 4 to 12 degrees. The curves have been displaced so that their mean separation is 2.5 s; time is increasing from the bottom to the top.

the velocity at each depth, I have subtracted a polynomial in even powers of $\sin \lambda$ (see equation 1.1). The upper figure shows the residuals in the surface layers, where the torsional oscillation is clearly visible. The averaging kernels for this location are reasonably well localized above $r = 0.95\,\mathrm{R}_\odot$ (see figure 6.14). The lower figure shows the residuals for the deeper layers; the averaging kernels are well localized below $r = 0.95\,\mathrm{R}_\odot$. Here there is no clear indication of the banded pattern characteristic of the torsional oscillation. This is in contrast with some recent results (Howe et al., 2000; Toomre et al., 2000) using frequency splittings, which found that the pattern is visible down to at least $r = 0.92\,\mathrm{R}_\odot$.

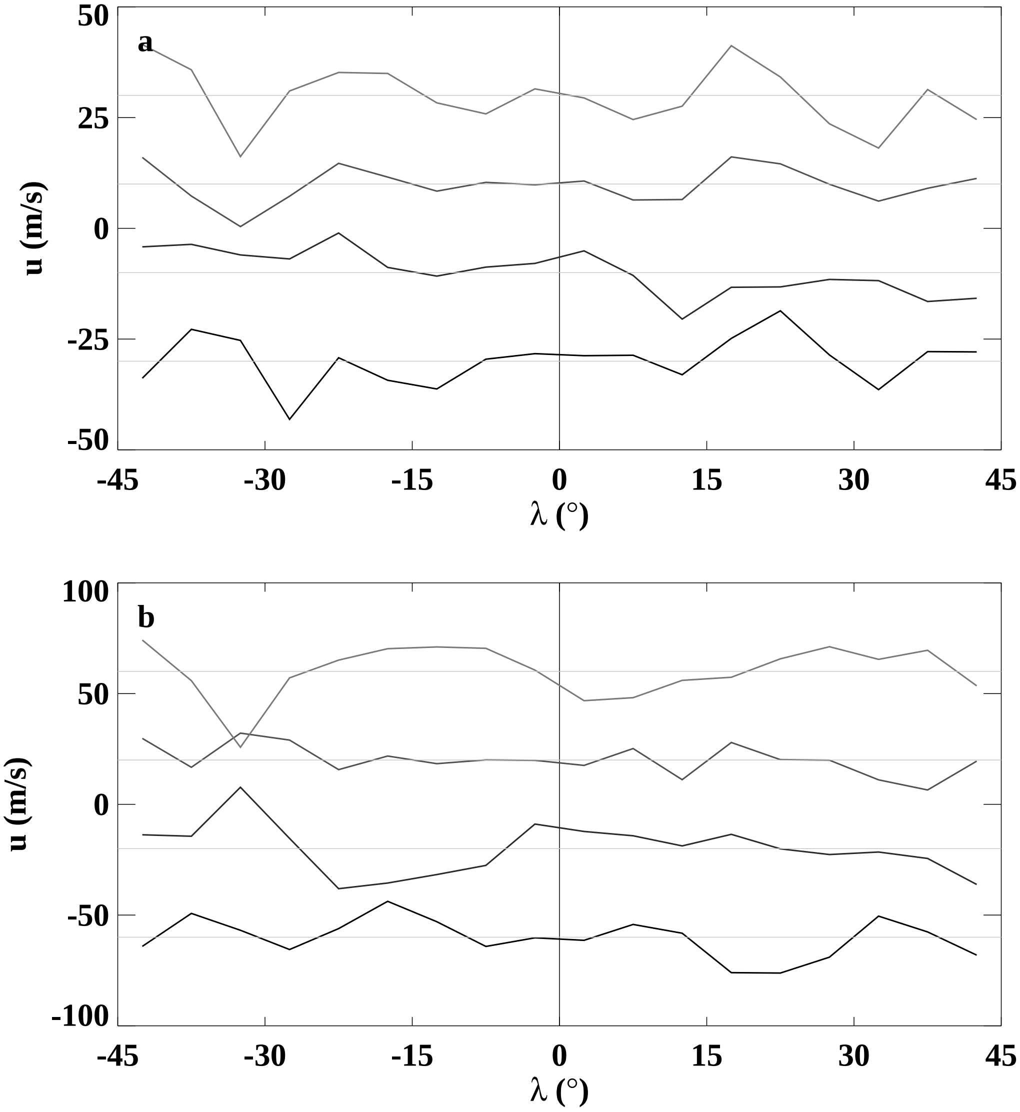

Figure 6.13: These plots show the evidence for the torsional oscillation at two different depths. The four curves in each case are for the four different time intervals, each six months long. The residuals have been displaced from zero to separate the curves. The upper plot shows the signal at the solar surface; in this region, the averaging kernels are well localized above $r = 0.95\,\mathrm{R}_\odot$. The lower plot shows the torsional oscillation for the deepest layers of the inversion, where the averaging kernels are well localized below $r = 0.95\,\mathrm{R}_\odot$ (see figure 6.14).

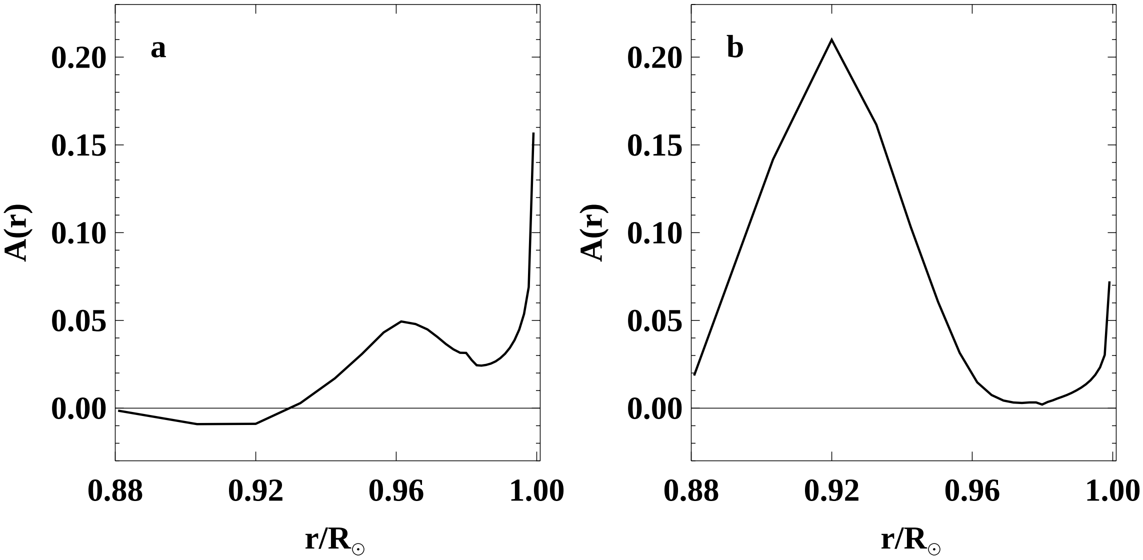

Figure 6.14: The radial cross section of the mean averaging kernels for figure 6.13(a) and (b).

Of course, there is an important difference between the two methods; the frequency splitting measurements are sensitive only to the symmetric component of the pattern, whereas these time-distance method can be used to measure the antisymmetric part as well. Figure 6.15 shows the residuals for the deeper layer again, this time decomposed into symmetric and antisymmetric components. The evidence for the torsional oscillation pattern is still not very compelling, but it is interesting to note that the lowest two curves in the upper plot and the middle two curves in the lower plot are very similar pairs. Since these four measurements should be competely independent, this may indicate some interesting time-varying patterns.

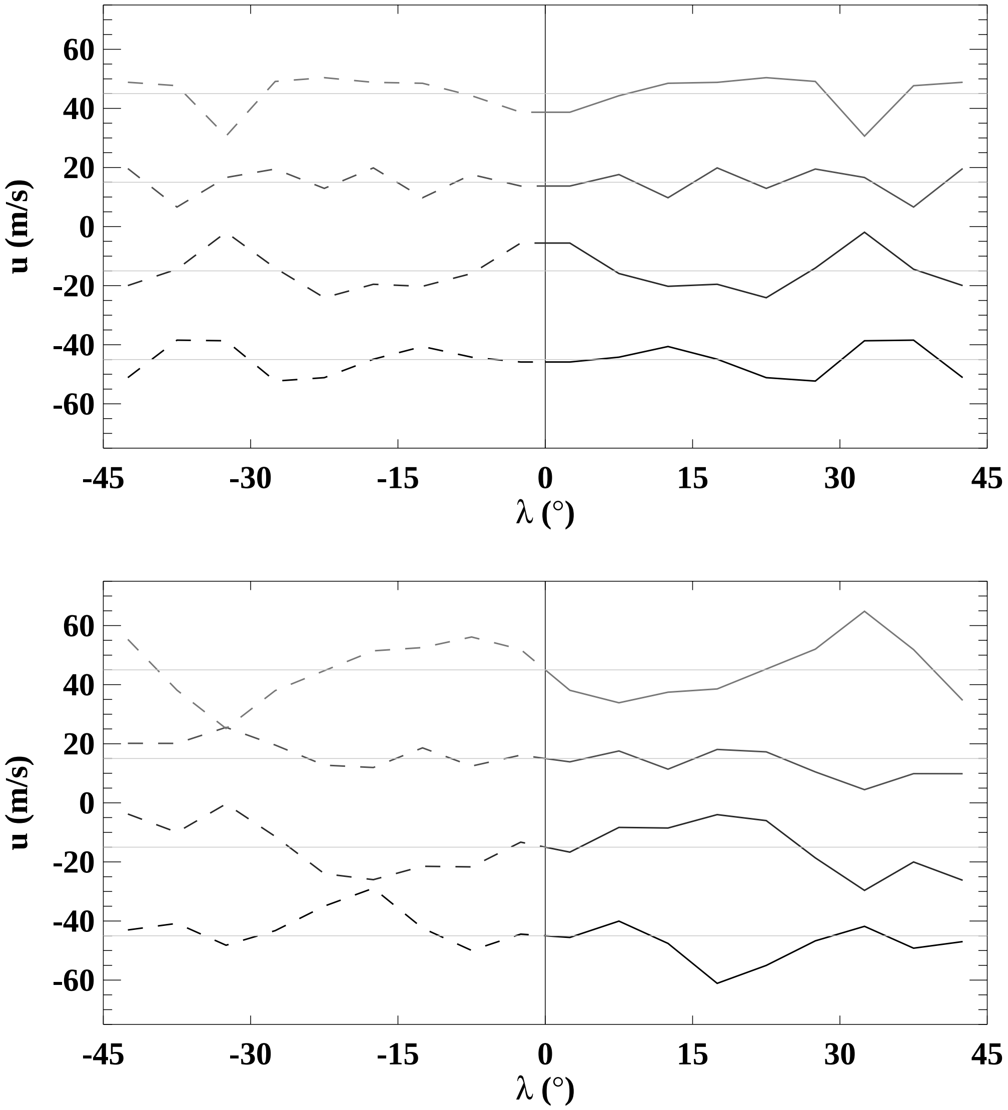

Figure 6.15: The residuals from figure 6.13 are decomposed into their symmetric (upper plot) and antisymmetric (lower plot) components.

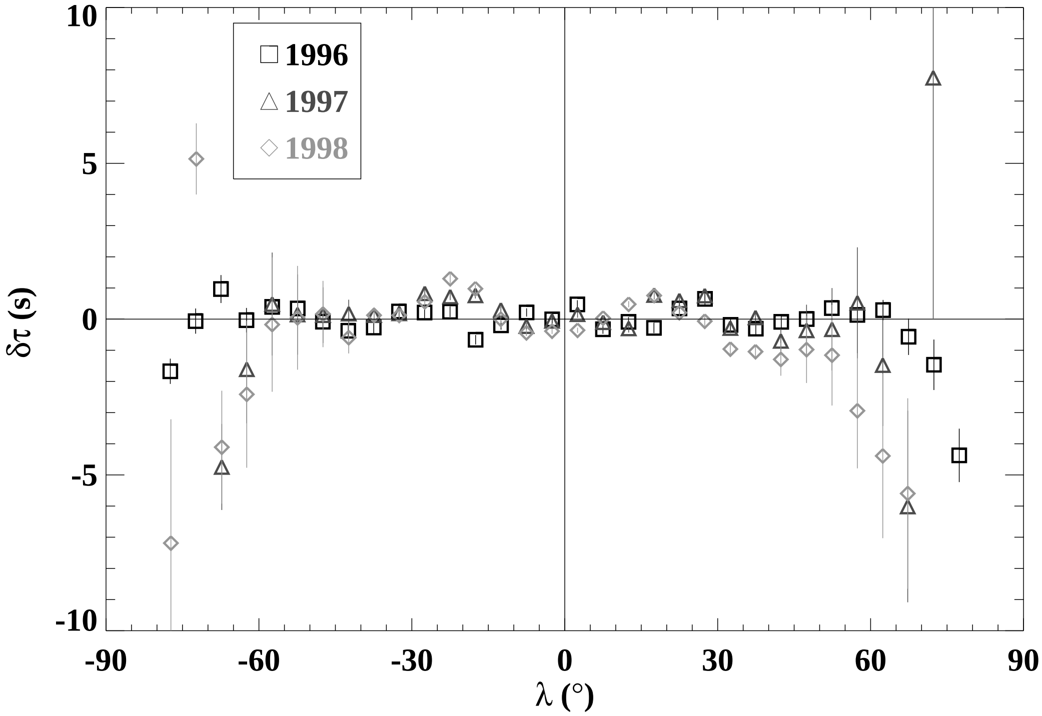

Figure 6.16: East-west time differences for the three Dynamics periods are plotted as a function of latitude. From each curve, a function of the form of equation 4.8 has been subtracted; the parameters were determined from a least-squares fit to the 1996 measurements. The distance range for these measurements is ($1° \leq 6°$); recall that for this range, a time difference of 1 s implies a depth-averaged velocity of 10 m/s (see figure 4.12).

6.1.5 Time variation of high-latitude rotation

Figure 6.16 shows the east-west time difference measurements for the three Dynamics periods. These measurements have had a smooth function subtracted, to emphasize the small differences between them (of course, the same function has been subtracted from all three sets of measurements). There are small variations in the flow measured at low latitude; these variations are signatures of the torsional oscillation. At high latitude, the measurements suggest that the polar rotation was decreasing during the rising phase of the solar cycle. This is in agreement with previous observations that the differential rotation is more pronounced during solar maximum.

Unfortunately, the measurements made at these latitudes have rather poor signal-to-noise, and it is not possible to resolve any depth dependence in the inversions. Future observations made from out of the ecliptic plane might be able to improve on this result.

6.2 Meridional Circulation[6]

6.2.1 Meridional circulation deep in the convection zone

Using the same time series of Structure images as described in section 6.1, I computed cross correlations for north-south pairs up to distances of 45°. The inversion procedure was also the same; the L-curve for the inversion is shown in figure 6.17. This set of inversions was performed with $H = H_{u/r}$ (see equation 5.12) in equation 5.14.

The results of the inversion are shown in figures 6.18 and 6.19. Since a travel distance of 45° corresponds to a turning point of $0.71\,\mathrm{R}_\odot$, the model in this case extends to the base of the convection zone. The results of the inversion clearly show a poleward flow near the solar surface, with a weak dependence on radius. This is consistent with previous results from Giles *et al.* (1998) and Braun and Fan (1998). However, none of these previous results extended below about $0.88\,\mathrm{R}_\odot$. The inversion results in figure 6.19 indicate that the poleward flow extends throughout the entire convection zone.

As with the rotation inversion results, however, it is necessary to make some comments on the limitations of the inversion results. For example, the regularization in this case will try to minimize the gradient of u/r; in areas where the sensitivity is low, or the measurement errors are large, the model will tend to show a linear variation with r. It is important also to consider the averaging kernels; some selected averaging kernels are shown in figures 6.20 and 6.21. Comparing with figures 6.4

---

[6] Some of the results presented in this section have been published in *Nature* (Giles et al., 1997), in the conference proceedings of IAU Symposium 185 (Giles and Duvall, 1998), and in the conference proceedings of the SOHO6/GONG98 Workshop (Giles et al., 1998). Preliminary results on the meridional circulation deep in the convection zone have been presented at the SOHO9 Workshop and are in preparation for submission to a peer reviewed journal.

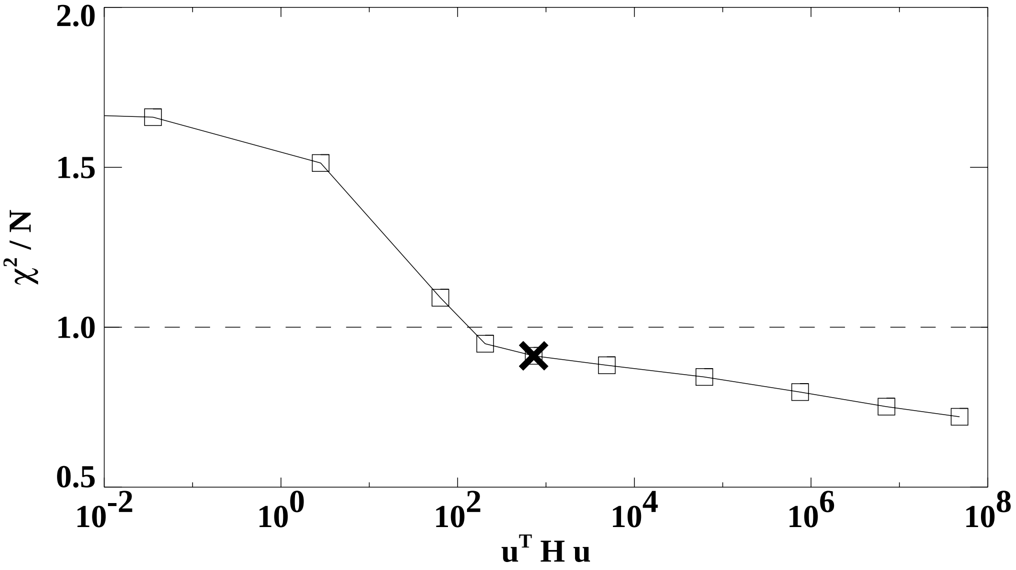

Figure 6.17: The regularization trade-off curve for an inversion of the meridional circulation.

and 6.5, it is immediately striking that the kernels for the meridional circulation are not very well localized in latitude. This is especially true at large depths, where the sensitivity for each measurement is spread over a wide range of latitudes. As a result, it would be inaccurate to state that the meridional circulation must be poleward even at the bottom of the convection zone. The next section shows another possibility which is still entirely consistent with the measurements.

6.2.2 Problem of the return flow

One important constraint on the meridional circulation profile is that mass must be conserved. That is, the flow must satisfy the continuity equation, 2.40. The results shown in figures 6.18 and 6.19 thus pose a problem; if the flow is really poleward down to the bottom of the convection zone, that would imply that the return flow is in the radiative zone.

However, an examination of the averaging kernels in figures 6.20 and 6.21 shows

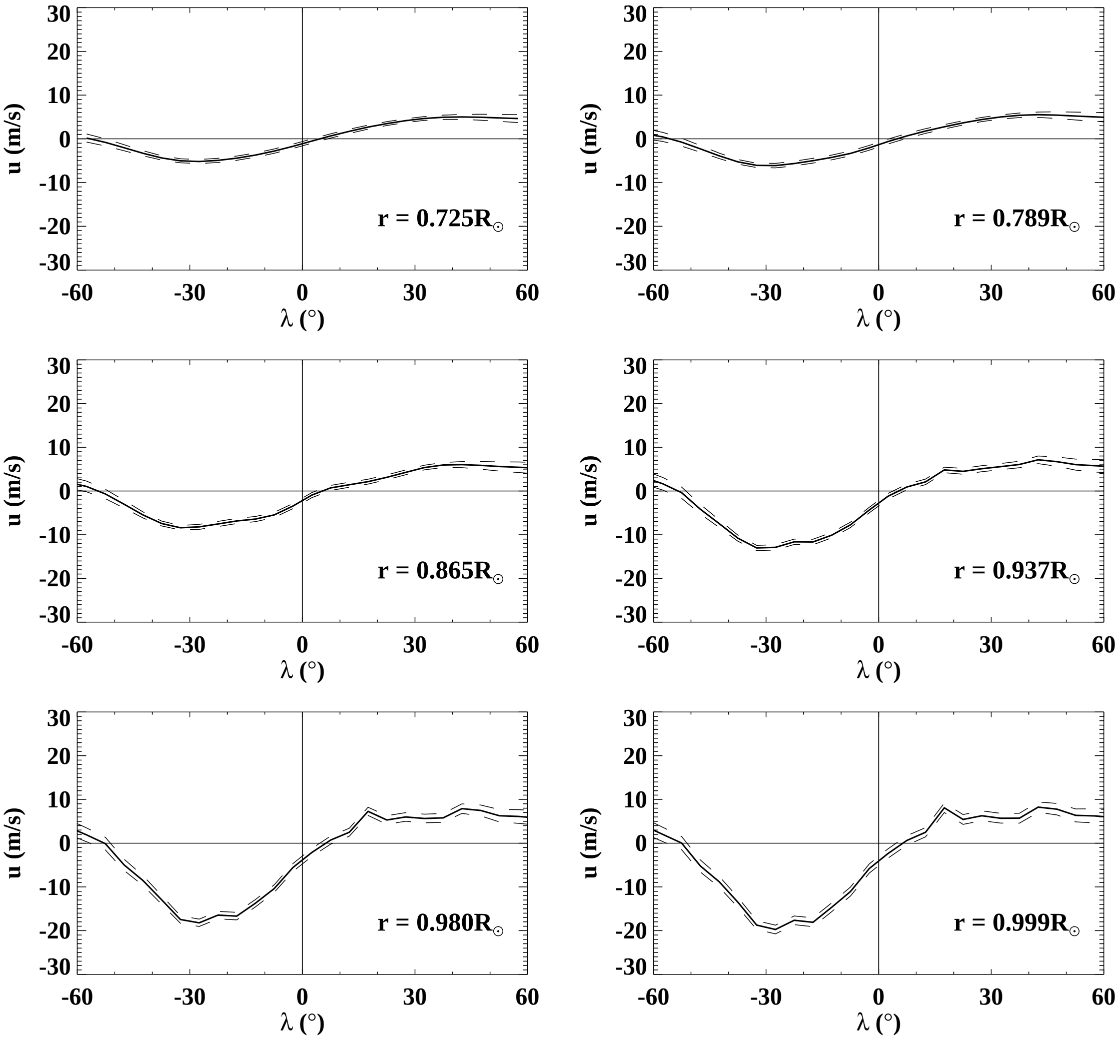

Figure 6.18: The meridional circulation inversion results, as a function of latitude λ, for six different depths. Positive velocities are northward.

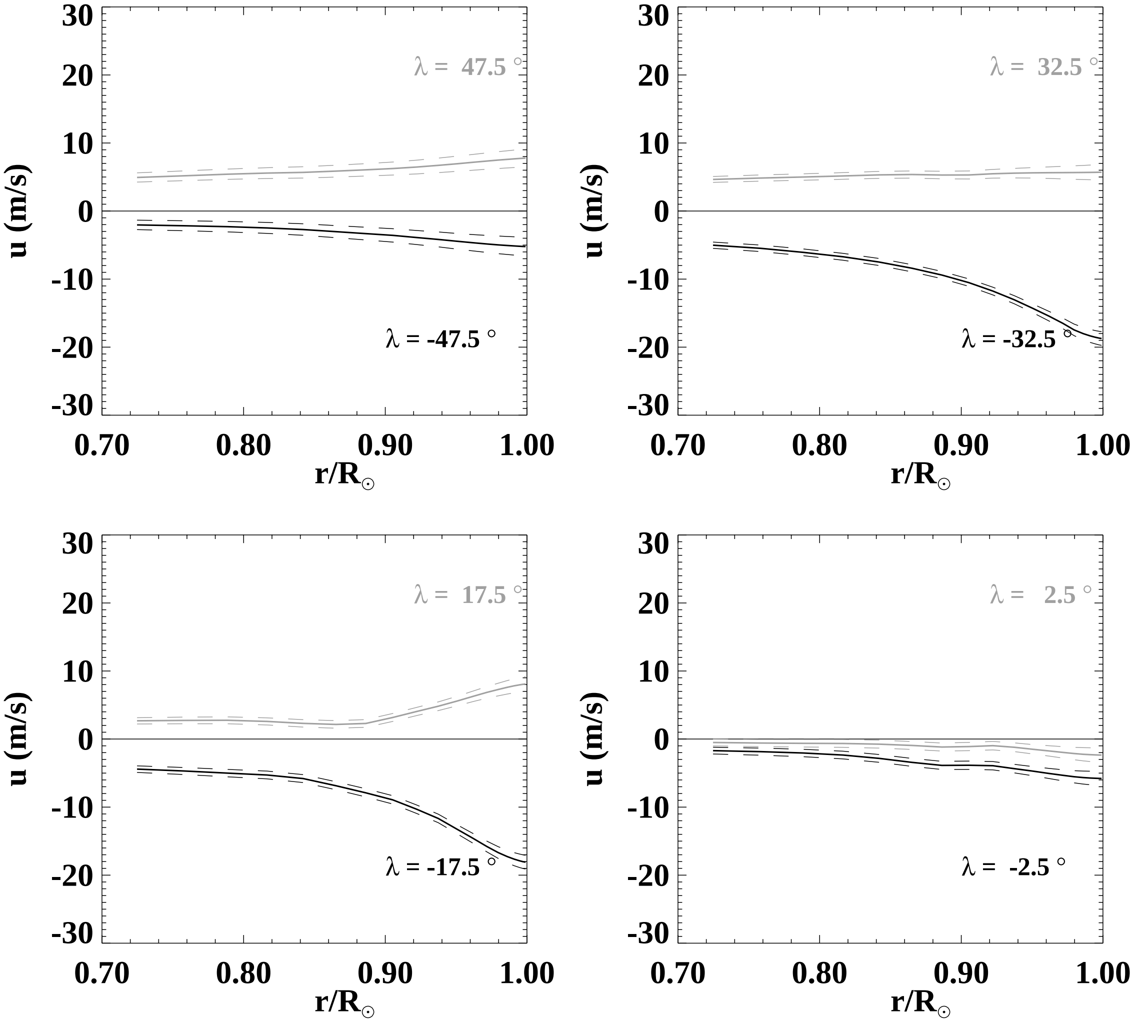

Figure 6.19: The meridional circulation inversion results, as a function of depth, for eight different latitudes. The dark curves, which are generally negative (southward) are for latitudes in the southern hemisphere; the lighter curves are for the corresponding latitudes in the northern hemisphere.

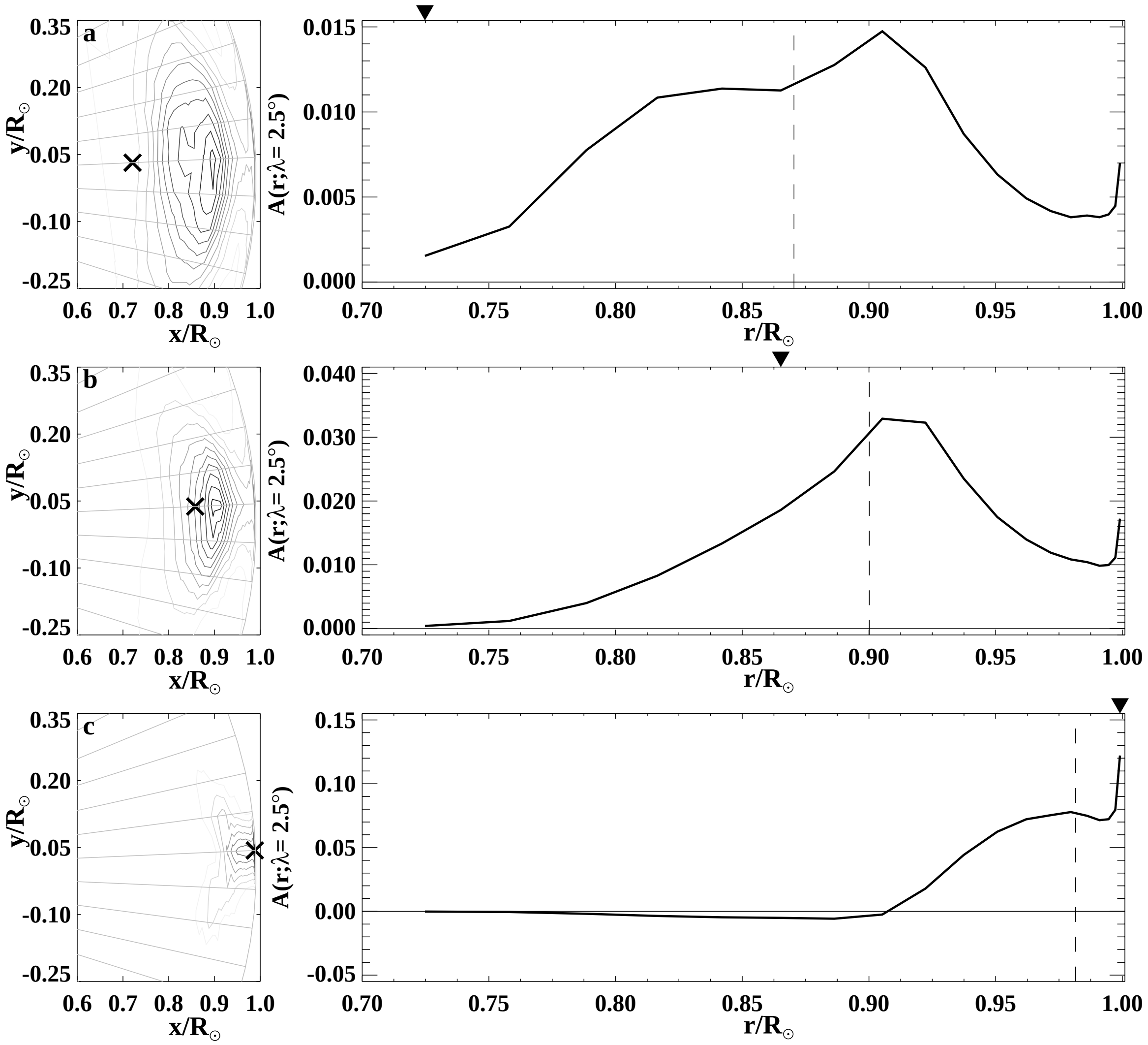

Figure 6.20: Some of the averaging kernels for the inversion results shown in figures 6.18 and 6.19. The plots in the left-hand column are contour plots of three selected averaging kernels. The contour spacing is 5% of the maximum amplitude of each kernel; dashed contours indicate a negative amplitude. The nominal locations of the three kernels, in each case marked with ×, are: (a) $r = 0.72\,\mathrm{R}_\odot, \lambda = 2.5°$; (b) $r = 0.87\,\mathrm{R}_\odot, \lambda = 2.5°$; and (c) $r = \mathrm{R}_\odot, \lambda = 2.5°$. In the right-hand column, a cross section of each kernel is plotted, as a function of radius, at the central latitude. The arrow above each plot marks the nominal radius of the kernel; the dashed line marks the location of the centroid.

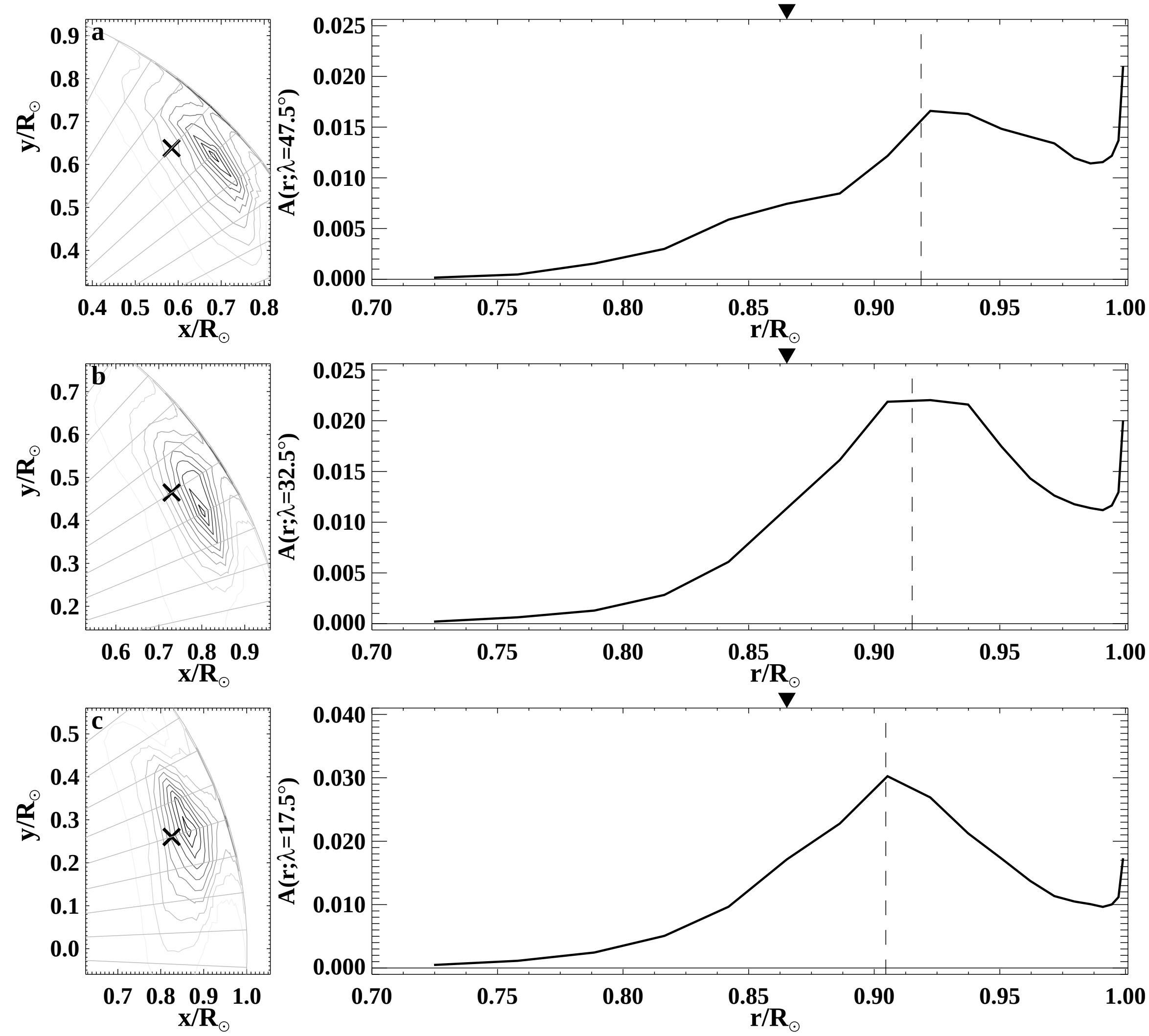

Figure 6.21: Some of the averaging kernels for the inversion results shown in figures 6.18 and 6.19. The symbols and contours are the same as for figure 6.20. In this case, the kernels all have the same nominal radius $r = 0.87\,\mathrm{R}_\odot$, but different latitudes: (a) $\lambda = 47.5°$; (b) $\lambda = 32.5°$; and (c) $\lambda = 17.5°$. Note for comparison that the nominal radius is also the same as in figure 6.20(b).

that the inversion results near the bottom of the convection zone actually contain information which spans a very wide range in radius; in fact, the averaging kernel in figure 6.20(a) has a very small amplitude at its nominal location of $r = 0.72\,\mathrm{R}_\odot$.

As explained in section 5.3, it is possible to constrain the inversion so that the solution must obey conservation of mass. When this constraint is added to the problem, new solutions can be generated which conserve mass and still satisfy the time-distance measurements. The "best" solution, in terms of the regularization condition, which satisfies the mass constraint is shown in figures 6.22 and 6.23. The turning point is at roughly $r = 0.80\mathrm{R}_\odot$; the amplitude of the equatorward flow at the base of the convection zone is about 3 m/s.

It is somewhat disheartening to admit that the circulation shown in figures 6.18 and 6.19 (which I will refer to as model A) and the one shown in figures 6.22 and 6.23 (model B) fit the measurements equally well. This is essentially due to the low sensitivity at the base of the convection zone, and the large errors on the measurements at large distances. For a ray with $\Delta = 45°$, the travel time difference in the two models differs by $|\delta\tau_A - \delta\tau_B| \simeq 0.1\,\mathrm{s}$. Since this is small compared to the measurement errors, the data cannot select one model in favour of the other. In the case of model B, the data for shorter distances is used to constrain the velocity in the near-surface layers, and the requirement that mass be conserved then dictates the circulation in the deepest layers.

Nevertheless, we might call model B the "best physical solution" which is consistent with the measurements. In addition, the combination of the 3 m/s equatorward flow and the $0.80\mathrm{R}_\odot$ turnover point are jointly constrained. For example, an increase in the flow amplitude would have to be matched by a lowering of the turnover, since the flow velocity in the upper layers is well-constrained by the data. It should also be noted that the models obtained with different regularization matrices H (equation 5.14) give qualitatively similar solutions.

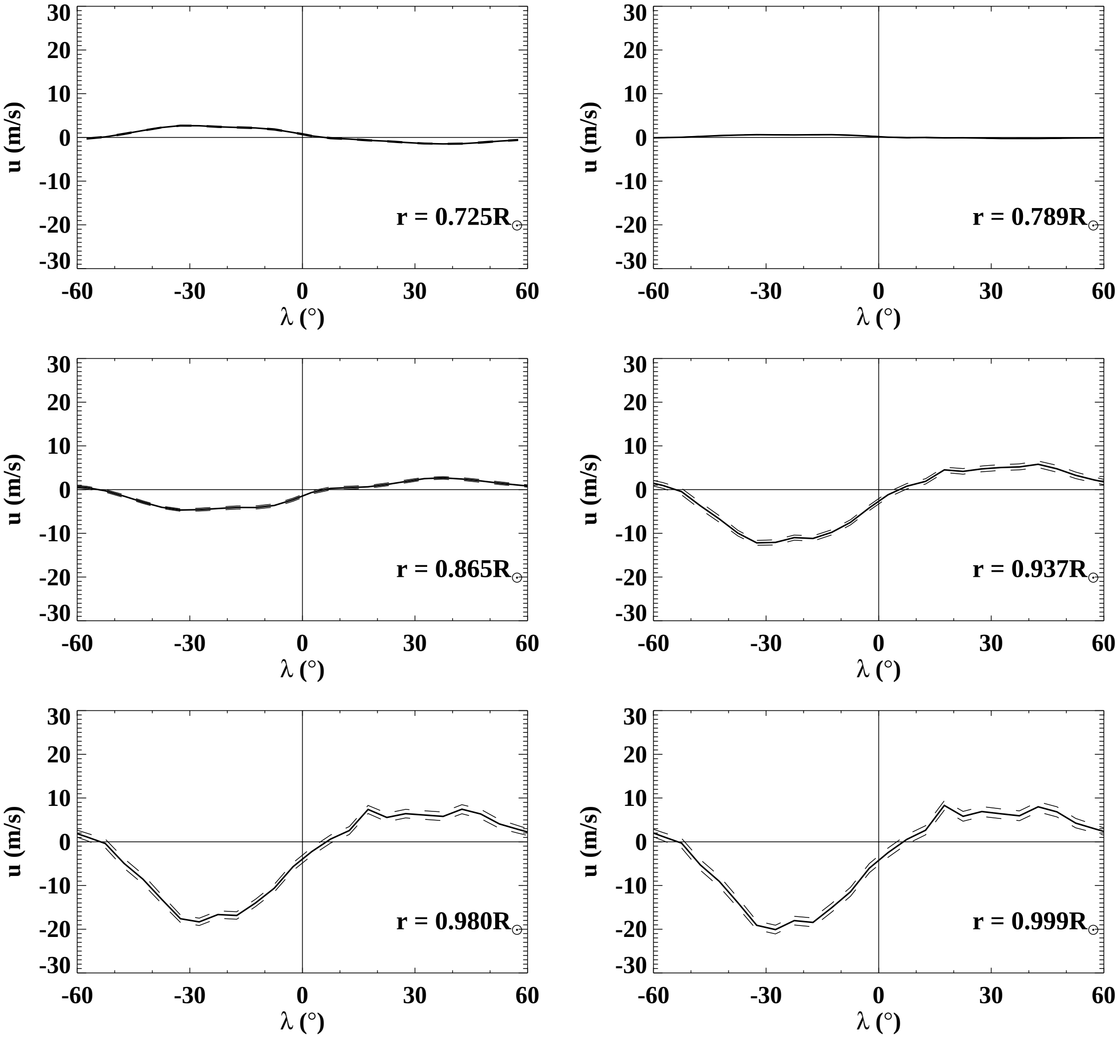

Figure 6.22: The meridional circulation inversion results, as a function of latitude λ, for six different depths. In this case, the model was constrained such that the total amount of mass moving northward is balanced by an equal amount moving southward, assuming that the velocity is zero below $0.71\,\mathrm{R}_\odot$. Positive velocities are northward.

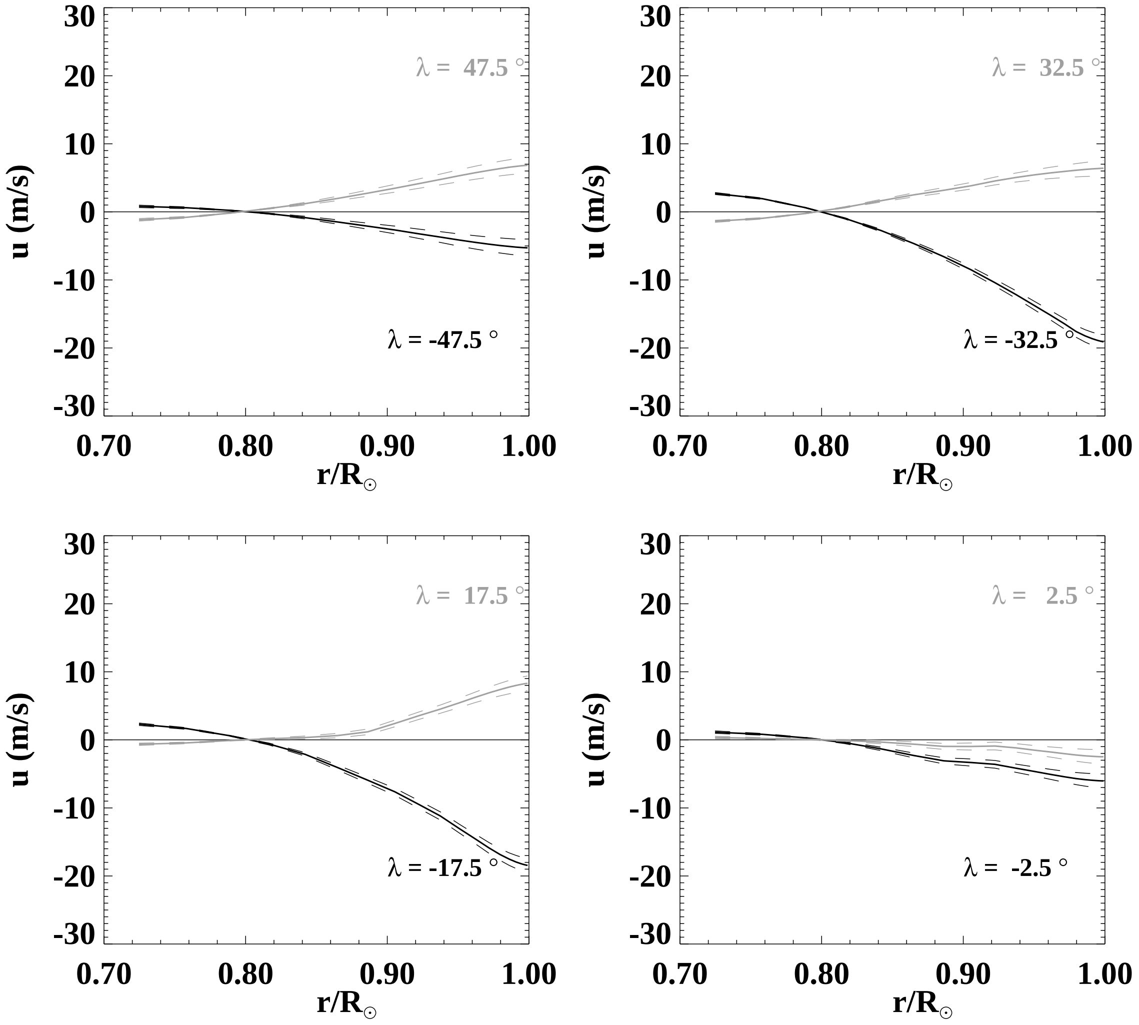

Figure 6.23: The meridional circulation inversion results for the mass-constrained case (see also figure 6.22), as a function of depth, for eight different latitudes. The dark curves, which are generally negative (southward) are for latitudes in the southern hemisphere; the lighter curves are for the corresponding latitudes in the northern hemisphere.

6.2.3 Behaviour of the equator-crossing flow

In section 4.7.1 it was pointed out that the equator-crossing (southward) meridional circulation observed with MDI may be due to an error in the orientation of the MDI image. Since the equatorial angular velocity in the convection zone is roughly independent of radius, this would result in an equator-crossing flow which was proportional to r. Figure 6.18 shows that the observed velocity is consistent with this hypothesis; however, section 6.2.2 demonstrates that quite different profiles are also consistent with the data. For the moment, it is only fair to say that the issue of the equator-crossing flow is still unresolved.

6.2.4 Time variation of meridional circulation

Since the two year observing run allows for time-resolved observations of the meridional circulation, it is interesting to examine the variation of the flow with the solar cycle. Previous observations (Komm et al., 1993b; Hathaway, 1996; Meunier, 1999) have indicated that the poleward flow observed at the surface has a smaller amplitude at solar maximum than at solar minimum.

The measurements made during the three Dynamics periods certainly show an interesting change between 1997 and 1998. Figure 6.24 shows these three sets of measurements, averaged over distance and plotted as a function of latitude. The magnetic activity was low in 1996 and 1997, but increased substantially in 1998. The amplitudes and shapes of the time difference curves are quite different; and, perhaps most interesting of all, there are hints that there is an equatorward flow in 1998 which originates near the pole and converges with the poleward flow at about 60°. The appearance of this type of two-cell pattern may be an important part of the solar cycle.

The differences in the measurements shown in figure 6.24 also appear in the inversions for meridional velocity. Figure 6.25 shows the surface velocity for these three time periods. The velocity in the inversions does not vary with depth down to $r = 0.96\,\mathrm{R}_\odot$. It would be interesting to look beyond this depth; unfortunately, considerations related to image geometry make the Structure images rather useless at

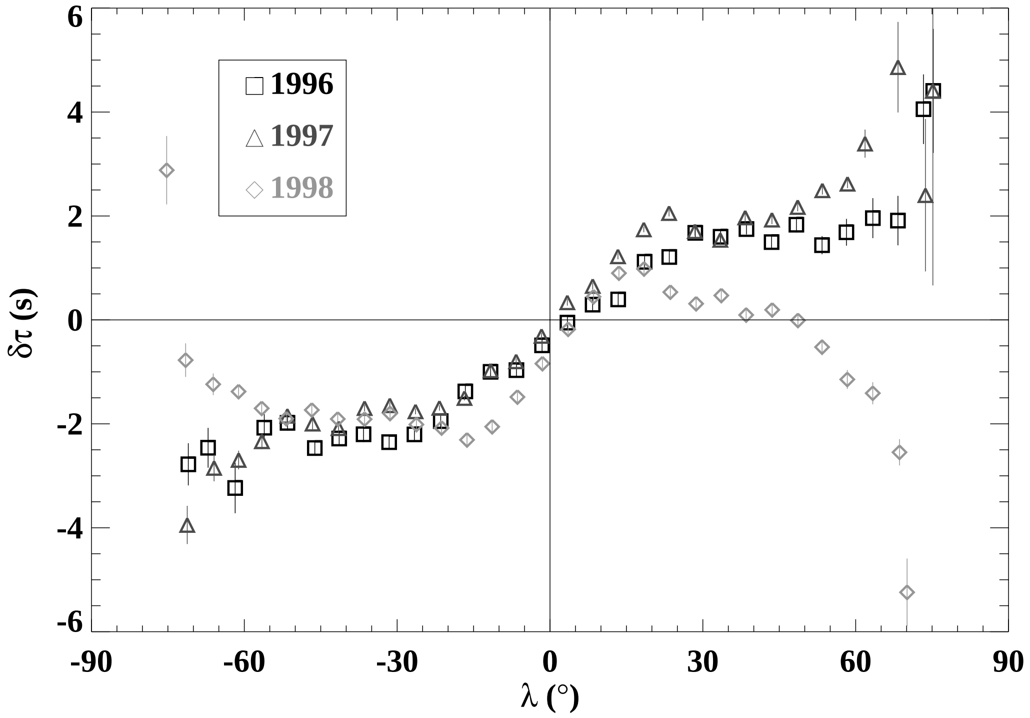

Figure 6.24: The south-north time differences as a function of latitude (see also figure 4.11) are plotted for three different Dynamics periods. These measurements were averaged in distance over a range ($1^\circ \leq \Delta \leq 6^\circ$). The sense of the time difference is south − north, so that a positive time difference indicates a northward flow. For reference, a time difference $\delta\tau = 1\,\mathrm{s}$ indicates a flow of about $10\,\mathrm{m/s}$; a distance of $\Delta = 6^\circ$ corresponds to an inner turning point at $r = 0.963\,\mathrm{R}_\odot$.

high latitude. The depth dependence of this possible two-cell pattern will probably remain unresolved until observations can be made from a position out of the ecliptic plane.

A final comment should be made about the equator-crossing flow. Figure 6.25 shows a time variation in this flow, with a larger amplitude in 1998 than in 1997 or 1996. However, most of this variation can be accounted for by an error in the Carrington elements. This is discussed further in appendix A.

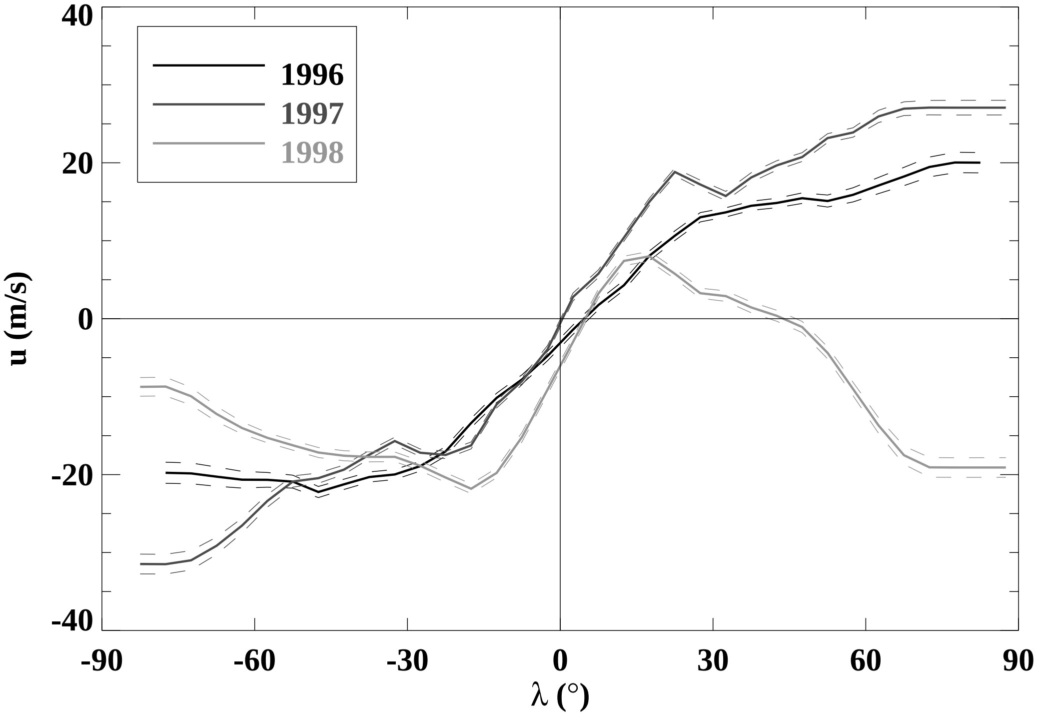

Figure 6.25: The inversion results for the three Dynamics periods. The velocity u is plotted as a function of latitude, for radius $r = \mathrm{R}_\odot$. The inversion resuts do not show any significant depth dependence for the region covered by these rays (down to $r = 0.96\,\mathrm{R}_\odot$).

Chapter 7

Discussion and Conclusions

The time-distance measurements and inversion results presented in the previous two chapters give us new insight into the Sun's behaviour. First, these measurements will allow a more complete model of the Sun's angular momentum. Furthermore, the flows probably play an important role in the Sun's magnetic cycle. I will deal with both of these areas briefly, and finish with a few comments about future directions in this field.

7.1 Angular Momentum Transport

7.1.1 Maintaining differential rotation

The angular momentum density of the Sun is very high at the equator compared to the poles — even higher than it would be if the Sun rotated as a solid body. Since viscous forces should act to dissipate such an imbalance, there must be an active source of driving for the differential rotation. This driving force must act to accelerate the equatorial regions relative to the polar regions.

The interaction between the rotation, the meridional circulation, and large-scale convection is a complex one, best treated by numerical simulations. Research by Gilman and his collaborators (Gilman, 1972; Gilman and Miller, 1986) has shed considerable light on the role played by the meridional circulation. Their models predict exactly the type of meridional circulation which is described in chapter 6: a dominant single-cell pattern in each hemisphere, poleward at the surface and equatorward at the bottom of the convection zone. By considering the Coriolis forces which arise from such a circulation, Gilman has noted that the meridional circulation always acts to reduce the differential rotation. This effect is dominated, however, by the influence of large-scale convection. Correlations of longitudinal and latitudinal motions give rise to Reynolds stresses which transport angular momentum from the poles towards the equator, thus driving the differential rotation.

The observations presented here qualitatively support Gilman's convection models, and may serve as an additional constraint on the model parameters. Even though the role of the meridional circulation in maintaining the differential rotation is small, the magnitude of the flow itself is determined by the characteristics of the convection. It will be interesting to see if the convection simulations can also be brought into quantitative agreement with the observations.

Another interesting feature of these observations is the solar-cycle variation in the observed flows. At high latitudes, the meridional circulation (section 6.2.4) and the rotation (section 6.1.5) both show a significant change as solar activity increases. The polar regions show a slower rotation, so that the differential rotation is more pronounced. At the same time, the poleward meridional flow at the surface disappears and possibly reverses. This behaviour is consistent with the idea that the poleward meridional circulation acts to destroy the differential rotation. The underlying cause of this change, however, is unknown.

7.1.2 Asymmetry in flow patterns

The two-year observations indicate that the large-scale solar differential rotation is essentially symmetric about the equator[1]. On smaller scales, however, the observations do show significant differences between the northern and southern hemispheres.

---

[1] Uncertainty in the direction of the solar rotation axis can lead to an *apparent* asymmetry in the angular velocity, as shown in appendix A.

One such feature was present throughout the entire two years of observation (section 6.1.3).

Very localized "jets" are not unheard of in dynamical models of the Sun, and indeed some similar features have been observed in inversions of global mode frequency splittings (Schou et al., 1998). However, this is the first time that an asymmetric feature of this type has been identified. It would perhaps be interesting to look at this region in more detail over a longer time period, and to optimize the resolution of the inversions in this area.

Finally, the observed north-south asymmetry in the solar meridional circulation is still unresolved. It is now my belief that the mean cross-equator flow is likely due to an instrumental effect as described in section 4.7.1. However, there is no *a priori* reason to believe that the meridional circulation must be always zero at the equator. The measurements have been presented as if the MDI camera was perfectly aligned with the spacecraft. Any subsequent information to the contrary can be used to correct the results.

7.2 The Solar Cycle

In addition to transporting mass and angular momentum, the measured meridional circulation must also transport magnetic fields from one latitude to another. It has long been believed that the solar differential rotation plays a critical role in the solar cycle; more recent models have also examined the possible role of the meridional circulation. In this section I will briefly describe and discuss these models in light of the measurements in this work.

7.2.1 Babcock-Leighton dynamo theories

During the 1960s, Babcock (1961) and Leighton (1964; 1969) described for the first time a coherent picture of the solar magnetic cycle using newly available measurements of the Sun's magnetic fields and surface motions. Although their models predated helioseismology, this work is still used as the foundation for much of our current understanding of the solar cycle. The model has come to be known as a *Babcock-Leighton* or $\alpha - \Omega$ dynamo model.

Conceptually, the Babcock-Leighton model begins with a subsurface poloidal (meridional) magnetic field. Since the Sun rotates differentially, a poloidal field line will become "wound up" by the rotating plasma until an amplified toroidal field has been produced. This is the so-called Ω-effect.

This toroidal field erupts at the surface in the form of bipolar magnetic regions (meant to represent sunspots). These magnetic regions are assumed to erupt with their "leading" (*i.e.* in the direction of rotation) poles located equatorward of their "trailing" poles; in this way, the poloidal component of the bipolar region is opposite that of the original poloidal field in that hemisphere. The α-effect is the name given to the mechanism which converts the toroidal field to poloidal field; different models account for this effect through slightly different mechanisms.

Once the bipolar regions have reached the surface, supergranular convection gives rise to an effective diffusion, which results in a net transport of trailing-polarity flux towards the poles. As more trailing-polarity flux moves to the poles, the polar fields are eventually reversed. This is in agreement with the butterfly diagram of the solar cycle, where the polar fields change sign each half-cycle.

The butterfly diagram gets its name from another obvious pattern in the field structure: as each half-cycle progresses, the sunspots appear at lower and lower latitudes. Numerically, Leighton found that in order to create stable oscillations of this type, his model required a radial gradient in the angular velocity. Furthermore, the observed equatorward migration of the magnetic eruptions could only be explained by a rotation rate which increases inward. As noted above, this work predated the birth of helioseismology as a diagnostic tool; it is now well known that the radial gradient in the angular velocity is rather small in the convection zone, except perhaps near the solar surface. There *are* strong gradients in the rotation rate at the base of the convection zone, but at low latitudes the rate is decreasing inward.

In addition, the original work by Babcock and Leighton did not include any meridional circulation. More recently, new models have been created which include meridional circulation, particularly Wang *et al.*(1991), Choudhuri *et al.*(1995), and Dikpati

& Charbonneau (1999). I will focus on the model by Wang *et al.* as representative of this class of models, in order to discuss some of the implications of the measurements I have made in this work.

7.2.2 Implications for the Wang *et al.* model

The meridional circulation plays two important roles in the dynamo model of Wang *et al.* First, the poleward meridional circulation at the surface helps to carry the flux from decaying trailing-polarity sunspots towards the poles. In earlier models, this poleward migration (and thus, ultimately, the polar field reversal) was accomplished by diffusion alone. Adding a meridional circulation therefore allows for smaller values of the supergranular diffusion. Second, the model postulates an equatorward return flow at the base of the convection zone. This flow is responsible for the "butterfly" migration of sunspots during the solar cycle, eliminating the need for an angular velocity profile which increases inward.

The stability and period of the dynamo created with this model depend quite sensitively on the magnitude of the equatorward return flow. Wang *et al.* observed that a change in this velocity of as little as 25% could make the dynamo oscillations unstable[2]. The authors present a "best" model with a return velocity of 1.3 m/s. The observations presented in chapter 6 indicate that the velocity is somewhat higher; however, it is obvious that the current measurements cannot constrain the velocity enough to distinguish between competing dynamo models.

The poleward surface velocity, on the other hand, is now quite strongly constrained by these measurements and others from helioseismology. Many dynamos use a peak value of $\simeq 10\,\mathrm{m/s}$, which is significantly lower than has been observed. In addition, there is preliminary evidence that the circulation profile changes significantly during the solar cycle. The results presented in section 6.2.4 about the possible appearance of a second, equatorward, circulation cell during the rising phase of the cycle are

---

[2] Charbonneau and Dikpati also found that the dynamo characteristics depended very sensitively on the value of the return velocity.

especially intriguing. In the dynamo models mentioned above, the meridional circulation is not allowed to vary with time; further observations will be important for establishing the pattern for an entire cycle.

7.2.3 Suppression of magnetic buoyancy

Another aspect of the solar magnetic dynamo which can be affected by the size and shape of the meridional circulation is the physical location of the strong toroidal field. Parker (1975) pointed out that magnetic buoyancy acting on flux tubes in the convection zone would cause them to rise to the surface very quickly. A flux tube with a field strength of 100 gauss would rise too quickly to be significantly amplified, and thus Parker concluded that the amplification process must take place at the very bottom of or just below the convection zone.

Another possible solution to the problem was suggested by van Ballegooijen (1982) and later expanded upon by van Ballegooijen and Choudhuri (1988). The basic premise is that an equatorward meridional circulation in the lower part of the convection zone can act to counteract the effects of magnetic buoyancy through drag on the flux tube. For a toroidal loop, the magnetic tension and the Coriolis force act to pull the tube toward the rotation axis; the magnetic buoyancy acts to pull the loop radially toward the surface, and the meridional circulation can cause a drag force which acts to pull the loop toward the equatorial plane in the horizontal direction.

The authors found that, under certain conditions, flux tubes of considerable strength can be stable to small perturbations in position in the lower part of the convection zone. Specifically, the tube can be stable in regions where the meridional flow is equatorward and increasing outward. The measurements of chapter 6 do not indicate any such regions, but of course this is not ruled out by the observations.

7.3 Conclusions

7.3.1 Summary of results

The measurements presented in the previous chapters show that the technique of time-distance helioseismology can be used to measure solar flows on global scales. In addition to the development of this method, this dissertation contains several important new results.

First, the meridional flow has been measured below the solar surface. The results presented here are an expansion of previous work (Giles et al., 1997; Giles and Duvall, 1998; Giles et al., 1998) which measured the subsurface circulation for the first time. In this work, the measurements have been extended to the base of the convection zone. In chapter 6 it was shown that the measurements are consistent with the presence of a single circulation cell in each hemisphere, with a poleward flow at the surface of 20 m/s and an equatorward velocity of 3 m/s at the base of the convection zone. The turning point for the circulation is at $0.80 R_\odot$. These last two quantities are not very tightly constrained by the measurements; however, their combination is constrained by considerations of conservation of mass.

Second, the solar rotation has been measured for each hemisphere independently. In addition to demonstrating the success of the time-distance method, these measurements indicate evidence of a localized, strongly asymmetric feature in the rotation. The feature is a region near 40° latitude and $0.92\,R_\odot$ which exhibits a faster rotation rate in the southern hemisphere than in the northern. The difference in zonal velocity may be as much as 200 m/s, which corresponds to 14% of the symmetric component of the velocity. The spatial extent of the asymmetry is uncertain, since it may be smaller than the wavelength of the acoustic waves used in the measurements.

Third, the near-surface rotation and meridional circulation appear to show significant time variation during the rising phase of the solar cycle. The measurements span somewhat more than two years of observations, beginning at solar minimum in the early summer of 1996. The solar rotation appears to decrease in the polar regions as activity increases; the meridional circulation also decreases and perhaps even reverses to become an equatorward flow. It will be interesting to see if these patterns continue in the MDI data from 1999 and beyond.

Fourth, the time variations of the measurements show some effects which are probably related to our uncertainty in the Carrington elements which describe the Sun's rotation axis. The measurements presented in Appendix A show that the inclination of this axis with respect to the ecliptic plane (denoted by i) is less then Carrington (1863) proposed; in this work I suggest a new value of $i = 7.15°$.

7.3.2 Future work[3]

The study of solar flows has been an area of active study for as long as there have been solar astronomers. No doubt this will continue into the foreseeable future. The tools of helioseismology have proven to be extremely valuable in this search, and the time-distance technique developed by Duvall and others has already proven to be a worthy addition.

A precise determination of the meridional circulation at the base of the convection would be a significant observational constraint on solar dynamo theories. The measurements presented here show that the time-distance technique can be used to determine the large-scale meridional velocities. The current precision is not yet enough to discriminate between competing theories, but already at least two important facts have been established. First, the observations clearly show that the meridional circulation is a global phenomenon, and not just confined to the surface. Since a velocity of 1 m/s has been shown in some models to have important effects on the dynamo oscillations, models which ignore the meridional circulation are probably incomplete. Second, the magnitude of the poleward flow near the surface is now very well constrained by several methods in helioseismology. This surface flow may play an important role in the polar field reversal of the magnetic cycle.

In terms of improvement to this work, I believe that the interpretation of time-distance measurements will be an area of increased focus over the next few years.

---

[3] If any researchers are interested in the measurements used in this work, Appendix B contains a table of the datasets which have been created during this research project, along with a brief explanation of how they can be retrieved from the archives at Stanford. These might be especially interesting to those who would offer an improved interpretation of the measurements.

Thus far most workers in the field have concentrated — as I have, in this dissertation — on making new and interesting measurements. Most of these measurements have been interpreted within the framework of the ray approximation. Although I believe this method to be quite adequate for the scope of the current work, I also expect that more general techniques will be developed in the near future.

Furthermore, the MDI instrument is, as of this writing, still in good working order. In fact, more than eight months' worth of Dopplergrams have been taken since the last image used for this work. This is especially intriguing given the changes seen in the 1998 Dynamics period.

Finally, some day it will be possible to make similar obervations from other spacecraft. Perhaps some will travel out of the ecliptic plane and allow a view over one of the solar poles. Some may allow measurements for very long travel distances by coordinating multiple platforms. Over the course of this research project, much has been learned about efficient and effective processing of MDI images for time-distance helioseismology, and these lessons should be put to good use in the future.

Appendix A

On The Rotation Axis of the Sun

In interpreting measurements of solar velocities, it is crucial to know the direction of the Sun's axis of rotation for each observation. The "known" axis of solar rotation that is used almost universally today was determined almost 150 years ago (Carrington, 1863) by observing the motions of sunspots recorded on photographic plates at a ground-based observatory[1]. Although Carrington did not offer an estimate of the uncertainty in his proposed standard, it seems unlikely that the error was less than about a tenth of a degree. Subsequent researchers have attempted to improve on the accuracy of this measurement, with varying results. This appendix presents a new measurement which may offer the most accurate determination yet, and compares the results with those obtained by other researchers in the last one hundred years. Finally, it is proposed that the set of more modern measurements be used to adopt a new standard for the Sun's axis of rotation.

---

[1] It is interesting to note that the observations required to make this calculation were available at least two hundred years earlier (see Eddy *et al.* (1976)

A.1 The Coordinate System: i and Ω

Consider the representation of the Sun in figure A.1[2]. The great circle ΥEN is the intersection of the plane of the ecliptic (the plane of the Earth's orbit) with the solar surface. The point C defines the center of the sphere, and CK is perpendicular to the ecliptic. The point Υ is defined such that a straight line drawn from C to Υ points in the direction of the vernal equinox; this is the reference direction from which celestial longitudes are measured. The line joining C and the Earth cuts the sphere at E, and the plane defined by CK and CT, perpendicular to CE, is defined as the plane of the disk. The heliocentric ecliptic longitude of the Earth is ΥE; the geocentric longitude of the Sun is denoted by $\eta = \Upsilon E + 180°$.

The Sun rotates around an axis CP, where P is the north pole of the Sun. The great circle perpendicular to this axis is the solar equator, of which the arc NJ is a section. The inclination of the solar equator to the ecliptic (the angle JNE in figure A.1) is denoted by i. The point N is the ascending node of the solar equator on the ecliptic plane, and its longitude ΥN is given the symbol Ω. The values of i and Ω completely determine the Sun's rotation axis. The standard values used by the astronomical community are those determined by Carrington (1863), namely

$$\begin{aligned} i_c &= 7.25°, \\ \Omega_c &= 73.67° + 0.013958°(t - 1850.0), \end{aligned} \tag{A.1}$$

where t is expressed in years. The value of Ω increases slowly due to precession.

The point E will be seen as the center of the disk; the latitude of this point must be known in order to correctly interpret the measured velocities. This latitude is denoted by B_0. For the spherical triangle defined by PEN,

---

[2] The notation and description in this section borrow heavily from Smart (1977). It is included here so that the reader need not make reference to that work.

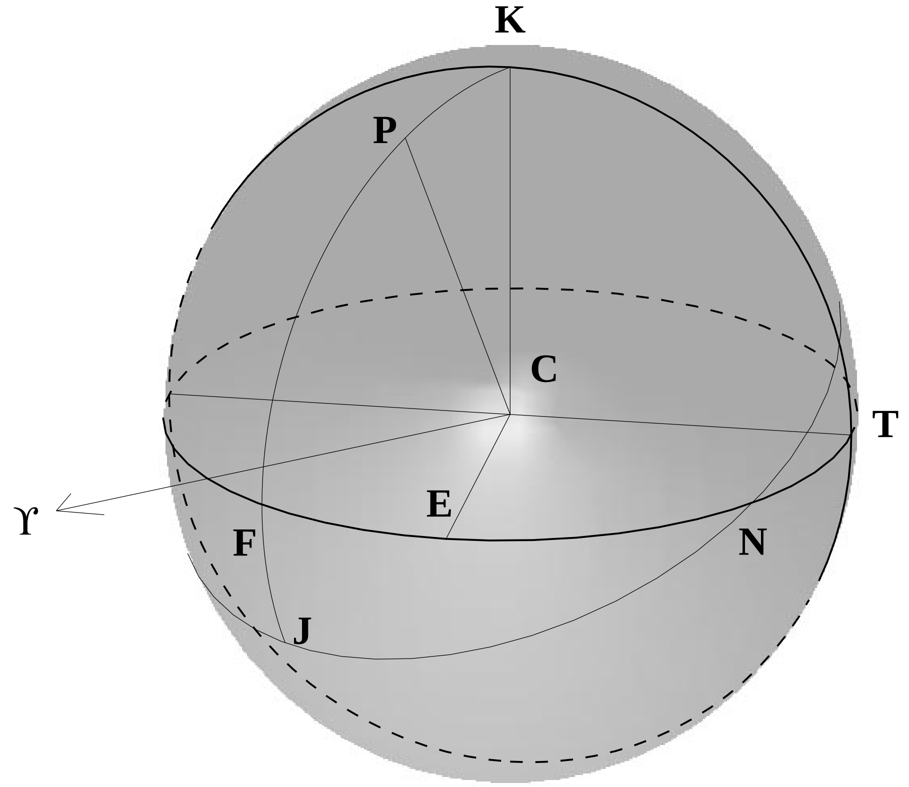

Figure A.1: The geometry of the coordinate system used in measuring solar positions. The line CP represents the rotation axis of the Sun; the axis CK is the pole of the ecliptic. The inclination (angle KCP) is exaggerated. Other symbols are explained in the text.

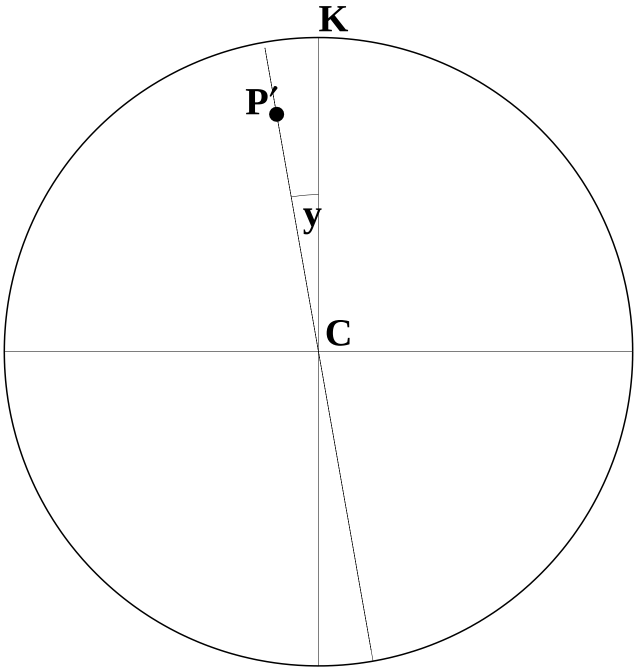

Figure A.2: The angle denoted by y is the *effective position angle* of the solar image taken by MDI. The point P' is the projection of the north pole of the Sun into the plane of the image.

$$\begin{aligned} PN &= 90^\circ, \\ PE &= 90^\circ - B_0, \\ EN &= \Omega - \eta - 180^\circ, \\ \angle PNE &= 90^\circ - i. \end{aligned} \tag{A.2}$$

Using the cosine law for spherical triangles (see e.g. Smart (1977)), the angle B_0 can thus be computed from the rotation elements:

$$\sin B_0 = sin(\eta - \Omega) \sin i \tag{A.3}$$

Now consider the angle made by the projection of the rotation axis CP onto the plane of the disk, and the pole of the ecliptic CK. Let us denote this angle[3] by y (see figure A.2). The axes CE, CT, and CK define a rectangular coordinate system, and the coordinates of P are given by $(\sin KP \cos EF, \sin KP \sin EF, \cos KP)$. Hence the projection of P onto the CT-CK plane has coordinates $(\sin KP \sin EF, \cos KP)$, and the angle y is given by $\tan y = \tan KP \sin EF$. The angle KP is the inclination i, and EF can be expressed in terms of Ω such that

$$\tan y = -\cos(\eta - \Omega) \tan i \tag{A.4}$$

Equations A.3 and A.4 thus define the coordinate system on the disk as seen from Earth.

A.2 SOHO Orbit and Alignment

The SOHO spacecraft orbits the Sun in a halo orbit about the Earth-Sun Lagrange point L_1. The spacecraft attitude is maintained (via star trackers) so that the MDI camera is aligned always with the Carrington rotation elements. More precisely, if the Sun's rotation axis is accurately described by the elements (i_c, Ω_c) of equation A.1, then SOHO is aligned such that the angle y described by equation A.4 will always be zero.

On the other hand, what if the Sun rotates about an axis described by coordinates (i, Ω) which are slightly different from the Carrington elements? Clearly this will mean that the position angle y and the heliographic latitude of disk center B_0 will be somewhat different from their expected values. To quantify these effects, suppose that the actual rotation elements of the Sun differ from the Carrington elements according to

---

[3] Note that y is *not* the position angle P of the rotation axis as it is usually defined.

$$\begin{aligned} i &= i_c + \Delta i, \\ \Omega &= \Omega_c + \Delta\Omega. \end{aligned} \tag{A.5}$$

Define the angle errors

$$\begin{aligned} E_P &\equiv y - y_c, \\ E_B &\equiv B_0 - B_{0c}. \end{aligned} \tag{A.6}$$

Here y_c is given by equation A.4, with i replaced by i_c and Ω replaced by Ω_c. The latitude B_{0c} is defined in the same way by equation A.3.

Using Taylor series expansions for the trigonometric functions, the equations A.3 and A.4 can be used to express y and B_0 in terms of the known values y_c and B_{0c} and the errors Δi and $\Delta\Omega$. The definitions A.6 can then be used to write

$$E_P \simeq \frac{-(\Delta\Omega \tan i_c \sin(\eta - \Omega_c) + \Delta i \sec^2 i_c \cos(\eta - \Omega_c))}{1 + \tan^2 i_c \cos^2(\eta - \Omega_c)} \tag{A.7}$$

$$E_B \simeq \frac{\Delta i \cos i_c \sin(\eta - \Omega_c) - \Delta\Omega \sin i_c \cos(\eta - \Omega_c)}{[1 - \sin^2 i_c \sin^2(\eta - \Omega_c)]^{1/2}} \tag{A.8}$$

Here all terms which are second-order or higher in Δi, $\Delta\Omega$, E_P, and E_B have been neglected, since all of these quantities can be assumed to be quite small. Furthermore, the quantity i_c is small enough that terms which are second-order in i_c can also be ignored; in this case equations A.7 and A.8 simplify to

$$E_P \simeq -(\Delta\Omega \tan i_c \sin(\eta - \Omega_c) + \Delta i \cos(\eta - \Omega_c)) \tag{A.9}$$

$$E_B \simeq \Delta i \cos i_c \sin(\eta - \Omega_c) - \Delta\Omega \sin i_c \cos(\eta - \Omega_c) \tag{A.10}$$

Hence it can be seen that the angle errors E_B and E_P will vary with a one-year period as SOHO orbits around the Sun. This fact provides the basis for the measurement of Δi and $\Delta\Omega$ outlined in the following section. It is worth noting that some other sources of these angle errors — for example, a fixed error in the alignment of MDI relative to the SOHO axis — do *not* show a similar dependence on orbital position.

A.3 Solar Velocities and Angle Errors

An error in the position angle or in the heliographic latitude of disk center will result in errors in the analysis of solar velocities. For example, if the position angle has a small error E_P, then the "meridional" velocity determined in the analysis will contain a component of the zonal velocity or rotation which leaks in:

$$v_{\theta,m}(\theta) = v_\theta(\theta) + v_\phi(\theta)\sin E_P \tag{A.11}$$

Here the subscript m denotes a measured velocity, whereas values without such notation are the true velocities in the θ and ϕ directions. For the rotation, the principal source of error will be a misidentification of the latitude of each position on the disk:

$$v_{\phi,m}(\theta) = v_\phi(\theta) - v'_\phi(\theta)E_B \tag{A.12}$$

where v'_ϕ is the derivative of the zonal velocity with respect to colatitude θ. The minus sign in equation A.12 arises because the error E_B is defined as a latitude error, while the derivative is made with respect to the colatitude.

Since the errors E_B and E_P which arise from an error in the Carrington elements vary during the orbit of SOHO, it should be possible to extract them from the measured velocities. For this purpose, a time series of velocities was constructed, with two average profiles $v_\theta(\theta)$ and $v_\phi(\theta)$ for each Carrington rotation. The total length of the time series was somewhat more than two years. For the first iteration of the procedure, the true rotation profile $v_\phi(\theta)$ was taken to be the mean of the measured profiles. A function of the form

$$v(\eta - \Omega_c) = a_0 + a_1\sin(\eta - \Omega_c) + a_2\cos(\eta - \Omega_c) \tag{A.13}$$

was then fit to each of $v_{\phi,m}$ and $v_{\theta,m}$ at each colatitude by a linear least-squares method. Combining equations A.11 and A.9, it was possible to determine

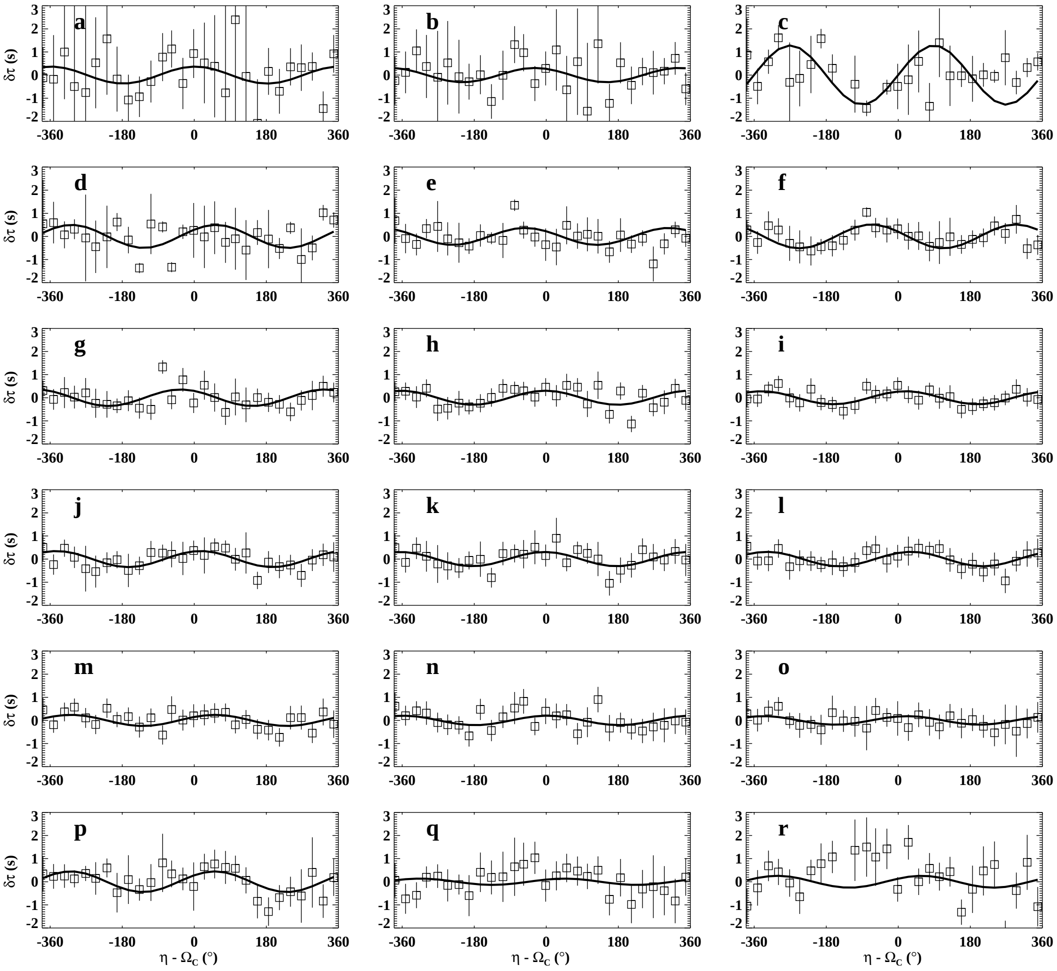

Figure A.3: The time variation of the meridional velocity is plotted for eighteen different latitudes. The horizontal axis denotes the coordinate $\eta - \Omega_c$, where η is the SOHO-centric longitude of the Sun, and Ω_c is defined in equation A.1. The vertical axis shows the difference $\delta\tau$ between the southward and northward travel times for travel distances of 3° to 10°. In each plot, the mean value of the velocity has been removed in order to emphasize the time variation. A positive time difference represents a meridional flow more northward than the mean. The squares represent the measured data points, where there is one point for each Carrington rotation. The solid curve is a function of the form given in equation A.13. The latitudes and fit parameters are summarized in table A.1.

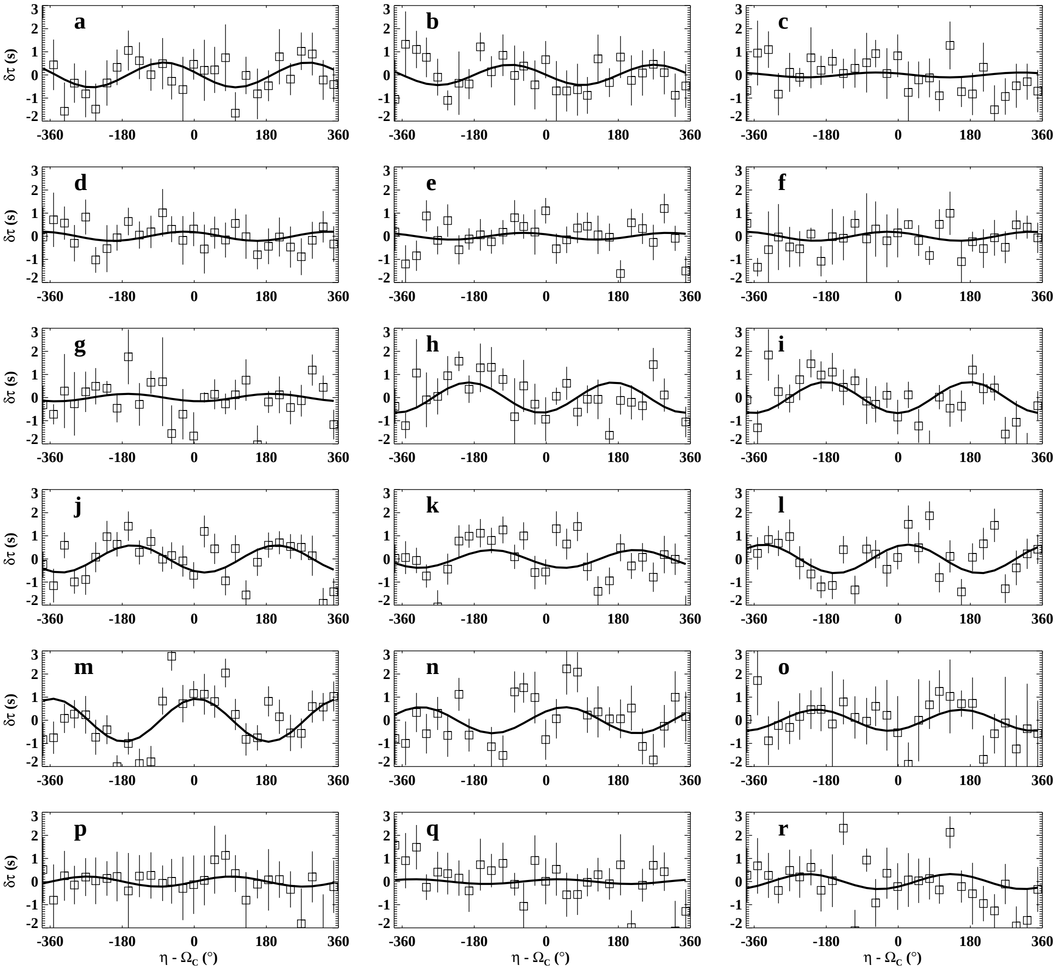

Figure A.4: The time variation of the rotation is plotted for eighteen different latitudes. The horizontal axis denotes the coordinate $\eta - \Omega_c$, where η is the SOHO-centric longitude of the Sun, and Ω_c is defined in equation A.1. The vertical axis shows the difference $\delta\tau$ between the eastward and westward travel times for travel distances of 3° to 10°. In each plot, the mean value of the velocity has been removed in order to emphasize the time variation. A positive time difference represents a rotation velocity which is faster than the mean. The squares represent the measured data points, where there is one point for each Carrington rotation. The solid curve is a function of the form given in equation A.13. The latitudes and fit parameters are summarized in table A.2.

$$\begin{aligned}\langle v_\theta \rangle &= a_0, \\ \Delta\Omega &= -\frac{a_1}{v_\phi \tan i_c}, \quad \text{and} \\ \Delta i &= -\frac{a_2}{v_\phi}\end{aligned} \tag{A.14}$$

from $v_{\theta,m}$ at each colatitude. Similarly, estimates for Δi and $\Delta\Omega$ can be made from the measurements of the zonal velocities:

$$\begin{aligned}\langle v_\phi \rangle &= a_0, \\ \Delta i &= -\frac{a_1}{v'_\phi \cos i_c}, \quad \text{and} \\ \Delta\Omega &= \frac{a_2}{v'_\phi \sin i_c}\end{aligned} \tag{A.15}$$

At every latitude, a time series of time differences was constructed with one point for each of 28 Carrington rotations. A function of the form of equation A.13 was fit to the time series using a weighted least squares technique. Figures A.3 and A.4 show the time series and fits. The measurement errors used in the fitting were calculated as described in section 4.5. The values of Δi and $\Delta\Omega$ were derived from the parameters of the least-squares fit, along with uncertainties; these values are given in tables A.1 and A.2.

From the measurements of the meridional flow, the mean values of these quantities were $\Delta i = -(0.091 \pm 0.012)^\circ$, and $\Delta\Omega = -(0.18 \pm 0.10)^\circ$. Slightly different values were obtained from the rotation meaurements: $\Delta i = -(0.105 \pm 0.033)^\circ$ and $\Delta\Omega = (0.16 \pm 0.27)^\circ$. Thus the two measurements agree with one another within their uncertainties; however, it there are clearly some systematic errors in the measurements derived from the zonal velocity. Table A.2 shows that the values for both Δi and $\Delta\Omega$ show a sytematic dependence on latitude, being especially large in magnitude near the equator. The plots in figure A.5 show that while the measurements made using meridional flows are normally distributed about their mean values, the measurements made from zonal flows are widely (and not randomly) scattered. The most extreme

Fig.	λ (°)	χ^2	$\Delta i(°)$	$\Delta\Omega(°)$
a	-42.5	0.5	-0.190±0.157	-0.052±1.831
b	-37.4	0.5	-0.127±0.107	0.545±1.132
c	-32.6	6.2	-0.005±0.061	-4.385±0.617
d	-27.4	3.4	-0.119±0.049	-1.282±0.498
e	-22.5	1.3	-0.085±0.047	0.885±0.410
f	-17.7	0.8	-0.075±0.044	1.377±0.394
g	-12.7	1.0	-0.107±0.042	0.571±0.386
h	-7.5	0.9	-0.108±0.037	0.038±0.325
i	-2.4	0.5	-0.094±0.033	-0.238±0.279
j	2.4	0.5	-0.118±0.044	-0.257±0.354
k	7.5	0.5	-0.109±0.049	0.065±0.374
l	12.7	0.4	-0.096±0.044	-0.471±0.349
m	17.7	0.6	-0.055±0.042	-0.549±0.342
n	22.5	0.6	-0.078±0.048	-0.024±0.420
o	27.4	0.2	-0.069±0.058	-0.223±0.478
p	32.6	0.5	-0.121±0.070	-1.194±0.564
q	37.4	0.5	-0.045±0.086	-0.357±0.758
r	42.5	1.8	-0.070±0.099	-0.889±0.923
Means			-0.091±0.012	-0.182±0.101

Table A.1: Determination of elements i and Ω from meridional velocity. Each row in the table corresponds to a plot in figure A.3. The quantities Δi and $\Delta\Omega$ were estimated from each plot independently as described in the text. The last row gives the mean values for Δi and $\Delta\Omega$, where each measurement has been appropriately weighted according to its uncertainty.

deviations from the mean values are for latitudes near the equator (plots h, i, j, k, l, and m of figure A.4 and table A.2. When these measurements are excluded from the mean, the values for Δi and $\Delta\Omega$ become (-0.112 ± 0.034) and (-0.28 ± 0.28), respectively. However, it is at least slightly dubious to suggest that there exists a systematic error which causes only these particular measurements to be incorrect. Until the source of this one-year oscillation in the zonal velocity is explained, it is probably safest to disregard the measurements from zonal velocities altogether.

Fig.	λ (°)	χ^2	Δi(°)	$\Delta\Omega$(°)
a	-42.5	0.9	-0.208±0.099	-0.404±0.732
b	-37.4	0.7	-0.208±0.102	0.002±0.846
c	-32.6	0.7	-0.043±0.108	-0.253±0.895
d	-27.4	0.5	-0.045±0.113	-0.816±0.885
e	-22.5	1.3	-0.088±0.125	-0.472±0.937
f	-17.7	1.3	-0.093±0.188	-1.454±1.104
g	-12.7	1.1	-0.060±0.279	1.918±1.763
h	-7.5	2.0	0.365±0.473	12.565±3.365
i	-2.4	1.5	0.145±1.036	29.495±7.802
j	2.4	1.6	1.612±1.010	-26.241±7.708
k	7.5	2.3	0.546±0.342	-4.524±2.564
l	12.7	1.6	-0.399±0.280	7.207±2.069
m	17.7	2.4	-0.101±0.206	8.330±1.477
n	22.5	1.6	-0.288±0.163	2.158±1.240
o	27.4	0.6	-0.101±0.159	-1.897±1.309
p	32.6	0.2	-0.112±0.132	-0.035±1.138
q	37.4	0.9	-0.024±0.096	0.328±0.893
r	42.5	1.7	-0.099±0.086	-0.724±0.804
Means			-0.105±0.033	0.166±0.269

Table A.2: Determination of elements i and Ω from zonal velocity. Each row in the table corresponds to a plot in figure A.4. The last row gives the mean values for Δi and $\Delta\Omega$, where each measurement has been appropriately weighted according to its uncertainty.

A.4 Previous Results and Discussion

Prior to 1975, every determination of the rotation elements i and Ω relied on essentially the same method used by Carrington. The approach used is to observe the motions of a large number of sunspots (over a long time period), and to use those motions to infer the direction of the axis of rotation. The approach relies on the assumption that, averaged over these long time periods (typically several years), sunspots do not exhibit significant asymmetric meridional motions. In the early part of this century, attempts to measure the rotation elements were made by Dyson &

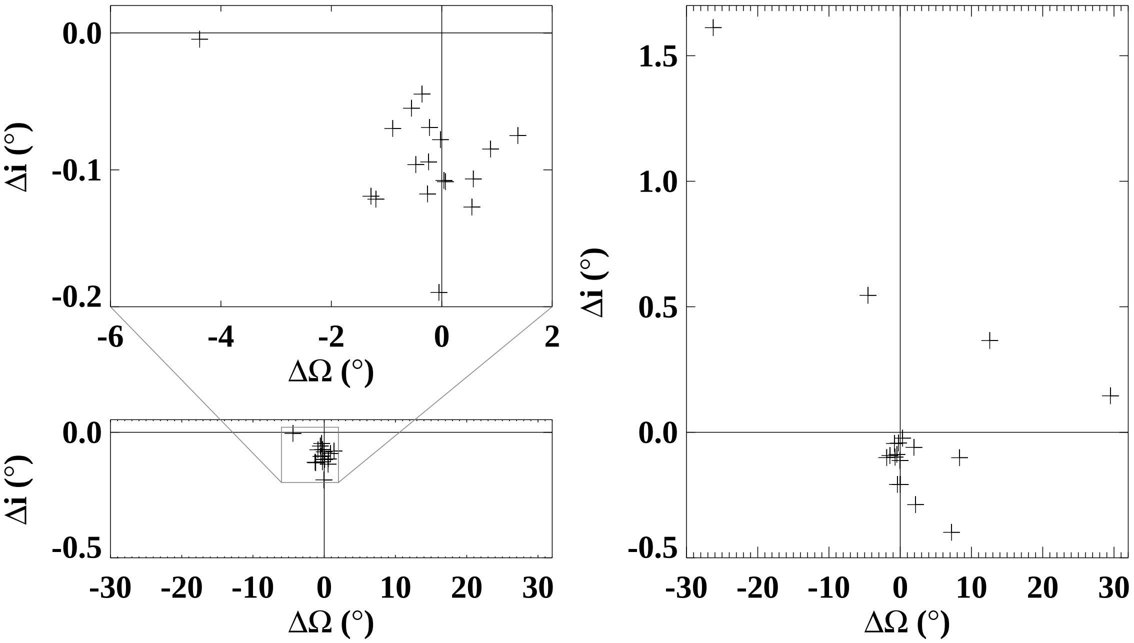

Figure A.5: The measurements from tables A.1 and A.2 have been plotted in the (i, Ω) phase space. The left-hand pair of figures is for the measurements made using the meridional flows; the right-hand figure is for the measurements of zonal flows. The lower plot on the left is on the same scale as the right-hand plot, to demonstrate the relative scatter of the two sets of measurements. The upper plot on the left shows a close-up of the meridional measurements.

Maunder (1912; 1913) and by Epstein (1916; 1917). None of these works (or Carrington's) offered any estimate of the uncertainty in their calculated values.

More recent efforts using sunspots have been made by Balthasar *et al.* (1986; 1987), by Stark & Wöhl (1981), and by Clark (1979). These four results agree with each other reasonably well (see figure A.6) and show that the inclination i is somewhat less than i_c, whereas the longitude defined by Ω is somewhat larger than Ω_c. As an interesting sidenote, the paper by Stark and Wöhl includes a recalculation of i_c and Ω_c from Carrington's original data, and estimates their uncertainties to be at least $\pm 0.11°$ and $\pm 0.52°$ respectively.

In the last few decades, some attempts have been made to determine the rotation

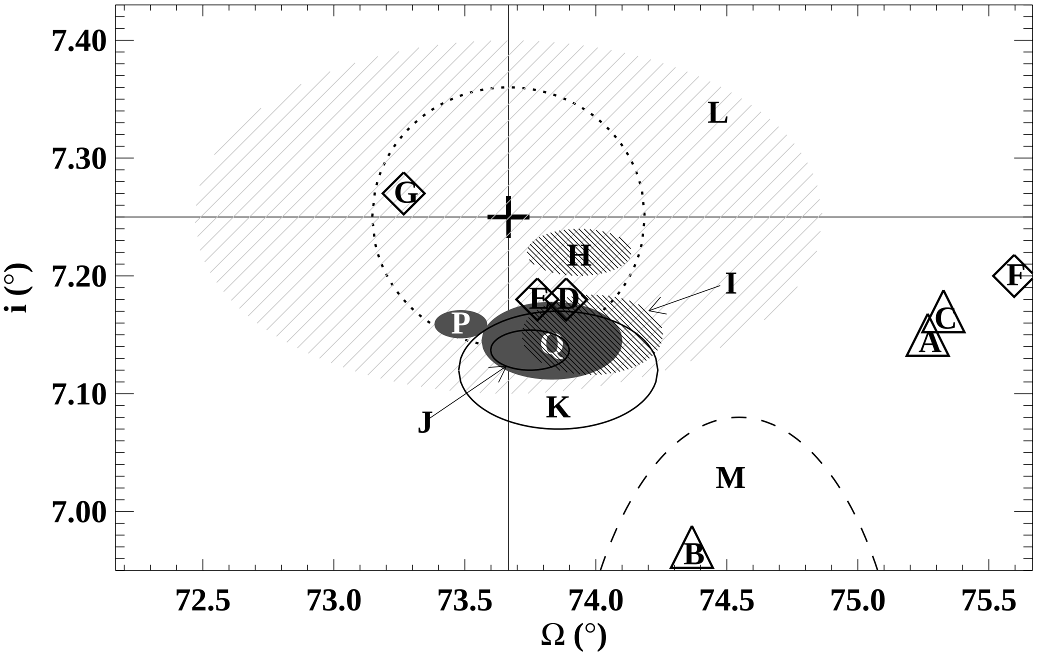

Figure A.6: A collection of past measurements of i and Ω. Note that Ω shown here is the value for year 1850.0. The "standard" values used (marked by the cross) are those given by Carrington (1863); the region marked by the dotted line represents an estimate of the uncertainty in Carrington's measurement, made by Stark and Wöhl (1981) using Carrington's original data. The triangles represent other measurements made during the nineteenth century, all from measurements of sunspots: (A) Laugier (1840); (B) Spoerer (1866); (C) Wilsing (1882). These three measurements are taken as cited by Wöhl (1978), who also includes a more complete selection of early measurements (these do not appear within the range of this plot). The four diamonds represent slightly more modern measurements, also from sunspots: (D) Dyson and Maunder (1912); (E) Dyson and Maunder (1913); (F) Epstein (1916); (G) Epstein (1917). The rest of the measurements, which are even more recent, include estimates of the uncertainty and are therfore depicted as ellipses of the appropriate size. Four of these are also from sunspot measurements: (H) Clark *et al.* (1979); (I) Stark and Wöhl (1981); (J) Balthasar *et al.* (1986); (K) Balthasar *et al.* (1987). The two largest ellipses are for measurements using direct Doppler velocities: (L) Labonte (1981) and (M) Wöhl (1978). The results from this work are the filled ellipses denoted by P (from the meridional circulation) and Q (from the rotation).

elements from direct Doppler measurements (Wöhl, 1978; LaBonte, 1981). Since it has long been observed that sunspots rotate at a slightly different *rate* than the bulk plasma (see the excellent review by Beck (2000) for examples), the question has been raised whether the rotation *axis* of the sunspots might also be different from that of the plasma. The result of Wöhl (1978) suggests that the rotation elements measured from Doppler velocites are significantly different from the magnetic measurements, although he attributes this to a probable error in the Carrington elements rather than the existence of two different axes of rotation. LaBonte (1981) found that the elements measured from Mt. Wilson data did not differ from the Carrington elements to within the uncertainty of his observations. It is worth noting that of all of the modern measurements shown in figure A.6 the two determinations from Doppler observations show the largest uncertainties. It is probably only possible to say that the "two-axis" question remains unanswered, although any difference between the hypothetical axes is certainly quite small.

The measurements presented in this work are not subject to many of the same systematic effects of earlier work. In particular, no assumptions are made about the north-south symmetry of either the rotation or the meridional flow. In fact, after removing the time-varying signals E_P and E_B the meridional flow still shows a significant southward bias over the duration of the observations. On the other hand, any *real* time-variation in the flow could be confused with the error signal. Since the observing period is only twice the period of the expected error signal, it is possible that the real time variation is not being separated very well from the spurious one. Also, there are probably some small systematic errors which arise from the time-distance treatment of the measurements. However, it should be noted that at only one point is a velocity converted to a travel-time difference or vice versa, and that is in the computation of v_ϕ to use in equations A.11 and A.12. As a final note, the measurements presented in this work depend on the assumption that the SOHO spacecraft pointing was constant during the entire observing run. Although this may not be strictly true, it is unfortunately the best information currently available. In the future, more accurate orientation information may be available from the spacecraft log files, at which time the estimates here might be revised.

Figure A.6 shows clearly that the set of modern measurements supports a value of i which is significantly less than i_c; a consensus seems to indicate a value of $i = 7.15°$. The measurements of Ω are of course subject to much greater uncertainty than the measurements of i, owing to the small value of the latter coordinate. The collection of modern measurements is consistent with the conclusion that $\Omega = \Omega_c$, at least to within twice the measurement uncertainty.

A.5 Conclusions

I have presented time-distance measurements of the meridional and zonal flows on the Sun which show time variations with periods which match the orbital period of the SOHO spacecraft. The time variation in the meridional velocity is consistent with an error in the Carrington elements of $\Delta i = -(0.091 \pm 0.012)°$, and $\Delta\Omega = -(0.18 \pm 0.10)°$. The time variation in the zonal velocity is more problematic, since it contains some spurious time variation which cannot be explained by this effect. However, a selected subset of measurements appear to also be consistent with the above error in the Carrington elements. The corrected values of the Carrington elements are in good general agreement with modern measurements, and indeed are within the (unstated) uncertainties in Carrington's original measurements (Stark and Wöhl, 1981).

These measurements using MDI data give an uncertainty in the Carrington elements which is smaller than any previous result. The evidence is very strong that the rotation axis of the Sun is inclined to the plane of the ecliptic by less than $i_c = 7.25°$; I suggest that a new value of $i = 7.15°$ be adopted, based on the collection of all the measurements which have been made to date.

In terms of the other results presented in this thesis, this conclusion obviously must be taken into consideration when examining time variation of solar flows. For the measurements presented in section 6.2.4, most of the apparent time variation in the equator-crossing flow can be accounted for by the error in the solar inclination.

Appendix B

Datasets Available from SOI

During the course of this work, large volumes of data have been generated and many computer cycles have been consumed. This appendix is included here to assist any future researchers in retrieving the data from the archives at Stanford's Solar Oscillations Investigation (SOI).

Datasets stored by SOI are available from the SOI Science Support Center (SSSC) at Stanford. To retrieve a dataset, it must be specified by `prog`, `level`, and `series`. For the datasets which I have archived, the `prog` is generally `giles` and the `level` is generally `lev2`; some exceptions will be noted later. I have used the `series name` to distinguish between different types of datasets, and the `series number` to identify the time (and sometimes position on the disk) of observation.

Table B.1 lists the broad categories of relevant datasets which are available and archived at the SSSC. The datasets are collections of FITS[1] files. The header of each file contains important information about the input data and processing. A few more details are provided below.

---

[1] The Flexible Image Transport System is a particular format of binary data storage.

Dataset Name				Dates
prog	level	series	series numbers	
mdi	lev2	track_08h	3717-3899	1996.05.25 - 1996.07.23
mdi	lev2	lxcor_08h	3717-3899 13717-13899 23717-23899	
mdi	lev2	rxcor_08h	3717-3864 13717-13899 23717-23899	
giles	lev2	track_fdV97	0-2403	1997.04.13 - 1997.05.11
giles	lev2	lxcor_fdV97		
giles	lev2	rxcor_fdV97		
giles	lev2	track_fdV98	0-2403	1998.01.09 - 1998.02.06
giles	lev2	lxcor_fdV98		
giles	lev2	rxcor_fdV98		
giles	lev2	trackvw_struct trackvw_struct_more trackvw_struct_more2	810-1332	1996.05.01 - 1998.06.24
giles	lev2	lxcorvw_all lxcorvw_all_more lxcorvw_all_more2	810-1332	
giles	lev2	rxcorvw_all rxcorvw_all_more rxcorvw_all_more2	810-1332	

Table B.1: A list of datasets archived at the Stanford SSSC. Datasets with series names which begin with `track` are tracked data cubes; series names beginning with `lxcor` denote cross correlations along the north-south direction; and those beginning with `rxcor` are cross correlations along the east-west direction. The datasets can be exported from the SSSC by via the World Wide Web at `http://soi.stanford.edu/`

B.1 Tracked Data Cubes

These datasets consist of the remapped, tracked, and background-subtracted cubes of images which were used to compute the cross correlations. Section 4.1 describes this process in more detail. Important FITS header parameters for each dataset include MAPSCALE, which determines the spacing of the remapped pixels; OBS_B0 and OBS_L0, which describe the Carrington coordinates of the center of the remapped region; T_FIRST and T_LAST, which desribe the temporal span of the data; and TRACK_A0 which measures the tracking velocity. Further details of the header parameters can be found in the man pages for module `track_region`, which was used to produce them. Module man pages can be accessed from the SOI Web site at `http://soi.stanford.edu/`.

In general, each dataset consists of a single data cube. The measurements from the 1996 Dynamics period are exceptional; each dataset consists of three different cubes from three different longitudes on the disk.

B.2 Cross Correlations

These datasets consist of cross correlations computed from the different tracked cubes. Cross correlations for the meridional flow measurements are denoted by series names which begin with `lxcor`; the rotation measurements have names beginning with `rxcor`.

Each dataset consists of a number of FITS files; each file contains the cross correlations for a particular starting latitude. Important header paramters include: DMIN, the minimum travel distance; DMAX, the maximum travel distance; and SINB, which is the starting latitude for the cross correlations (unique to each file). These datasets were produced with module `xcorr`; the man pages for describe the datasets and header parameters in more detail.

Within each file, each "row" contains $2N + 4$ elements. The first element is the mean travel distance (from the latitude given by the header parameter SINB, in the northward or westward direction) in degrees. The second element is the total number of pairs of image pixels which have been used to compute the cross correltaion. The third element is the average deviation (in degrees) from the target direction for propagation between the pairs of pixels. The remaining elements in the row are the cross correlation, from time lag $-N$ to time lag $+N$ (minutes).

The following special notes apply to the different entries in table B.1.

B.2.1 Dynamics 1996

The cross correlations are slightly different in form from the rest of the datasets listed in the table, because they were produced with an older version of `xcorr`. The series numbers for the tracked cubes denote the time; each cube covers a nominal eight-hour period. The series numbers for the cross correlations denote the same time period, with the prefix 0, 1, or 2 indicating the heliocentric longitude. Note that the east-west cross correlations with series numbers 3865-3899 have been lost from the archive.

B.2.2 Dynamics 1997, 1998

Not all series numbers between 0 and 2403 are used. The series number consists of two parts. The first two digits of each series number (00-24) denote the Carrington longitude of the center of the remapped region. The last two digits (00-19) denote different time periods of observation for that particular Carrington longitude. Each dataset covers a nominal eight-hour time period.

B.2.3 Structure

Series numbers denote different time periods. Each dataset covers a nominal time period of 180 hours and follows a particular Carrington longitude during that time. A new dataset, for a trailing Carrington longitude, begins every 36 hours. Where the 180-hour observing time is interrupted by a gap, and there are useable measurements on the other side of the gap, "filler" datasets have also been created. These are the `_more` and `_more2` series; they exist only for a small subset of series numbers.

Bibliography

Arevalo, M. J., Gomez, R., and Vazquez, M.: 1982, *Astron. Astrophys.* **111(2)**, 266

Babcock, H. W.: 1961, *Astrophys. J.* **133**, 572

Balthasar, H., Lustig, G., Stark, D., and Wöhl, H.: 1986, *Astron. Astrophys.* **160**, 277

Balthasar, H., Stark, D., and Wöhl, H.: 1987, *Astron. Astrophys.* **174**, 359

Basu, S., Antia, H. M., and Tripathy, S. C.: 1998, in (Korzennik and Wilson, 1998), pp 705–710

Beck, J. G.: 2000, *Sol. Phys.*, in press

Belvedere, G., Godoli, G., Motta, S., Paterno, L., and Zappala, R. A.: 1977, *Astrophys. J., Lett.* **214(2)**, 91

Birch, A.: 1999, private communication

Bogdan, T. J.: 1997, *Astrophys. J.* **477**, 475

Bracewell, R. N.: 1986, *The Fourier Transform and Its Applications*, McGraw-Hill, New York, second edition

Braun, D. C., Duvall, Jr., T. L., and LaBonte, B. J.: 1988, *Astrophys. J.* **335**, 1015

Braun, D. C. and Fan, Y.: 1998, *Astrophys. J., Lett.* **508**, L105

Brown, T. M.: 1980, in R. B. Dunn (ed.), *Solar Instrumentation: What's Next?*, p. 150, National Solar Observatory, Sunspot, NM

Brown, T. M., Christensen-Dalsgaard, J., Dziembowski, W. A., Goode, P., Gough, D. O., and Morrow, C. A.: 1989, *Astrophys. J.* **343**, 526

Brown, T. M. and Morrow, C. A.: 1987, *Astrophys. J., Lett.* **314**, L21

Carrington, R. C.: 1858, *Mon. Not. R. Astron. Soc.* **19**, 1

Carrington, R. C.: 1863, *Observations of the Spots on the Sun From November 9,* *1853 to March 24, 1861, Made at Redhill, London*, Williams & Norgate, London

Choudhuri, A. R., Schüssler, M., and Dikpati, M.: 1995, *Astron. Astrophys.* **303(2)**, L29

Christensen-Dalsgaard, J. et al.: 1996, *Science* **272**, 1286

Christensen-Dalsgaard, J. and Gough, D. O.: 1980, *Nature* **288**, 544

Christensen-Dalsgaard, J., Gough, D. O., and Thompson, M. J.: 1989, *Mon. Not. R. Astron. Soc.* **238(2)**, 481

Claerbout, J. F.: 1976, *Fundamentals of Geophysical Data Processing*, McGraw-Hill, New York

Clark, D. H., Yallop, B. D., Richard, S., Emerson, B., and Rudd, P. J.: 1979, *Nature* **280**, 299

Deubner, F.-L.: 1975, *Astron. Astrophys.* **44(2)**, 371

Deubner, F.-L. et al. (eds.): 1998, *New Eyes to See Inside the Sun and Stars*, Proceedings of IAU Symposium 185, Dordrecht, Kluwer

Dikpati, M. and Charbonneau, P.: 1999, *Astrophys. J.* **518**, 508

Domingo, V. and Fleck, B.: 1995, *Sol. Phys.* **162**, 1

D'Silva, S. and Duvall, Jr., T. L.: 1995, *Astrophys. J.* **438**, 454

Duvall, Jr., T. L.: 1979, *Sol. Phys.* **63**, 3

Duvall, Jr., T. L., Dziembowski, W. A., Goode, P. R., Gough, D. O., Harvey, J. W., and Leibacher, J. W.: 1984, *Nature* **310**, 22

Duvall, Jr., T. L., Jeffries, S. M., Harvey, J. W., and Pomerantz, M. A.: 1993, *Nature* **362**, 430

Dyson, F. W. and Maunder, E. W.: 1912, *Mon. Not. R. Astron. Soc.* **72(7)**, 564

Dyson, F. W. and Maunder, E. W.: 1913, *Mon. Not. R. Astron. Soc.* **73(7)**, 673

Eddy, J. A., Gilman, P. A., and Trotter, D. E.: 1976, *Sol. Phys.* **46**, 3

Epstein, T.: 1916, *Astron. Nachr.* **202**, 401

Epstein, T.: 1917, *Astron. Nachr.* **204**, 351

Evans, J. W.: 1980, in R. B. Dunn (ed.), *Solar Instrumentation: What's Next?*, p. 155, National Solar Observatory, Sunspot, NM

Evans, S.: 1999, *Ph.D. thesis*, UCLA

Giles, P. M. and Duvall, Jr., T. L.: 1998, in (Deubner et al., 1998), p. 149

Giles, P. M., Duvall, Jr., T. L., and Scherrer, P. H.: 1998, in (Korzennik and Wilson, 1998), pp 775–780

Giles, P. M., Duvall, Jr., T. L., Scherrer, P. H., and Bogart, R. S.: 1997, *Nature* **390**, 52

Gilman, P. A.: 1972, *Sol. Phys.* **27**, 3

Gilman, P. A. and Miller, J.: 1986, *Astrophys. J.* **61**, 585

Godoli, G. and Mazzucconi, F.: 1979, *Sol. Phys.* **64(2)**, 247

González Hernández, I., Patrón, J., Bogart, R. S., et al.: 1998, in (Korzennik and Wilson, 1998), pp 781–786

Gough, D.: 1984, *Philosophical Transactions of the Royal Society London A* **313(1524)**, 27

Gough, D. O.: 1976, in R. M. Bonnet and P. Delache (eds.), *The Energy Balance and Hydrodynamics of the Solar Chromosphere and Corona*, pp 3–36, Clermont-Ferrand, G. de Bussac

Gough, D. O.: 1993, in J.-P. Zahn and J. Zinn-Justin (eds.), *Astrophysical Fluid Dynamics*, Vol. XLVII of *Les Houches*, Chapt. 7, pp 339–615, Elsevier Science Publishers, Amsterdam

Gradshteyn, I. S. and Ryzhik, I. M.: 1994, *Table of Integrals, Series, and Products*, Academic Press, San Diego, fifth edition

Hale, G. E.: 1908, *Astrophys. J.* **28**, 315

Hathaway, D. H.: 1996, *Astrophys. J.* **460**, 1027

Hathaway, D. H., Gilman, P. A., Harvey, J. W., et al.: 1996, *Science* **272**, 1306

Howard, R., Adkins, J. M., Boyden, J. E., Cragg, T. A., Gregory, T. S., Labonte, B. J., Padilla, S. P., and Webster, L.: 1983, *Sol. Phys.* **83(2)**, 321

Howard, R. and Gilman, P. A.: 1986, *Astrophys. J.* **307**, 389

Howard, R. and Harvey, J. W.: 1970, *Sol. Phys.* **12**, 23

Howard, R. and LaBonte, B. J.: 1980, *Astrophys. J., Lett.* **239**, L33

Howard, R. F.: 1984, *Ann. Rev. Astron. Astrophys.* **22**, 131

Howe, R., Komm, R., and Hill, F.: 2000, *Sol. Phys.*, submitted

Jackson, J. D.: 1975, *Classical Electrodynamics*, John Wiley & Sons, new York, second edition

Jensen, J., Jacobsen, B. H., and Cristensen-Dalsgaard, J.: 1998, in (Korzennik and Wilson, 1998), pp 635–640

Kambry, M. A., Nishikawa, J., Sakurai, T., Ichimoto, K., and Hiei, E.: 1991, *Sol. Phys.* **132**, 41

Keys, R. G.: 1981, *Acoustics, Speech, and Signal Processing*, Vol. 29 of *IEEE Transactions*, pp 1153–1160

Komm, R., Howard, R., and Harvey, J.: 1993a, *Sol. Phys.* **145(1)**, 1

Komm, R. W., Howard, R. F., and Harvey, J. W.: 1993b, *Sol. Phys.* **147**, 207

Korzennik, S. G. and Wilson, A. (eds.): 1998, *Structure and Dynamics of the Sun and Sun-Like Stars*, Proceedings of SOHO6/GONG98 Workshop, Noordwijk, ESA Publications Division

Kosovichev, A. and Zharkova, V.: 1998, in (Deubner et al., 1998), pp 191–914

Kosovichev, A. G.: 1996, *Astrophys. J., Lett.* **461**, L55

Kosovichev, A. G. and Duvall, Jr., T. L.: 1997, in F. Pijpers, J. Christensen-Dalsgaard, and C. S. Rosenthal (eds.), *Solar Convection and Oscillations and Their Relationship*, Proceedings of SCORe96 Workshop, pp 241–260, Kluwer, Dordrecht

Kosovichev, A. G. and Schou, J.: 1997, *Astrophys. J., Lett.* **482**, L207

LaBonte, B. J.: 1981, *Sol. Phys.* **69**, 177

LaBonte, B. J. and Howard, R. F.: 1982, *Sol. Phys.* **80**, 361

Larsen, R.: 1999, private communication

Latushko, S.: 1994, *Sol. Phys.* **149**, 231

Leibacher, J. and Stein, R. F.: 1971, *Astrophys. J., Lett.* **7(3)**, 191

Leighton, R.: 1964, *Astrophys. J.* **140**, 131

Leighton, R.: 1969, *Astrophys. J.* **156(1)**, 1

Leighton, R. B.: 1960, Proceedings of IAU Symposium 12, pp 321–325

Leighton, R. B., Noyes, R. W., and Simon, G. W.: 1962, *Astrophys. J.* **135**, 474

Meunier, N.: 1999, *Astrophys. J.*, in press

Parker, E.: 1975, *Astrophys. J.* **198(1)**, 205

Patrón, J., Hill, F., Rhodes, Jr., E. J., Korzennik, S. G., and Cacciani, A.: 1995, *Astrophys. J.* **455**, 746

Press, W. H., Tuekolsky, S. A., Vetterling, W. T., and Flannery, B. P.: 1992, *Numerical Recipes in C*, Cambridge University Press, Cambridge, second edition

Ribes, E., Mein, P., and Mangeney, A.: 1985, *Nature* **318**, 170

Ryutova, M. and Scherrer, P.: 1998, *Astrophys. J.* **494(1)**, 438

Scherrer, P. H., Bogart, R. S., Bush, R. J., et al.: 1995, *Sol. Phys.* **162**, 129

Schou, J., Antia, H. M., Basu, S., et al.: 1998, *Astrophys. J.* **505**, 390

Schou, J. and Bogart, R. S.: 1998, *Astrophys. J., Lett.* **540**, L131

Schroter, E. and Vazquez, M.: 1978, *Sol. Phys.* **60(1)**, 181

Schwabe, S. H.: 1843, *Astron. Nachr.* **20**, 243

Smart, W. M.: 1977, *Textbook on Sperical Astronomy*, Cambridge University Press, Cambridge, second edition, Revised by R. M. Green

Snodgrass, H. and Howard, R.: 1985a, *Sol. Phys.* **95(2)**, 221

Snodgrass, H. and Howard, R.: 1985b, *Science* **228(4702)**, 945

Snodgrass, H. B.: 1983, *Astrophys. J.* **270**, 288

Snodgrass, H. B.: 1984, *Sol. Phys.* **94**, 13

Snodgrass, H. B. and Ulrich, R. K.: 1990, *Astrophys. J.* **351**, 309

Spiegel, E. A. and Zahn, J.-P.: 1992, *Astron. Astrophys.* **265**, 106

Stark, D. and Wöhl, H.: 1981, *Astron. Astrophys.* **93**, 241

Title, A. M. and Rosenberg, W. J.: 1981, *Opt. Eng.* **20(6)**, 815

Toomre, J., Christensen-Dalsgaard, J., Howe, R., Larsen, R., Schou, J., and Thompson, M. J.: 2000, *Sol. Phys.*, submitted

Ulrich, R. K.: 1970, *Astrophys. J.* **162(3)**, 993

Ulrich, R. K., Boyden, J. E., Webster, L., Snodgrass, H. B., Padilla, S. P., Gilman, P., and Scheiber, T.: 1988, *Sol. Phys.* **117**, 291

van Ballegooijen, A.: 1982, *Astron. Astrophys.* **113(1)**, 99

van Ballegooijen, A. A. and Choudhuri, A. R.: 1988, *Astrophys. J.* **333**, 965

Wang, Y.-M., Sheeley, Jr, N. R., and Nash, A. G.: 1991, *Astrophys. J.* **383**, 431

Wilcox, J. M. and Howard, R.: 1970, *Sol. Phys.* **13(2)**, 251

Wilcox, J. M., Schatten, K. H., Tanenbaum, A. S., and Howard, R.: 1970, *Sol. Phys.* **14(2)**, 255

Wöhl, H.: 1978, *Astron. Astrophys.* **62**, 165

Ye, B. and Livingston, W.: 1998, *Sol. Phys.* **179(1)**, 1

Zappala, R. and Zuccarello, F.: 1991, *Astron. Astrophys.* **242(2)**, 480

Zweibel, E. G. and Gough, D. O.: 1995, in J. T. Hoeksema, V. Domingo, B. Fleck, and B. Battrick (eds.), *Helioseismology*, Vol. 2 of *Proceedings of SOHO4 Workshop*, pp 73–76, ESA Publications Division, Noordwijk